COMPARISON, OPTIMIZATION, AND APPLICATION OF VARIOUS
SPONTANEOUS PARAMETRIC DOWNCONVERSION SOURCES OF
POLARIZATION-ENTANGLED PHOTON PAIRS

BY

KRISTINA A. MEIER

DISSERTATION

Submitted in partial fulfillment of the requirements
for the degree of Doctor of Philosophy in Physics
in the Graduate College of the
University of Illinois Urbana-Champaign, 2021

Urbana, Illinois

Doctoral Committee:

    Associate Professor Virginia Lorenz, Chair
    Professor Paul G. Kwiat, Director of Research
    Assistant Professor Elizabeth Goldschmidt
    Professor Vidya Madhavan

Abstract

As benchtop quantum information protocols become increasingly more advanced and the distances over which these experiments are performed become significantly longer, integrated optics provide a small, robust, and practical alternative to traditional bulk optics. Waveguide technology makes it possible to create bright entangled-photon sources that can be used on platforms where weight and stability requirements are limiting factors, e.g., on aerial or even space-based mobile platforms, which could allow reconfigurable long-distance transfer of photonic qubits. Specifically, for our goals, we are working on the characterization and optimization of both highly nondegenerate and degenerate Spontaneous Parametric Down-Conversion waveguide sources of collinear polarization-entangled photon pairs using various entanglement methods determined by the relevant application. Our ultimate goal is to create polarization-entangled photon pairs that are also spectrally unentangled, a necessary condition for efficient multiphoton protocols, e.g., for quantum repeaters. Additionally, highly nondegenerate polarization-entangled photon pairs can be manipulated to create frequency-entangled pairs for ultra-high-timing-resolution interference-based quantum metrology on the attosecond-level. This metrology scheme would enable new technologies for both biomedical and defense applications.

For Eric, Arthur, and Baron

In memory of Ace

Acknowledgments

This work represents the Kwiat group's first foray into integrated photonic sources. Through a long-standing collaboration with AdvR, Inc. in Bozeman, MT we developed a source that was the first of its kind. Phil Battle and Tony Roberts were indispensable members of this collaboration and extended to us the patience and grace needed for us to complete our work. They welcomed me in Bozeman during my first summer of graduate school so that I could better understand their part of the work. Thank you Phil, Tony, and the rest of the team for your support over the years.

Thank you to my advisor, Paul Kwiat, for pushing me past my limits. You would apologize for being tough on me, but did not see the immense appreciation I had for every one of our one-on-one meetings. From preparing me for my first journal club presentation to perfecting my defense, you have always pushed me just far enough and I am forever grateful.

Thank you to all my mentors prior to graduate school. Thank you to my professors from Denison University who were truly inspirational and unbelievably good at teaching. You treated us as individuals with needs and aspirations of our own. Thank you to Josh Bienfang and Michael Wayne who introduced me to the field while providing endless entertainment in the lab.

Thank you to my mom who has worked so hard over the years to get me exactly where I needed to be at every point in my life. Many tears were shed at every step, but somehow it always worked out. Thank you, Mom, for showing me what hard work brings and for always supporting me.

Thank you to my dad who brought me to his workshop and introduced me to electronics and soldering when I was very young. Thank you for always pushing me to follow science and technology and for being an endless source of dad jokes - *What's zero plus zero? Eight!*

Thank you to the rest of my family - my siblings, my step-parents, my in-laws, my aunts and uncles, and my grandparents. My list of cheerleaders is never-ending (I'm pretty sure one of my sisters thinks I shoot atoms through walls, but that is just more proof of her unconditional support!). A special thank you to my grandma, Mary Kay, who is one of the strongest women I know. She has been my cheerleader from the start and is still rocking her independence at 83 years old!

Thank you to Rebecca Sandoval, Courtney Krafczyk, Kathleen Winters-Castle, and Michelle Victora who kept me afloat through every obstacle over the past six years. From forcing me into the office to get a desk my first year (thanks Michelle!) to helping me survive parenthood as a working parent (thanks Courtney and Kathleen!) to getting a job (thanks Rebecca!), these four women have been irreplaceable.

Thank you to my 2510 crew. I am struggling to find the words to show my gratitude. You have been there for me literally every single day of the past four years. Colin, Michael, Spencer - there are no words. They say it takes a village to raise a child and you were that village. You all stepped up in every way possible and I am forever grateful. Thank you.

Finally, thank you to my husband, my son, and my dogs. These past six years have not been easy; we said goodbye to Ace, went through months of heartache with Baron, and survived eight excruciating days in the NICU with Arthur. We also had a lot of laughs along the way; we navigated Japan, Italy, and France together and went on tons of hikes and camping trips all around Illinois. We have experienced every emotion you can imagine over the past six years, but in this moment we are a mere two weeks away from starting our dream jobs in our version of paradise. *Can you believe it? We did it!*

Table of Contents

List of Figures

List of Abbreviations

AFM   Atomic Force Microscopy

BS   Beamsplitter

DM   Dichroic Mirror

DoF   Degree of Freedom

DPSS   Diode-Pumped Solid State

HOM   Hong-Ou-Mandel

HWP   Half Waveplate

KTP   Potassium Titanyl Phosphate

NA   Numerical Aperature

OAM   Orbital Angular Momentum

PBS   Polarizing Beamsplitter

ppKTP   Periodically Poled KTP

PPLN   Periodically Poled Lithium Niobate

QPM   Quasi-Phase-Matching

QWP   Quarter Waveplate

SFG   Sum-Frequency Generation

SHG   Second Harmonic Generation

Si-APD   Silicon Avalanche Photodetector

SNSPD   Superconducting Nanowire Single Photon Detector

SPDC   Spontaneous Parametric Downconversion

SWaP   Size, Weight, and Power

TEC   Thermoelectric Cooler

WP   Waveplate

List of Symbols

c Speed of Light, $c = 299792458$ m/s

π pi, $\pi = 3.1415926$

i Imaginary Number, $i = \sqrt{-1}$

ϵ_0 Vacuum Permittivity, $\epsilon_0 = 8.85 * 10^{-12}$ F/m

$\hbar$ Reduced Planck's Constant, $\hbar = 1.055 * 10^{-34}$ J·s

t Time

e Euler's Number, $e = 2.71828$

$A,\ \alpha,\ \beta$ Amplitudes

ω Angular Frequency

λ Wavelength

$\Delta\lambda$ Bandwidth

λ_0 Vacuum Wavelength

ψ Quantum State

$p,\ s,\ i$ Pump, Signal, and Idler

$P(t)$ Time-Varying Polarization

$E(t)$ Electric Field

$\chi^{(2)}$ Nonlinear Susceptibility

$\hat{a},\ \hat{a}^\dagger$ Annihilation and Creation Operators

$\vec{r}$ Path Vector

$\hat{H}$ Hilbert Space

d Dimension of the Hilbert Space

δ	Dirac Delta Function
Λ	Poling Period
k	Wave Vector
n	Index of Refraction
f	Linear Frequency
Δk	Wave Vector Mismatch
L	Crystal Length
l	Path Length
v_g	Group Velocity
H	Horizontal Polarization
V	Vertical Polarization, Visibility, or Volume
D	Diagonal Polarization
A	Anti-Diagonal Polarization
R	Right-Circular Polarization
L	Left-Circular Polarization
ρ	Density Matrix
σ	Density Matrix, or Half-Bandwidth
C	Concurrence
F	Fidelity
γ	State Purity
S_L	Linear Entropy
τ	HOM Time Delay
$\Delta\omega$	Frequency Detuning
ϕ, θ	Phase
$\Delta\tau$	Coherence Time

Chapter 1

Introduction

Quantum networking presents the next challenge in the field of quantum information. Extending beyond previously implemented quantum information protocols and making a long-range, practical, and commercially viable quantum network for reliable and secure information transfer is a natural next step in taking quantum information science from benchtop experiments to real-world applications. Towards this goal, an important area where further development is essential is scalable integrated sources of entanglement. Since both the atmosphere and fiber optics have significant channel loss, technological developments that allow for the transmission of photonic qubits over long distances is critical. One currently accepted method for doing so is to create a network of quantum nodes where qubits can be sent, stored, and made to interact with each other, enabling feats such as teleportation [1] and entanglement swapping [2–4]. In this scenario, optimized quantum sources are critical. Furthermore, if photonic qubits are sent through free-space channels, then the nodes may need to be located on platforms that are well above the Earth's surface, in order to maximize optical access and minimize the deleterious effects of atmospheric turbulence. To do so, we can imagine leveraging previous technological advances in satellite networking to create space-based networks of quantum nodes so that quantum information can be transmitted over long distances [5] and to many different locations. Mobile platforms are also attractive for defense applications; for example, the capability to send quantum-secured information from ship to ship via drones could be advantageous for the Navy. However, both space-based satellite and drone-based platforms have stringent size and weight requirements. Moving from bulk table-top implementations to integrated photonic circuits would allow for increased flexibility, robustness, and efficiency for quantum communication protocols on mobile platforms, assuming such devices could be made to operate at a level comparable to their bulk-optic counterparts.

Size, weight, and power (SWaP) are not the only important metrics. For quantum networks using techniques such as quantum teleportation [1], entanglement swapping [2–4], or others that involve two-photon interference., photon pair sources must feature high entanglement quality while also emitting spectrally pure photon pairs, in which the photons in a given pair are not entangled in frequency*. Thus far, bulk systems outperform integrated photonics in their ability to create usable entangled photons, especially when the photon wavelengths become increasingly nondegenerate [6]; this could be important, e.g., when sending one photon down an optical fiber (where a wavelength in the low-loss telecommunication band is preferred), and using the other to connect to a quantum memory, many of which have their storage wavelength between 600 and 1200 nm. To determine the current optimal source for mobile-platform networks, a direct comparison between three entanglement sources - waveguide-based, beam-displacer-based, and Sagnac-interferometer-based - is desired. The three sources will be rated based on their ability to create a maximally entangled two-qubit polarization state, overall brightness, and a few other relevant metrics, the former two sources being discussed in this dissertation. As an additional experiment, the "best" source in terms of brightness and entanglement fidelity will be used in an interferometer-based attosecond-resolution quantum-metrology project, coined "Project Atto," that requires such highly nondegenerate polarization-entangled photon pairs to achieve the desired timing resolution ($\sim$ as).

1.1   An Introduction to Polarization Entanglement

The field of quantum information strongly relies on the phenomenon of quantum entanglement. This entanglement can exist between particles whether they are atoms or photons and can describe the relationship between their physical properties such as frequency, polarization, spin, momentum, and relative location of these particles. If two particles are entangled, it means that one or more of these physical properties is perfectly correlated - for

---

*Spectral purity of the photon source does not mean the photons are monochromatic; instead, it refers to the factorizability of the spectral part of the overall quantum state. As we discuss in greater details in Section 4.1, spectral correlations between the photons will diminish/eliminate their ability to achieve high quality two-photon interference, which underlies quantum teleportation and entanglement swapping.

instance, they have indefinite but identical polarizations - and the underlying quantum state is non-separable - you cannot describe one particle without the other. Mathematically, this correlation shows up as the inability to factor the mathematical description of one particle from the other, i.e., the total quantum state cannot be written as a product state. Generally, one can describe an entangled two-particle two-qubit[†] state as

$$|\psi\rangle = \alpha|a_1\rangle \otimes |b_2\rangle + \beta|b_1\rangle \otimes |a_2\rangle = \alpha|a_1 b_2\rangle + \beta|b_1 a_2\rangle, \tag{1.1}$$

where 1 and 2 label the particle, a and b describe the entangled properties of those particles, and α and β are the non-zero amplitudes of the two-photon state such that $|\alpha|^2 + |\beta|^2 = 1$; for a pure quantum state such as Equation 1.1, the entanglement will be maximal when $|\alpha| = |\beta|$. In this state, if the 1st particle is measured to have a particular value of observable a, e.g., $a =$ horizontal polarization, then the 2nd particle must have a corresponding value for observable b, e.g., $b =$ vertical polarization. The shorthand used in the right-hand equality in Equation 1.1 is common in the field of quantum information and will be used throughout this dissertation.

1.1.1 Two-Photon Polarization Entanglement

Let us now use polarization and frequency as our descriptors: the particles will be polarized photons, which we will call our quantum bits or "qubits," with nominal frequencies ω_1 and ω_2[‡]. The states we are creating can come in three broad levels of entanglement: maximally entangled, partially entangled, or separable (not entangled). There are four canonical two-qubit maximally entangled states, called Bell States, that are crucial to current quantum

---

[†]A "qubit," or quantum bit, is the essential unit of quantum information, just as the bit (binary digit) is for classical information. The qubit is a general superposition of a 2-state system: $|\psi\rangle = \alpha|0\rangle + \beta|1\rangle$, where $|\alpha|^2 + |\beta|^2$, and $|0\rangle$ and $|1\rangle$ are two orthogonal basis states. For example, $|0\rangle + |1\rangle$ could be ground and excited states of an atom, spin up and down states of a spin, etc. For optical qubits, polarization qubits are most common; one can also have superpositions of time bins or different spatial modes (and in these cases can encode larger-dimensional states (qutrits, qudits). Here we restrict our discussions to qubits encoded in polarization.

[‡]It is helpful to note that although in our field it is more common to refer to a photon's "wavelength" (represented by λ), "frequency" or ω is typically used when discussing the theory. The relationship between these two values is: $\omega = 2\pi c/\lambda$, where here we implicitly assume this is the wavelength in vacuum; later we will need to account for wavelength (and polarization) dependence of the refractive index of the material through which the photons are propagating.

information protocols, such as quantum teleportation [1] and entanglement-based quantum key distribution [7]:

$$|\phi^+\rangle \equiv \frac{1}{\sqrt{2}}\left(|H_{\omega_1}H_{\omega_2}\rangle + |V_{\omega_1}V_{\omega_2}\rangle\right) \tag{1.2}$$

$$|\phi^-\rangle \equiv \frac{1}{\sqrt{2}}\left(|H_{\omega_1}H_{\omega_2}\rangle - |V_{\omega_1}V_{\omega_2}\rangle\right) \tag{1.3}$$

$$|\psi^+\rangle \equiv \frac{1}{\sqrt{2}}\left(|H_{\omega_1}V_{\omega_2}\rangle + |V_{\omega_1}H_{\omega_2}\rangle\right) \tag{1.4}$$

$$|\psi^-\rangle \equiv \frac{1}{\sqrt{2}}\left(|H_{\omega_1}V_{\omega_2}\rangle - |V_{\omega_1}H_{\omega_2}\rangle\right), \tag{1.5}$$

where $H(V)$ refers to horizontally(vertically) polarized light[§]. For the purpose of this work, $|\psi^+\rangle$ will be discussed predominantly, but all the states are equivalent, in that they can be interconverted using only local operations, e.g., implemented with waveplates. Maximally entangled states are the usual desired resource for quantum information protocols; however, partially entangled states, such as $|\psi\rangle = \alpha|H_{\omega_1}V_{\omega_2}\rangle + \beta|V_{\omega_1}H_{\omega_2}\rangle$, can be sometimes used, albeit with lower fidelities. Finally, it is helpful to have an example of an unentangled, or separable, two-qubit state, e.g., $|\psi_{sep}\rangle = \frac{1}{\sqrt{2}}\left(|H_{\omega_1}H_{\omega_2}\rangle + |V_{\omega_1}H_{\omega_2}\rangle\right)$. Mathematically, this state can be written as a product of $|H_{\omega_1}\rangle + |V_{\omega_1}\rangle$ and $|H_{\omega_2}\rangle$: $\frac{1}{\sqrt{2}}\left(\left(|H_{\omega_1}\rangle + |V_{\omega_1}\rangle\right) \otimes |H_{\omega_2}\rangle\right)$ and therefore does not describe an entangled state. For the moment we are discussing only the polarization degree of freedom (DoF). Of course, the photons could still be entangled in some other DoF, e.g., their energy or temporal DoF, and we will see later that this will strongly affect their usability, e.g., for quantum network applications.

It is common to use a photon's polarization as a qubit state in quantum information protocols as it is easy and not very resource intensive to manipulate polarization. Practically, waveplates (WP) and polarizers can be purchased as relatively inexpensive off-the-shelf components, allowing for transformation or measurement of a photon's polarization. It is also

---

[§]Experimentally, the definition of horizontally and vertically polarized light is relative with respect to some reference, e.g., the optical table and the other optics on the table. However, it is important to note that H and V are orthogonal and form a complete basis in the polarization Hilbert space. Their six polarization combinations ($|H\rangle$, $|V\rangle$, $|D\rangle \equiv \frac{1}{\sqrt{2}}(|H\rangle + |V\rangle)$, $|A\rangle \equiv \frac{1}{\sqrt{2}}(|H\rangle - |V\rangle)$, $|L\rangle \equiv \frac{1}{\sqrt{2}}(|H\rangle + i|V\rangle)$, and $|R\rangle \equiv \frac{1}{\sqrt{2}}(|H\rangle - i|V\rangle)$) are sufficient to fully describe the polarization state of the light. We will use H and V as our basic polarization states throughout this dissertation.
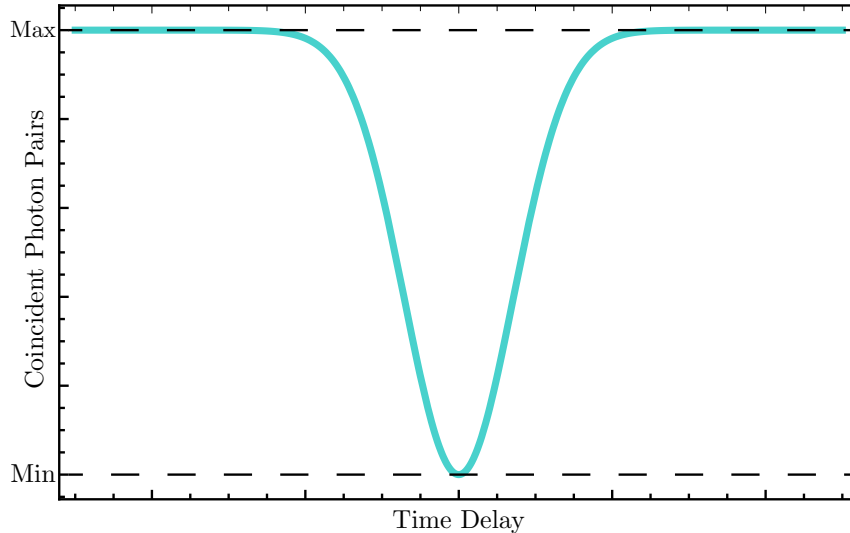
Figure 1.1: When two indistinguishable photons interfere on a 50:50 beamsplitter (BS), the measured coincidences go to zero when the photons arrive simultaneously (i.e., with zero relative delay), resulting in the characteristic HOM dip.

straightforward to separate photons both spatially and temporally based on their polarization using standard optics, e.g, using polarizing beamsplitters (PBS). In this way, using the polarization of a photon as a qubit is an optimal choice for various experiments. This being said, it is important to keep in mind that there are other aspects of light that can be used to encode quantum states, e.g., time-bin [8], spatial paths [9], orbital angular momentum (OAM) [10], and frequency [11].

1.1.2 Hong-Ou-Mandel Dip

To entangle two photons using the protocol of entanglement swapping, information about where the photons were created is erased: the photons must be indistinguishable from each other. In 1987, Hong, Ou, and Mandel (HOM) developed an experiment where two photons interfere on a 50:50 beamsplitter (BS), through which each photon has equal probability of reflecting or transmitting [12]; single-photon detectors in both outputs of the BS detect the three possible outcomes: both photons go to the same detector (two options), or one photon goes to each. The results are post-selected based on coincidence, only counting cases where the photons were detected on different detectors. The coincidences are then plotted with respect to the relative arrival time between the two photons. For indistinguishable photons,
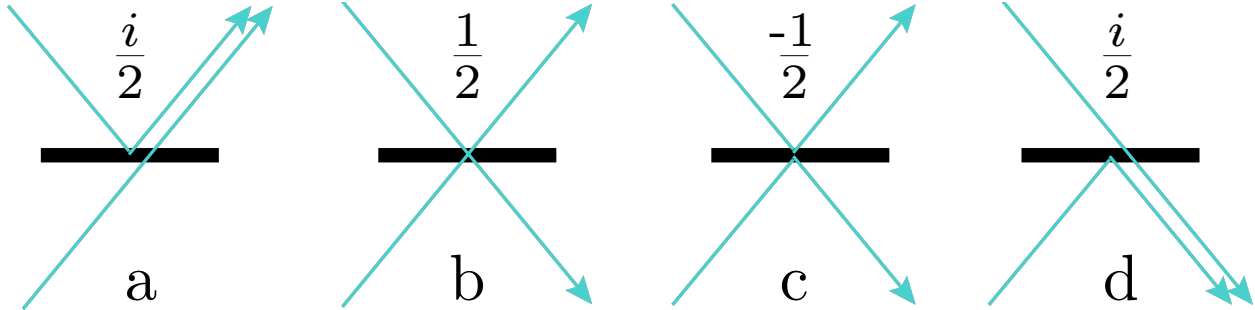
Figure 1.2: The four possible processes for two photons interfering on a 50:50 BS. (a) The top photon reflects and picks up an amplitude of i and the bottom photon reflects and picks up an amplitude of 1, for a total amplitude of $1/\sqrt{2} \times i/\sqrt{2} = i/2$. (b) Both photons transmit for a total amplitude of $1/\sqrt{2} \times 1/\sqrt{2} = 1/2$. (c) Both photons reflect for a total amplitude of $i/\sqrt{2} \times i/\sqrt{2} = -1/2$. (d) The top photon transmits and the bottom photon reflects for a total amplitude of $i/\sqrt{2} \times 1/\sqrt{2} = i/2$. For indistinguishable processes, finding the total probability requires adding the amplitudes and then taking the amplitude squared. For distinguishable processes, each process can be treated independently.

the resulting plot, shown in Figure 1.1, features a characteristic dip at a relative time delay of zero, corresponding to the two photons arriving simultaneously at the BS.

The dip in coincidences occurs due to the destructive interference of two indistinguishable processes. When the two photons reach the BS, they can either transmit or reflect, which gives us a total of four possible processes between the two photons: one reflects and one transmits (Fig. 1.2(a) and Fig. 1.2(d)), both reflect (Fig. 1.2(c)), or both transmit (Fig. 1.2(c)). The probability amplitudes are listed above each possibility in Figure 1.2. Each reflection off the BS picks up an amplitude of $\frac{i}{\sqrt{2}}$, whereas each transmission picks up $\frac{1}{\sqrt{2}}$. Squaring the absolute value of the amplitude of each process gives the probability of it occurring: $|(\frac{i}{\sqrt{2}})(\frac{1}{\sqrt{2}})|^2 = |(\frac{1}{\sqrt{2}})(\frac{1}{\sqrt{2}})|^2 = |(\frac{i}{\sqrt{2}})(\frac{i}{\sqrt{2}})|^2 = (\frac{1}{\sqrt{2}})(\frac{i}{\sqrt{2}})|^2 = \frac{1}{4}$. So, if we treat each process independently, they each have an equal probability. However, if we assume indistinguishable processes, then there is no way to distinguish the processes in Figure 1.2(b) from Figure 1.2(c) and we must add the <u>amplitudes</u> of these indistinguishable processes before taking the absolute square. Now, the probability of process (b) or (c) happening is, $P = |(\frac{1}{\sqrt{2}})^2 + (\frac{i}{\sqrt{2}})^2|^2 = 0$, which is why zero coincidences are measured for indistinguishable processes with no time delay.

In order to quantify how indistinguishable the photons are, we can use the "visibility," $V \equiv (\text{Max}-\text{Min})/(\text{Max}+\text{Min})$, where "Max" and "Min" refer to the maximum and minimum detected coincidences, respectively, as specified in Figure 1.1. Given this definition, if the two

(a) $\qquad |\psi\rangle = |H_{\omega_1} V_{\omega_2}\rangle + |V_{\omega_1} H_{\omega_2}\rangle \rightarrow |\psi_{DA}\rangle = |D_{\omega_1} D_{\omega_2}\rangle + |A_{\omega_1} A_{\omega_2}\rangle$

(b) $\qquad |H\rangle = \frac{1}{\sqrt{2}}(|D\rangle + |A\rangle) \qquad |V\rangle = \frac{1}{\sqrt{2}}(|D\rangle - |A\rangle)$

(c) $|\psi\rangle = \frac{1}{2}(|D_{\omega_1}\rangle + |A_{\omega_1}\rangle)(|D_{\omega_2}\rangle - |A_{\omega_2}\rangle) + \frac{1}{2}(|D_{\omega_1}\rangle - |A_{\omega_1}\rangle)(|D_{\omega_2}\rangle + |A_{\omega_2}\rangle)$

(d) $|\psi\rangle = \frac{1}{2}(|D_{\omega_1} D_{\omega_2}\rangle - |D_{\omega_1} A_{\omega_2}\rangle + |A_{\omega_1} D_{\omega_2}\rangle - |A_{\omega_1} A_{\omega_2}\rangle)$

(e) $\qquad\qquad + \frac{1}{2}(|D_{\omega_1} D_{\omega_2}\rangle + |D_{\omega_1} A_{\omega_2}\rangle - |A_{\omega_1} D_{\omega_2}\rangle - |A_{\omega_1} A_{\omega_2}\rangle)$

Figure 1.3: (a) For a two-qubit state to be entangled, it must display correlations in all polarization bases. Therefore, to verify entanglement, the state can be transformed to the $\{D, A\}$ basis. (b) H and V can be written in the $\{D, A\}$ basis. (c) Transforming the state to the $\{D, A\}$ basis. (d) The simplified first term. (e) The simplified second term, describing photons created in the second process. In order to have an entangled state, the red-shaded ket from (d) must cancel with the red-shaded ket from (e), and likewise for the blue-shaded kets.

photons are completely indistinguishable, the visibility would be $V = (\text{Max} - 0)/(\text{Max} + 0) = 1$, the maximum possible value of the visibility. Another useful metric is the coherence time of a photon, $\tau \equiv \lambda^2/c\Delta\lambda$, determined by its bandwidth, $\Delta\lambda$. In a HOM experiment, τ is the relative time delay over which the two photons display some destructive interference. More precisely, for gaussian pulses with bandwidth $\Delta\lambda$, τ is the relative delay for which the visibility drops to $1/e = 37\%$.

1.1.3 Measuring the D/A Visibility

Cycling back to our previous discussion, there are two possible creation processes for our polarized photons: $|H_{\omega_1} V_{\omega_2}\rangle$ and $|V_{\omega_1} H_{\omega_2}\rangle$. In order for the two processes to be entangled, they must be indistinguishable from each other. Let us consider the (unnormalized) two-qubit polarization state shown in Figure 1.3. In order for the state to be considered maximally entangled, it must take the form of $|\psi\rangle = |D_{\omega_1} D_{\omega_2}\rangle + |A_{\omega_1} A_{\omega_2}\rangle$ in the $\{D, A\}$ basis, as shown in Figure 1.3(a) when transformed using the equations in Figure 1.3(b). In order to achieve this entangled state in the $\{D, A\}$ basis, the red-shaded term from Figure 1.3(d) must cancel the red-shaded term from Figure 1.3(e), and likewise for the blue-shaded terms. The only way for these cancellations to happen is if these terms from Figure 1.3(d) and (e) are indis-
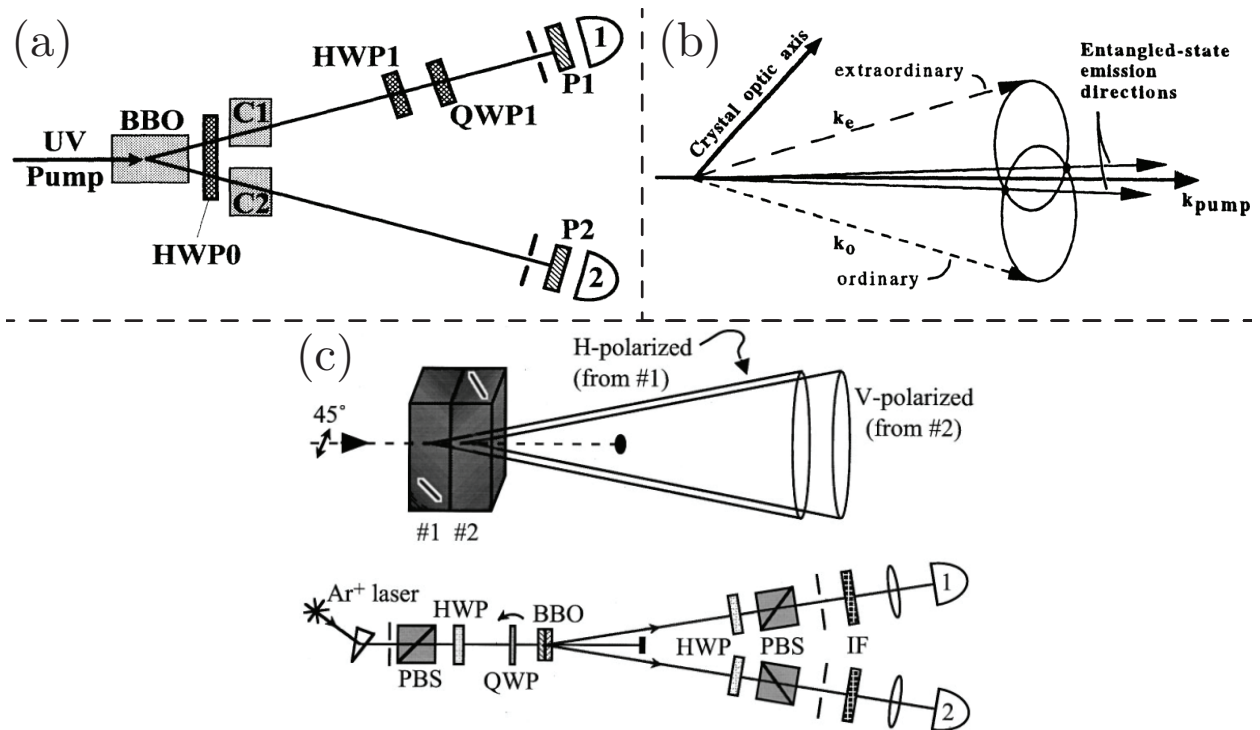
Figure 1.4: Traditional SPDC-based sources of polarization entanglement. (a) Experimental Setup and (b) light cones of SPDC source described in [13]. (c) Experimental Setup and light cones of SPDC source described in [14].

tinguishable. The ways in which these two terms can become more or less distinguishable will be discussed throughout this work.

1.1.4 Creating Polarization Entangled Photon Pairs

Photon pairs can be created (probabilistically) via a nonlinear optical process such as spontaneous parametric downconversion (SPDC), in which a high energy pump photon occasionally splits into two daughter photons (more details in Chapter 2)[¶]. Experimentally, we can create entangled photon pairs by combining two independent sources of photon pairs such that there is no information about which source produced a pair. Beginning in 1970 with the publication of *Observation of Simultaneity in Parametric Production of Optical Photon Pairs* by Burnham et al., SPDC has been a popular choice for creating either entangled photon pairs or heralded single-photons [15]. SPDC is popular because it is fairly straightforward and

---

[¶]Four-wave mixing is an alternative process, in which a pair of pump photons is converted into an entangled pair.

easy to implement, and produces photons naturally entangled in their spatial and temporal modes [16]. However, the optimal method to combine independent photon pair sources is still up for debate. Traditionally, SPDC-based polarization entanglement can be accomplished by using Type-II phase-matching (refer to Section 2.3) and slightly changing the pump angle with respect to the optic axis of the nonlinear crystal as shown in Figure 1.4(a) and (b) [13]. One can also use two bulk nonlinear crystals, where one's optic axis is rotated 90°, stacked against each other, as shown in Figure 1.4(c) [14]; here there are two equal probability amplitudes to produce two horizontally polarized photons from one crystal and two vertically polarized photons from the other. However, over the years, groups have proposed and implemented new creative sources of polarization entanglement that are meant to improve upon these original sources. Waveguide-based (Section 3.1), beam-displacer-based (Appendix A), and Sagnac-interferometer-based [17] sources all show promise. To give a recommendation on what source would be the most appropriate for our applications, i.e., aerial and space-based quantum communication, work has been done on these three types of sources, ultimately using the same lab space, pump laser, and detectors in order to directly compare the entanglement quality of each source.

Chapter 2

Designing a Spontaneous Parametric Downconversion Source of Photon Pairs

SPDC is a process that satisfies both energy and momentum conservation laws, in which one pump photon splits into two daughter photons within some nonlinear material (Figure 2.1). This event is the reverse of sum frequency generation (SFG), or second harmonic generation (SHG) in the case where the two daughter photons have degenerate wavelengths. The ability to produce pairs of photons that are highly correlated in time, space, and frequency allows for manipulation of quantum states for quantum information purposes; SPDC can produce pure single-photon states that are heralded by the other photon in the pair; detecting the heralding photon projects the other photon into a well-defined spatial and spectral-temporal mode [18]. These single photons can then be used in various quantum information processing applications that require single photons, as opposed to weak coherent light. More importantly to our goals, maximally entangled states can be created by combining photon pair creation amplitudes from two different nonlinear processes [13]. This entanglement can present itself in various forms such as polarization, OAM [10], and time bin [8]; however, this dissertation work will only focus on polarization-entangled photon pairs.

To begin, let us consider a single nonlinear crystal pumped by a bright laser made up of many ($\approx 10^{15}$ per second per mW of laser power depending on the wavelength) coherent photons. Due to the non-linearity of the crystal, roughly one in a billion (10^9) of these coherent photons will decay into two daughter photons, the "signal" and "idler", with frequencies ω_s and ω_i (though as we shall see, there can be a spread in each of these, just as there can for the frequency ω_p of the pump, e.g., with a pulsed source). In order to conserve energy, the sum of these frequencies, $\omega_s + \omega_i$, must equal ω_p; in order to conserve momentum, the sum of the momenta of the daughter photons must also equal that of the pump photon:

$$\vec{p}_s + \vec{p}_i = \hbar\vec{k}_s + \hbar\vec{k}_i = \hbar\vec{k}_p = \vec{p}_p, \tag{2.1}$$
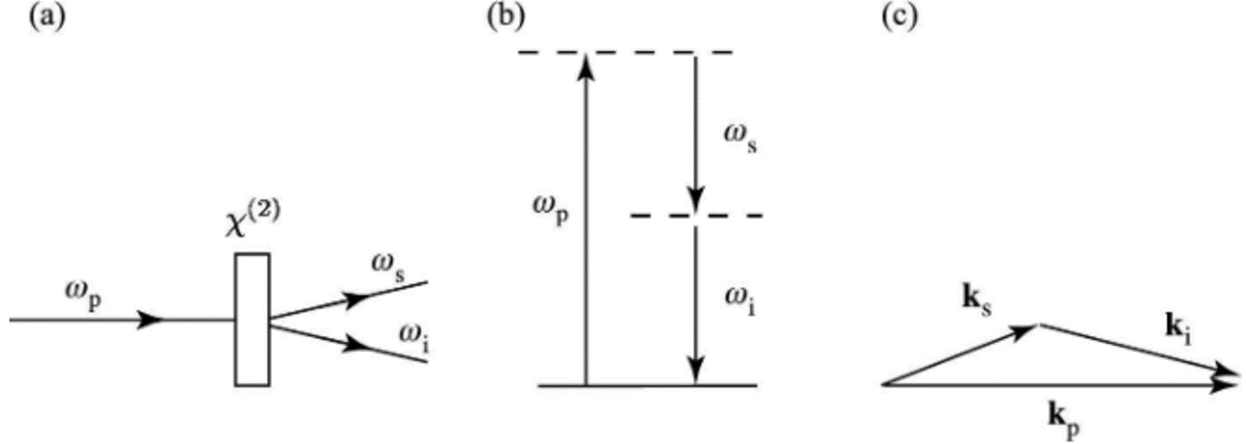
Figure 2.1: (a) A schematic of non-collinear SPDC with pump frequency, ω_p, signal frequency of ω_s, and an idler frequency of ω_i. (b) Energy-level diagram depicting energy conservation for SPDC. (c) Momentum-vector diagram depicting momentum conservation for SPDC (Figure from [19]).

where $|\vec{k}| = 2\pi n/\lambda$. This momentum or "phase"-matching can be accomplished through careful design of the nonlinear crystal and through choosing appropriate pump, signal, and idler frequencies (more on this later). Furthermore, depending on the "cut" of the crystal*, the daughter photons can be born into collinear modes, meaning they will exit the crystal along the same path, or non-collinear modes, meaning they exit the crystal in different paths separated by some angle. SPDC is a probabilistic process, meaning we cannot just push a button and deterministically produce a photon pair (at least not without external manipulation [18]); the photons produced via SPDC are actually governed by thermal statistics [20], so the maximum probability of producing a single pair is $\frac{1}{4}$.

2.1   Derivation of the SPDC Process

To understand the downconversion process on a deeper level, it is helpful to consider the relevant electric fields and their relationship to the polarization (or dipole moment per unit volume) of the nonlinear medium. A time-varying polarization $P(t)$ acts as the source of new components of the electric field [19]. Therefore, we can write the relationship between $P(t)$ and $E(t)$ as follows:

---

*The cut refers to the angle the crystal optic axis (axes for biaxial crystals) makes with respect to the pump beam direction, and affects the index of refraction for extraordinary-polarized light. Thus, altering the crystal cut can allow tuning to enable phase matching.

$$P(t) = \epsilon_0(\chi^{(1)}E_1(t) + \chi^{(2)}E_1(t)E_2(t) + \chi^{(3)}E_1(t)E_2(t)E_3(t) + \dots), \qquad (2.2)$$

where ϵ_0 is the permittivity of free space, $\chi^{(\cdot)}$ is the susceptibility coefficient, and $E(t)$ is the electric field [21]. For linear optics, only the first term is considered. This greatly simplifies our polarization equation to $P(t) = \epsilon_0\chi^{(1)}E_1(t)$. However, as we venture into the field of nonlinear optics, the higher-order terms become relevant. Specifically for SPDC, we must consider the second term (or first nonlinear term) in addition to the linear term: $P(t) = \epsilon_0(\chi^{(1)}E_1(t) + \chi^{(2)}E_1(t)E_2(t))$. This second-order nonlinear relationship shows us that for the materials used for SPDC, the induced polarization has a quadratic relationship to the electric field. Therefore, an electric field at frequency ω ($E_0 e^{-i\omega t}$) can produce a polarization response at 2ω, which in turn generates an electric field at 2ω. Classically this describes the well-known phenomenon of SHG. SPDC producing degenerate photons from a higher energy pump photon is essentially this process in reverse, though quantum noise is needed to 'seed' the process.

To model SPDC mathematically, we start with the electric field operators $\hat{\mathbf{E}}_p(\mathbf{r}, t)$, $\hat{\mathbf{E}}_s(\mathbf{r}, t)$, and $\hat{\mathbf{E}}_i(\mathbf{r}, t)$, corresponding to the electric field operators of the pump, signal, and idler modes, respectively, where $E \propto \hat{a} - \hat{a}^\dagger$, and $\hat{a}^\dagger$ and $\hat{a}$ are the photon creation and annihilation operators, respectively [22], obeying $a^\dagger|n\rangle = \sqrt{n+1}|n+1\rangle$ and $a|n\rangle = \sqrt{n}|n-1\rangle$. The field operators can be broken down into positive (+) and negative (−) frequency components that represent whether the photon is being emitted or absorbed. We can write down the Hamiltonian for the process as

$$\hat{H} = \int_V \epsilon_0 \chi^{(2)}(\mathbf{r})\hat{\mathbf{E}}_p^+(\mathbf{r}, t)\hat{\mathbf{E}}_s(\mathbf{r}, t)\hat{\mathbf{E}}_i(\mathbf{r}, t)d^3\mathbf{r} + \text{H.c.}, \qquad (2.3)$$

where V is the volume of the crystal, t is time, $\mathbf{r} = (x, y, z)$, H.c. is Hermitian conjugate, and all other symbols have been previously defined [23]. This Hamiltonian, which is directly proportional to the second-order nonlinear susceptibility, couples the electric fields of the three modes. Although there are nominally eight terms, only two of these satisfy energy conservation, corresponding to creating two down-conversion photons by annihilating one pump photon (the process we care about) and vice versa (sum-frequency generation). We

12

can use the following definition for the electric field:

$$\hat{\mathbf{E}}(\mathbf{r}, t) = \int_0^\infty \sqrt{\frac{\hbar\omega}{2\epsilon_0}} \mathbf{E}_\omega(\mathbf{r}) e^{-i\omega t} \hat{a}_\omega d\omega, \tag{2.4}$$

where $\mathbf{E}_\omega(\mathbf{r})$ is the spatial mode of the (e.g., gaussian) electric field and $\hat{a}_\omega$ is the annihilation operator for a photon in that mode. The hermitian conjugate of the annihilation operator, $\hat{a}_\omega^\dagger(t)$ is called the creation operator and when applied, creates a photon in the given mode. We can write down the complete Hamiltonian by combining Equations 2.3 and 2.4 as follows:

$$\hat{H} = \int \epsilon_0 \chi^{(2)}(\mathbf{r}) \left(\int_0^\infty \sqrt{\frac{\hbar\omega_p}{2\epsilon_0}} \mathbf{E}_p(\mathbf{r}) e^{-i\omega_p t} \hat{a}_p d\omega_p \right. $$
$$\left. \int_0^\infty \sqrt{\frac{\hbar\omega_s}{2\epsilon_0}} \mathbf{E}_s^*(\mathbf{r}) e^{i\omega_s t} \hat{a}_s^\dagger d\omega_s \int_0^\infty \sqrt{\frac{\hbar\omega_i}{2\epsilon_0}} \mathbf{E}_i^*(\mathbf{r}) e^{i\omega_i t} \hat{a}_i^\dagger d\omega_i \right) d^3\mathbf{r}. \tag{2.5}$$

Since our ω- and $\mathbf{r}$-dependent terms are independent of each other, we can separate the triple integral into the product of three single integrals,

$$\hat{H} = \left(\frac{\hbar}{2\epsilon_0}\right)^{3/2} \epsilon_0 \int \chi^{(2)}(\mathbf{r}) \mathbf{E}_p(\mathbf{r}) \mathbf{E}_s^*(\mathbf{r}) \mathbf{E}_i^*(\mathbf{r}) \, d^3\mathbf{r}$$
$$\int_0^\infty \sqrt{\omega_p} \, e^{-i\omega_p t} \, \hat{a}_p \, d\omega_p \int_0^\infty \sqrt{\omega_s \omega_i} \, e^{i(\omega_s + \omega_i)t} \, \hat{a}_i^\dagger \, \hat{a}_s^\dagger \, d\omega_s d\omega_i. \tag{2.6}$$

We then define a function, $\Omega(\omega_s, \omega_i) \equiv \int_{medium} \chi^{(2)}(\mathbf{r}) \mathbf{E}_p(\mathbf{r}) \mathbf{E}_s^*(\mathbf{r}) \mathbf{E}_i^*(\mathbf{r}) \, d^3\mathbf{r}$, which describes the overlap and phase-matching of the pump, signal, and idler electric fields, and simplify the Hamiltonian:

$$\hat{H} = \epsilon_0 \left(\frac{\hbar}{2\epsilon_0}\right)^{3/2} \int_0^\infty \sqrt{\omega_p} \, e^{-i\omega_p t} \, \hat{a}_p \, d\omega_p \int_0^\infty \Omega(\omega_s, \omega_i) \sqrt{\omega_s \omega_i} \, e^{i(\omega_s + \omega_i)t} \, \hat{a}_i^\dagger \, \hat{a}_s^\dagger \, d\omega_s d\omega_i. \tag{2.7}$$

Now that we have written down the Hamiltonian, we can go ahead and apply it to our initial state. To do so, we can expand the time-evolution equation to give the state after some time t:

$$|\Psi_{\text{spdc}}(t)\rangle = \exp\left[-\frac{i}{\hbar}\int_0^t \hat{H}(t)\,dt\right]|0_i\rangle|0_s\rangle \approx \left(1 - \frac{-i}{h}\int_0^t \hat{H}(t)\,dt\right)|0_s\rangle|0_i\rangle. \qquad (2.8)$$

The right-side Taylor-series approximation here is made assuming we are in the weak-pump regime and can ignore any possibility of multiple-pair events. Additionally, we assume we are in the regime of a non-depleted coherent-state pump, and the two downconversion fields are initially assumed to start in the vacuum state. The first step is to take the integral of the time-dependent part of the Hamiltonian:

$$\int_0^t e^{-i\omega_p t} e^{i(\omega_s+\omega_i)t} dt \approx \delta\left(\frac{\omega_p - \omega_i - \omega_s}{\pi}\right). \qquad (2.9)$$

Next, we evaluate the ω_p integral.

$$\int_0^\infty \sqrt{\omega_p}\,\delta\left(\frac{\omega_p - \omega_i - \omega_s}{\pi}\right)d\omega_p = \pi\sqrt{\omega_i + \omega_s} \quad \text{if} \quad \omega_i + \omega_s > 0. \qquad (2.10)$$

Finally, we can combine Equations 2.7–2.10 and find the following SPDC state:

$$|\Psi_{\text{spdc}}\rangle = \epsilon_0 \frac{-i}{\hbar}\left(\frac{\hbar}{2\epsilon_0}\right)^{3/2}\int_0^\infty \Omega\left(\omega_s,\omega_i\right)\pi\sqrt{\omega_s\,\omega_i\left(\omega_s+\omega_i\right)}\,\hat{a}_p\,\hat{a}_s^\dagger\,\hat{a}_i^\dagger\,|0_s\rangle|0_i\rangle\,d\omega_s d\omega_i. \qquad (2.11)$$

We can also replace the pump annihilation operator, $\hat{a}_p$, by assuming that our pump is a high-power laser and therefore a classical state,

$$\hat{a}_p \equiv s\left(\omega_p\right)\sqrt{N_p} \qquad (2.12)$$

where $s(\omega_p)$ is the spectral amplitude (or probability distribution over its composite frequencies) of the pump and N_p is the mean number of pump photons. Plugging Equations 2.12 into Equation 2.11, and using energy conservation ($\omega_s + \omega_i = \omega_p$), from (2.9) our SPDC state becomes,

$$|\Psi_{\text{spdc}}\rangle = \epsilon_0 \frac{-i}{\hbar}\left(\frac{\hbar}{2\epsilon_0}\right)^{3/2}\int_0^\infty s\left(\omega_p\right)\sqrt{N_p}\,\Omega\left(\omega_s,\omega_i\right)\pi\sqrt{\omega_p\,\omega_s\,\omega_i}\,\hat{a}_s^\dagger\,\hat{a}_i^\dagger\,d\omega_s d\omega_i\,|0_s\rangle|0_i\rangle \qquad (2.13)$$

We then define our SPDC amplitude, $\psi(\omega_s, \omega_i)$, as follows:

$$\psi(\omega_s, \omega_i) \equiv \sqrt{\frac{\hbar}{8\,\epsilon_0}}\,\Omega(\omega_s, \omega_i)\,s(\omega_p)\,\sqrt{N_p}\,\pi\sqrt{\omega_p\,\omega_s\,\omega_i}$$
$$= \sqrt{\frac{N_p\pi^2\hbar\,\omega_p\,\omega_s\,\omega_i}{8\,\epsilon_0}}\,\Omega(\omega_s, \omega_i)\,s(\omega_p), \tag{2.14}$$

which gives us a final, simplified state where the two creation operators act on the vacuum state, forming an entangled photon pair with the above-defined SPDC amplitude:

$$|\Psi_{\text{spdc}}\rangle = -i\int_0^\infty \psi(\omega_s, \omega_i)\,\hat{a}_s^\dagger \hat{a}_i^\dagger d\omega_s d\omega_i |0_s\rangle|0_i\rangle. \tag{2.15}$$

2.2 Spectral Amplitude of the Downconversion Process

The overlap function that we described in Section 2.1 is the starting point for determining the spectral intensity of our downconversion photons. The overlap gives us the probability amplitude to create a photon pair with frequencies ω_i and ω_s. It is assumed that our photons are in co-propagating Gaussian modes. By integrating the overlap function over the entire length of the crystal, we can determine a function for the probability amplitude of the downconversion process. Due to the relationship between k and λ ($|\vec{k}| = 2\pi n/\lambda$), we can also derive the relationship between the downconversion intensity and wavelengths.

To begin, the electric fields of our pump, signal, and idler photons can be written in the form of $E(z,t) = A\,e^{i(kz-\omega t)}$. For simplicity here we assume that phase-matching is collinear and that the nonlinear susceptibility, $\chi^{(2)}$, is not **r**-dependent, meaning we have a uniform crystal and only have to integrate over the z-axis, i.e., over the length L of the crystal. These assumptions give the following overlap function:

$$\Omega(\omega_s, \omega_i) = A_p A_s^* A_i^* \chi^{(2)} \int_{-L/2}^{L/2} e^{i(k_p z - \omega_p t)} e^{-i(k_s z - \omega_s t)} e^{-i(k_i z - \omega_i t)}\,dz, \tag{2.16}$$

where A is some complex constant, and all other variables have been previously defined. We can combine the exponents and pull the time-dependent terms out of the integral and treat

them as a part of a new overall complex constant, C:

$$\Omega\left(\omega_s, \omega_i\right) = A_p A_s^* A_i^* \chi^{(2)} e^{-i(\omega_p t - \omega_s t - \omega_i t)} \int_{-L/2}^{L/2} e^{i(k_p z - k_s z - k_i z)} \, dz$$
$$= C \, e^{-i(\omega_p t - \omega_s t - \omega_i t)} \int_{-L/2}^{L/2} e^{i(\Delta k z)} \, dz, \tag{2.17}$$

where we have defined the momentum mismatch $\Delta k = k_p - k_s - k_i$. We can now complete the integral and then take the absolute-square to find the spectral intensity of the downconversion process. Integrating $e^{-i(\omega_p t - \omega_s t - \omega_i t)}$ over time leads to a delta function in frequency ($\delta(\omega_p - \omega_s - \omega_i)$), i.e., energy conservation.

$$I = \left| C \int_{-L/2}^{L/2} e^{i(\Delta k z)} \, dz \right|^2 = |C|^2 \left| \frac{e^{i\,\Delta k L/2} - e^{-i\,\Delta k L/2}}{i\Delta k} \right|^2$$
$$|C|^2 \left(\frac{\sin \Delta k L/2}{\Delta k/2} \right)^2 = |C|^2 L^2 \operatorname{sinc}^2(\Delta k L/2), \tag{2.18}$$

the quintessential downconversion intensity profile in the form of sinc^2, plotted in Figure 2.2 [19]. In order for efficient downconversion, the phase-matching (i.e., momentum conservation) conditions must be met. Since k is inversely proportional to the wavelength λ, Equation 2.18 also shows that the spectral intensity (that is, the downconversion intensity with respect to the wavelength of the signal or idler photon) will take the approximate form of a sinc-squared function for small bandwidths. This intensity equation also gives information about the relationship between the bandwidths $\delta\lambda_s$ and $\delta\lambda_i$ of the signal and idler photons and the crystal length L. Using $\delta k = -2\pi\delta\lambda/\lambda^{2\dagger}$ and therefore $\delta k L\,/2 = -\pi\delta\lambda L/\lambda^2$, we find that the bandwidth of the downconversion spectra is inversely proportional to the length of the crystal.

---

†We switch here to using lowercase δ to avoid confusion. This δk is different than Δk; δk relates to only one photon's wavelength (the spread in k), whereas Δk refers to the relationship between the k-vectors of the pump, signal, and idler.
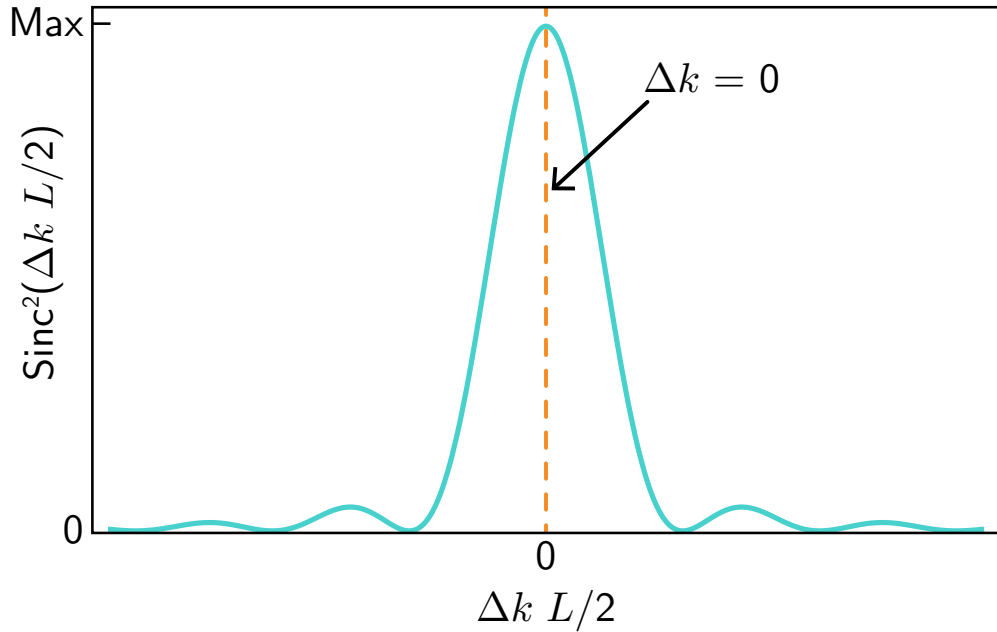
Figure 2.2: The downconversion spectral intensity with respect to the phase mismatch. The vertical dashed line marks the point in the spectrum where the phase mismatch is zero, which is where maximum downconversion efficiency is achieved. There will only be appreciable downconversion when $\Delta L/2 < \pi$.

2.3 (Quasi) Phase-Matching in Nonlinear Crystals

We can rewrite the phase-matching condition using the relation between momentum (k-vector) and frequency:

$$k(\omega, \text{pol}) \equiv \frac{2\pi}{\lambda} = \frac{2\pi\, n(\omega, \text{pol})\, \omega}{c}, \tag{2.19}$$

where "pol" refers to the polarization of the photon (not to be confused with the polarization, $P(t)$, of the nonlinear medium), λ is the (vacuum) wavelength of the photon, n is the frequency- and polarization-dependent index of refraction of the nonlinear crystal, and c is the speed of light. There are three types of polarization-based phase-matching to consider:

Type-0 Phase-Matching: $n_p^o \omega_p = n_s^o \omega_s + n_i^o \omega_i$ **or** $n_p^e \omega_p = n_s^e \omega_s + n_i^e \omega_i$ (2.20)

Type-I Phase-Matching: $n_p^o \omega_p = n_s^e \omega_s + n_i^e \omega_i$ **or** $n_p^e \omega_p = n_s^o \omega_s + n_i^o \omega_i$ (2.21)

Type-II Phase-Matching: $n_p^o \omega_p = n_s^o \omega_s + n_i^e \omega_i$ **or** $n_p^e \omega_p = n_s^o \omega_s + n_i^o \omega_i$ (2.22)

where n is the index of refraction, the o superscript refers to the polarization being along the ordinary axis (perpendicular to the optic axis of the crystal), the e superscript refers to the polarization being along the extraordinary axis (with a component parallel to the optic axis of the crystal)[‡], and p, s, and i refer to the pump, signal, and idler, respectively. Thus, when ordering a downconversion crystal, it is necessary to specify both the desired pump and daughter photon wavelengths and the phase-matching type desired. For example, one of the crystals used in this thesis work takes a 532-nm pump and downconverts it into a nondegenerate photon pair at a nominal signal wavelength of 1550 nm and an idler wavelength of 810 nm using Type-II phase-matching; the resulting state is

$$|\psi\rangle = |H_{810}\rangle \otimes |V_{1550}\rangle, \qquad (2.23)$$

where H and V correspond to the ordinary and extraordinary polarizations of the downconversion photons, respectively, and the subscripts refer to their wavelengths.

An additional consideration when designing an SPDC crystal is the exit angle of the downconversion photons. For our purposes, a 0° (collinear) exit angle is preferred (more on this later). However, a non-zero exit angle is often required. Applications that necessitate a non-zero exit angle include ghost imaging experiments, where one photon is used to scatter off an object [24], and degenerate photon experiments where the downconversion photons have equal frequencies and therefore would be impossible to separate deterministically, e.g., using a dichroic mirror (DM) [13]. In either case, the downconversion photons must satisfy momentum conservation, Equation 2.1.

Although any nonlinear crystal can theoretically create entangled photon pairs through

---

[‡]Changing the crystal cut changes the angle between the optic axis and the extraordinary polarization vector, and thereby the index of refraction that the extraordinary component experiences.
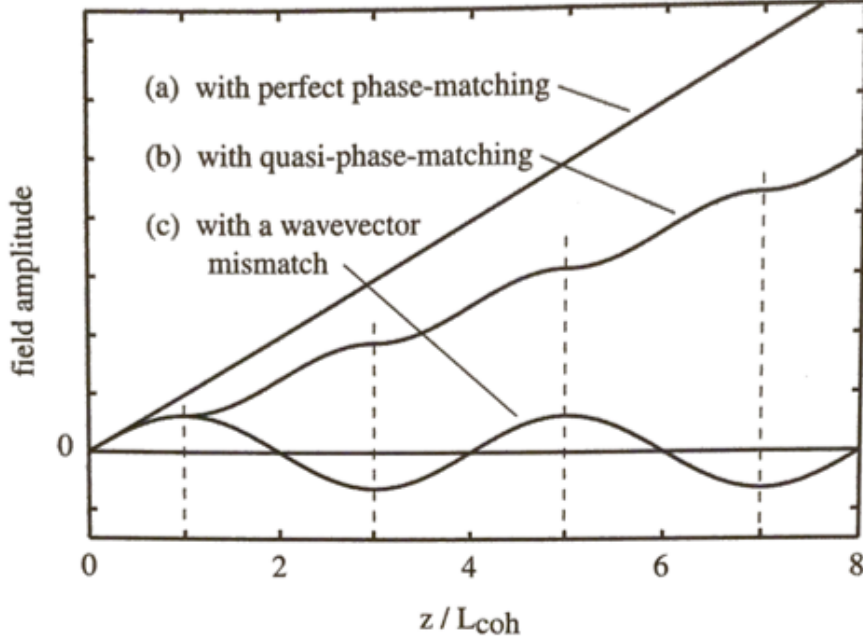
Figure 2.3: The downconversion electric field amplitude with respect to the length of the crystal in units of the field coherence length within the crystal. With perfect phase-matching (inherent to the crystal) the downconversion electric field amplitude increases linearly over the length of the crystal (so the downconversion probability would increase as L^2. With no phase-matching, the average downconversion amplitude averages to zero: the downconversion photons are continually converted back into the pump. Finally, with QPM, the process is less efficient than with perfect phase-matching, but the downconversion field amplitude still increases over the entire length of the crystal (Figure from [19]).

SPDC, not all nonlinear materials are equally useful for specific applications. The pump and daughter photon specifications required for phase-matching (and therefore efficient pair production) within a specified nonlinear crystal may not be well suited for the desired application. Or, the application may require frequency and polarization combinations that only naturally fulfill the phase-matching requirements in a less accessible (in terms of cost, availability, or ease-of-use) nonlinear crystal. To circumvent these potential issues, nonlinear crystals can be periodically poled in such a way that phase-matching can be achieved even with light that would not normally satisfy momentum conservation requirements. This periodic poling allows "quasi-phase-matching" (QPM) and is accomplished by reversing the crystal domain orientation, which effectively flips the sign of $\chi^{(2)}$ over a certain length of the crystal at a period, Λ, determined by the necessary QPM[§]. The effect of this is shown in

---

[§]Originally, periodic poling was accomplished as the crystal was growing; however, this method was too imprecise. Now, poling is instead done on a pre-made crystal using lithography. One way to accomplish this type of poling is to use lithography to diffuse dopants or force ion-exchanges in marked areas. This method
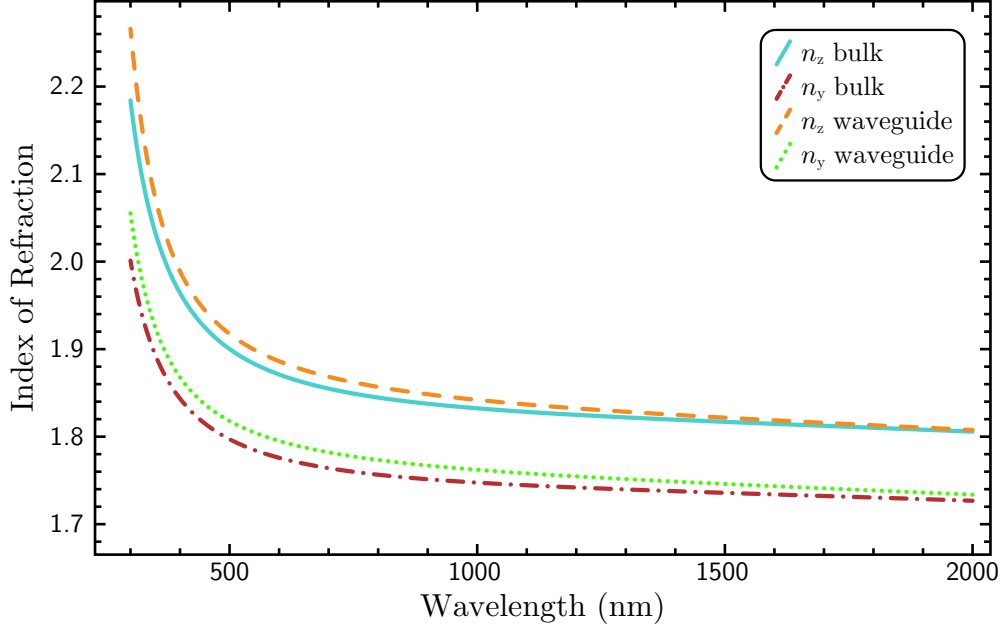
Figure 2.4: Calculated values of the polarization-dependent indices of refraction for bulk KTP and waveguides[||] in KTP [25]. The z (y) subscript corresponds to photons polarized parallel (perpendicular) to the ordinary axis in the crystal. The red (dash-dotted) and blue (solid) lines represent the index of refraction versus vacuum wavelength ($\equiv c/f$) in a bulk crystal, whereas the orange (dashed) and green (dotted) lines represent the index of refraction in a particular waveguide.

Figure 2.3; instead of the downconversion electric field amplitude generated over the length of the crystal averaging to zero when phase-matching is not satisfied[¶], QPM enables the amplitude to increase monotonically over the length of the crystal. Commonly poled crystals include lithium niobate (periodically poled lithium niobate, PPLN - pronounced pip-lynn) and potassium titanyl phosphate (ppKTP).

The poling period is calculated by determining the intrinsic phase mismatch Δk within the crystal at the given photon frequencies and polarizations. This dependence arises specifically because the refractive index of the (birefringent) nonlinear crystal depends on the frequency and polarization of the light. An example of $n(\omega, \text{pol})$ as determined by the Sellmeier equation[**] of the material is shown in Figure 2.4). Note that if a waveguide is used,

---

is less common due to its inability to pole deeper than a few microns; however, it can still be used effectively for schemes where SPDC takes place in a waveguide on the surface of a substrate. The most common way of poling a crystal is to use lithography to place electrodes on the crystal. An electric field pulse is applied to these electrodes, permanently forcing the sign of the nonlinear coefficient of the material to flip in the specific area.

[¶]Effectively, the nonlinear process oscillates between downconversion ($\omega_p \to \omega_s + \omega_i$) and upconversion ($\omega_s + \omega_i \to \omega_p$).

[**]The Sellmeier equation of a material is an empirical measure of the the index of refraction of the material

in addition to the (bulk) crystal structure itself affecting the refractive index, it will also depend on the geometry of the waveguide (transverse dimensions, surrounding material's refractive index, etc.; in general it will need to be measured empirically. Periodic poling can be used to compensate for imperfect phase-matching ($k_p \neq k_s + k_i$); This adds an additional term to the phase-matching condition:

$$\Delta k = k_p - k_s - k_i + \Delta K \tag{2.24}$$

where $\Delta K \equiv 2\pi/\Lambda$, and Λ is the poling period required for QPM. To determine the optimal value of Λ, and thus ΔK, required to satisfy the phase-matching condition, $\Delta k = 0$, one must consider the specifications of the application both in terms of frequency and polarization.

2.4 Group Velocity Walk-Off

One consequence of the wavelength- and polarization-dependent index of refraction is that our photon wave packets can travel at different group velocities within the crystals if they have different wavelengths and/or polarization. Consequently, the photons within a pair can exit the crystal at different times. As will become clear in our discussion of creating polarization-entangled photon pairs, this group velocity walk-off will need to be corrected; therefore, it is necessary to understand how to calculate this walk-off.

To begin, we will need to calculate the group velocity of each photon wavepacket. The group velocity of one photon is defined as follows [26]:

$$v_g \equiv \frac{d\omega}{dk} = \frac{c}{n - \lambda_0 \frac{dn}{d\lambda_0}}, \tag{2.25}$$

where c is the speed of light in vacuum, $\lambda_0 \equiv \frac{2\pi c}{\omega}$ is the wavelength of the photon in vacuum, and n is the index of refraction given λ_0. The value of the group velocity can be calculated numerically using known values of the index of refraction of the material for different wavelengths and polarization, e.g., as shown by the plot of the Sellmeier equation in Figure 2.4.

---

experienced by light with a specified frequency (or wavelength) and polarization. The Sellmeier equation will be discussed further in Section 2.4.

The Sellmeier equation is an empirical measure of the index of refraction's dependency on wavelength and polarization. It is a purely experimental measure and is determined by measuring the index of refraction for a series of wavelength values in multiple samples and then implementing the method of least squares to fit the curve [27]. When ordering a birefringent material, typically the manufacturer will provide the Sellmeier equation of their specific product. In general, the Sellmeier equation takes the form

$$n^2(\lambda_0) = 1 + \sum_i \frac{B_i \lambda_0^2}{\lambda_0^2 - C_i}, \tag{2.26}$$

where B_i and C_i are experimentally determined values specific to the material, and each term of the sum represents a peak in the absorption spectrum of the material; note that these coefficients in general also depend on temperature.

Once the Sellmeier equation is known, to approximate $dn/d\lambda_0$ numerically, we can simply take the difference in the values of n for λ_0 and λ_0+1 (in nanometers) divided by the difference in wavelength:

$$v_g \approx \frac{c}{n - \frac{\lambda_0}{\lambda_0 - (\lambda_0 + 1)}(n(\lambda_0) - n(\lambda_0 + 1))}. \tag{2.27}$$

Depending on the situation, the group velocity of the pump may also need to be determined; however, for this calculation we will use the simple case of a single type-II phase-matched, nondegenerate downconversion process, where a pump photon downconverts into a signal photon with frequency, ω_s, polarized along the ordinary axis, and an idler photon with frequency, ω_i, polarized along the extraordinary axis. Since they are formed as a pair, these two photons will be created at the same point in the crystal and will travel over the same distance. The crystal birefringence is assumed to be uniform over the entire path of the photons. From the group velocity, we can use basic kinematics, $t = l/v_g$, to solve for the difference in exit times of the two photons of a pair:

$$\Delta t = t_s - t_i = l/v_{g,s} - l/v_{g,i}, \tag{2.28}$$

where s and i represent the signal and idler photons, respectively, and l is the length of the

path through which the photons travel. When performing these calculations, l is determined based on the crystal and poling geometry. For the proposed simple case, the photon pairs, on average, will be created at the center of the crystal. Of course, the photon pairs are created throughout the crystal; however, since we are assuming a uniform downconversion efficiency over the entire crystal, we can say on average that all the photons are born at the center, i.e., the photons born at the input of the crystal will travel through the entire length L of the crystal, whereas the photons born at the end of the crystal will essentially travel through no part of the crystal, giving an average length through which the downconverted photons travel, $(L + 0)/2 = L/2$. A more complete - and proper - justification of this simplifying assumption is given in [28] and [29]. Therefore, if the crystal length is L, then $l = L/2$. Group velocity walk-off in more involved sources involving polarization entanglement will be discussed in Section 3.2.2.

Once we have Δt, we can then correct for the group velocity walk-off by using a second birefringent material with the necessary length to re-overlap the two photons' wavepackets [30]. For this "temporal compensation" crystal we typically use calcite ($CaCO_3$) or quartz (SiO_2) due to ease of use and off-the-shelf availability. To find the correct length, we again determine the group velocities for our photons in the material of our temporal compensation crystal using the material's Sellmeier equations, and then use the previously calculated Δt such that $l_{c.c.} = \Delta t \, (1/v_{g,s} - 1/v_{g,i})^{-1}$, where $l_{c.c.}$ is the width of the compensation crystal. After this correction the photons from the same pair should travel together synchronously through space. As a final note, this specific scheme is not necessarily realistic; we almost never need to have the signal photon temporally compensated with respect to the idler photon. As will be shown in Section 3.2.2, we typically need to compensate the idler photons of two processes and the corresponding signal photons; however, this example highlights what *can* happen when two photons of differing polarization and/or wavelength travel through an SPDC crystal.
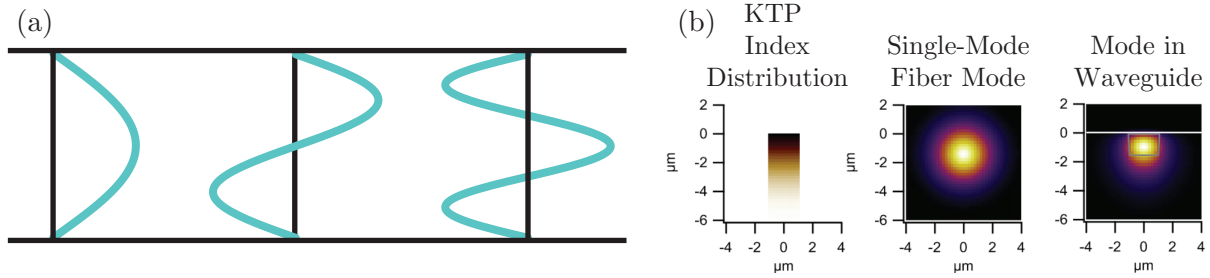
Figure 2.5: Waveguides work by restricting light to discrete modes within a channel. (a) A schematic of the zeroth, first, and second possible modes for light in a waveguide [31]; in this simplified 1-D example we assume the waveguide boundary conditions force the electric field to vanish at the walls. (b) In reality the confinement is usually much weaker ($n_{\mathrm{waveguide}} = n_{\mathrm{surrounding}} + \delta n$, $\delta n << 1$), so that the mode leaks into the surrounding material. The KTP index distribution is how the index changes with respect to the depth of the material. As will be discussed in Chapter 3, the waveguide is created by absorption of Rb^+ ions in specified areas and as such the amount of the Rb^+ ions absorbed by the bulk material will decrease with depth.

(a) Fully Embedded Waveguide   (b) Channel Waveguide   (c) Ridge Waveguide
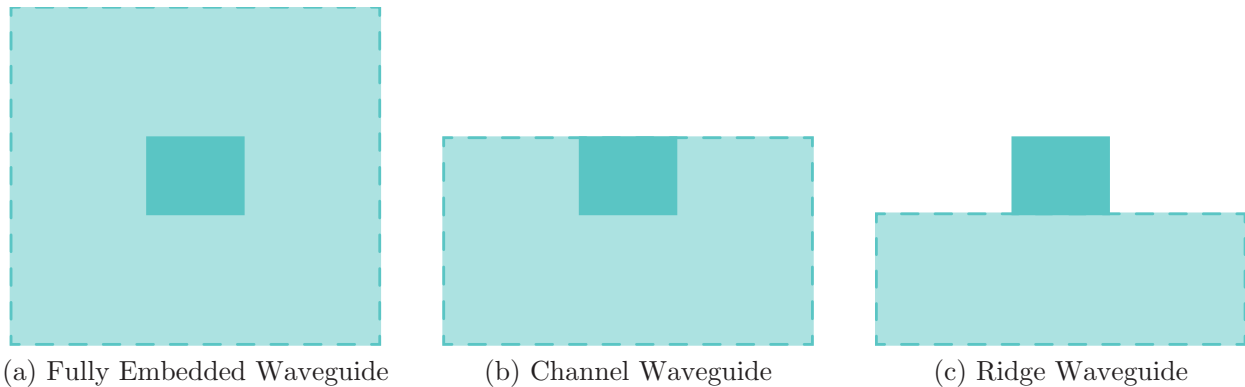
Figure 2.6: A schematic of different types of waveguides in nonlinear crystals. (a) A fully embedded waveguide where all four sides of the waveguide are surrounded by the bulk material. (b) A channel waveguide where three of the four sides of the waveguide are surrounded by the bulk material and one side is open to the surrounding environment ($n \approx 1$); this is usually created by diffusion of, e.g., Rb^+ ions into the material, leading to a region of (slightly) higher index of refraction, and thus transverse made confinement. (c) A ridge waveguide where one of the four sides of the waveguide are surrounded by the bulk material and three sides are open to the surrounding environment ($n \approx 1$).

2.5 A Note on Waveguide SPDC Sources

Waveguides work by constraining the modes of the light through channels with a higher index of refraction from the surrounding substrate (see Figure 2.6 for schematics of possible waveguide designs). If the waveguide is embedded in the substrate, the difference in refractive index may be quite small ($\Delta n \approx 0.01$), leading to fairly weak confinement. For a "ridge" waveguide, the surrounding medium on three sides is air, so that $\Delta n \approx n_{\mathrm{material}}$. Depending on the width of the waveguide channel, it can support a discrete number of modes given the wavelength of the guided light. A visual of these modes is shown in Figure 2.5. Therefore, when a pump photon downconverts in a waveguide, the daughter photons will be created in these discrete modes. Furthermore, since the pump frequency in SPDC is going to be higher than the signal and idler frequencies, the pump photon will naturally be able to exist in higher-order modes. The consequence of this shows up in the overlap term, $\Omega(\omega_1, \omega_2)$, from Section 2.1. For a waveguide, the electric field of the guided light can now be described as follows,

$$\hat{E}_{\mathrm{x}}^+ = A \sum_j f_{\mathrm{x}}^j(x,y) \int d\omega_{\mathrm{x}} e^{i(k_{\mathrm{eff,x}}^j(\omega_{\mathrm{x}})z - \omega_{\mathrm{x}} t)} \hat{a}_{\mathrm{x}}^j(\omega_{\mathrm{x}}), \tag{2.29}$$

where j labels the spatial mode of the light, the subscript x labels the signal, idler, and pump photons, $f(x,y)$ is the individual transverse-spatial-mode distribution over spatial coordinates x and y, and k_{eff} is the effective k-vector for the guided light [31]. If we use this new electric field definition from Equation 2.29 in the derivation outlined in Section 2.1, we end up with an overlap integral that contains the transverse spatial-mode distributions for each of the photons (pump, signal, and idler) in the SPDC interaction:

$$A_{klm} = \int \int f_{\mathrm{p}}^k(x,y) f_{\mathrm{s}}^l(x,y) f_{\mathrm{i}}^m(x,y) dx\, dy. \tag{2.30}$$

The consequence of A_{klm} is a change in the spectral distribution of the downconversion photons [32]: if the three spatial modes are well overlapped, then the downconversion process will be highly efficient. However, if the modes are slightly non-overlapping, the efficiency will decrease. Furthermore, since we are working with discrete modes, secondary peaks
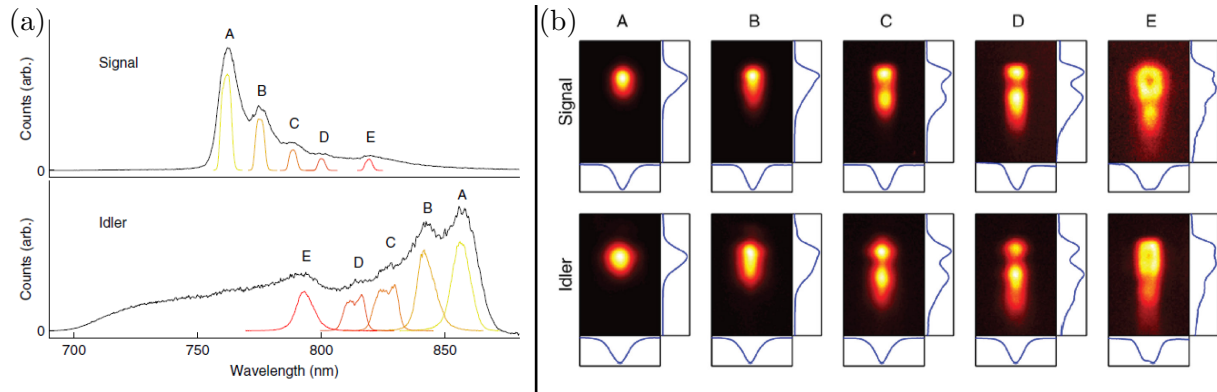
Figure 2.7: (a) Secondary peaks in the spectrum of SPDC in a channel waveguide. These peaks are caused by discrete SPDC modes interfering constructively along the waveguide channel. (b) Output spatial modes of the resulting signal and idler photons, measured using a charge-coupled device (CCD) camera (Figures from [32]).

can arise in the downconversion spectrum, from locations where the three modes interact constructively, as shown in Figure 2.7(a). Figure 2.7(b) shows images of the output modes from a ppKTP channel waveguide for different spectral pairs.

Chapter 3

Characterization of a Waveguide-Based Highly Nondegenerate Source of Polarization Entanglement

To create entangled photon pairs, we combine two independent SPDC photon pair source possibilities in such a way where all distinguishing information is lost. This means that when a photon is detected, we have no information about which source that photon came from. For example, two photon pair sources with type-II phase-matching could give us the polarization-entangled state, $|\psi\rangle = |HV\rangle + |VH\rangle$, where one source creates the $|HV\rangle$ process that is indistinguishable (either inherently or through various compensation) from the $|VH\rangle$ process made by the other source. There are multiple source geometries to create such SPDC-based sources of polarization-entangled photon pairs; we consider three: waveguide-based; beam-displacer-based (Appendix A) ; and Sagnac-interferometer-based [17]. At first glance, each of these three geometries may have obvious advantages - the waveguide source is brighter (more pairs per second per mW of pump power) than a bulk source and its small package is ideal for applications with stringent weight requirements; the beam displacer source alleviates the need for any additional compensation of the group velocity walkoff as discussed in Section 2.4; and the Sagnac source is well established and has been successful on complicated experiments such as the distribution of entanglement from space to Earth by Jian-Wei Pan's group [7]. However, when it comes to the entanglement quality and the absolute brightness of the source*, it is not immediately obvious which source is superior. The sources mentioned in this comparison feature nominal downconversion wavelengths of 810 nm (370 THz) and 1550 nm (193 THz), all created by a bright ($\sim$mW) pump laser at 532 nm (563 THz) in order to conserve energy. The wavelengths are selected to benefit the chosen application: satellite-based quantum communication. For the envisioned application,

---

*For instance, a bulk source may be able to withstand higher pump power, and thus have a higher absolute brightness than a waveguide source; also, the latter may have higher outcoupling losses, leading to a reduced effective brightness.
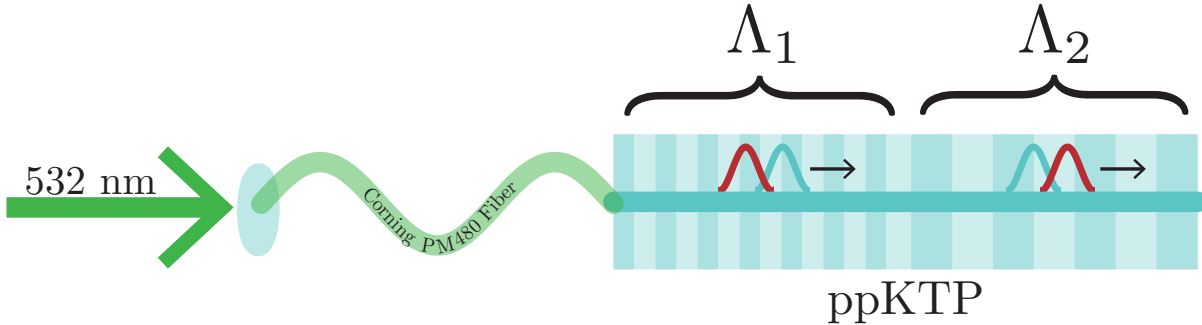
Figure 3.1: Consecutive Poling of a Waveguide SPDC Source: the waveguide-based entanglement source uses a consecutive poling schemed developed by AdvR. The first half of the periodically poled KTP crystal is poled with poling period $\Lambda_1 = 27$ μm to create the $|H_{810}V_{1550}\rangle$ process; the second half is poled with period $\Lambda_2 = 58$ μm to create the $|V_{810}H_{1550}\rangle$ process. One version of this waveguide source includes a fiber-pigtailed input as shown.

the entanglement source is located on a satellite in orbit. The 810-nm (signal) photon will remain on the satellite, whereas the 1550-nm (idler) photon will be collected at a ground station on Earth. The advantage of using a telecom ($\approx$1550 nm) wavelength for collection on Earth is that there is already existing infrastructure for sending this wavelength between Earth stations and satellites. Finally, detecting 810-nm photons requires comparatively few resources when it comes to size and weight. For example, Si Avalanche Photodiodes are small, plug-and-play, and work at room temperature[†]. As another application of such a non-degenerate source, the long-wavelength may be transmitted with minimum loss through an optical fiber, while the short-wavelength couples to a quantum memory. This chapter will include a detailed discussion of how to characterize and optimize SPDC-based photon pair sources, using the waveguide-based photon pair source as an example. Appendix A will describe the beam-displacer source.

3.1 AdvR Nondegenerate Waveguide Sources

Waveguides in nonlinear crystals are a popular choice for creating photon pairs through SPDC, and multiple groups have shown that degenerate (where the daughter photons are equal in frequency) or near-degenerate polarization entanglement in a waveguide is possible

---

[†]The detector module is designed to operate at room temperature, but the detectors themselves are locally cooled to $-20°$ C with thermoelectric coolers.

[30, 33–35]. However, highly nondegenerate polarization entanglement using SPDC has been proposed [36], but not previously demonstrated from a waveguide source. By helping develop the first-ever such source, we strive to make available bright, compact, and stable sources for advanced quantum communication protocols. We have thus characterized an SPDC-based source of highly nondegenerate polarization-entangled photon pairs on a waveguide designed and fabricated by AdvR [25] for applications where SWaP requirements are strict. For example, for quantum communication protocols between drones, a small, plug-and-play device capable of producing photon pairs at sufficient rates to tolerate loss in the atmosphere is ideal. Furthermore, a fully integrated waveguide source that would survive a rocket launch without need for remote re-alignment on arrival in orbit could be a critical resource for future satellite-based quantum communication.
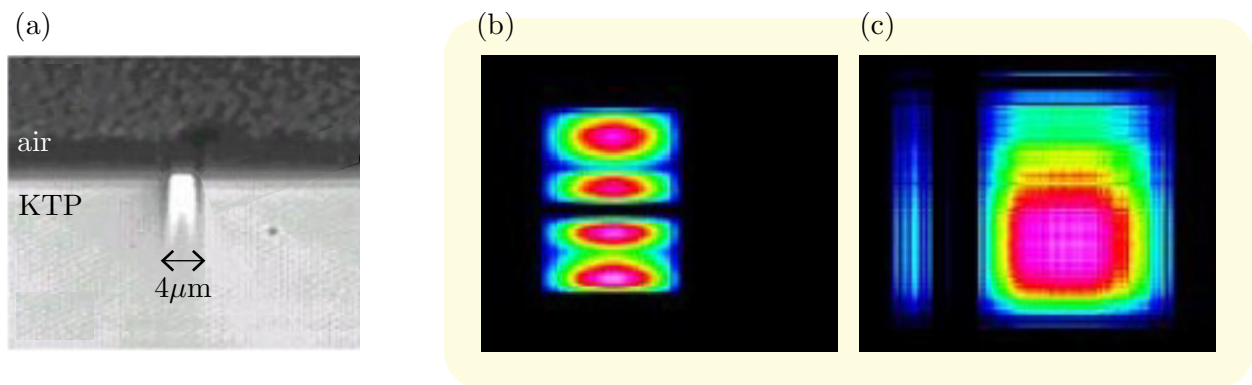
Figure 3.2: Supported Pump Spatial Modes in Waveguide: (a) the waveguide is a 4 μm-wide channel in the surface of the KTP substrate. Three of the four sides of the waveguide share an interface with the KTP crystal and the fourth side shares an interface with air. The waveguide channel must be wide and deep enough to support the fundamental mode of the longest wavelength (1550 nm), allowing for the existence of multiple pump modes. (b) Higher-order pump modes within the waveguide imaged on a Thorlabs beam profiler. (c) The fundamental pump mode (or some combination of the fundamental and higher-order modes).

The aforementioned photon pair source is a 4-μm-deep channel waveguide in a ppKTP crystal designed and fabricated by AdvR. Using standard photolithography techniques, a channel waveguide photomask is patterned onto the KTP wafer from which the crystals are cut. Once cut and polished, the individual waveguide chip is immersed in a molten bath RbNO$_3$ and the Rb$^+$ ions diffuse a few microns deep into the openings in the photomask. The areas where the ions diffused now have a slightly increased index of refraction ($\Delta n \approx 0.01$), thereby creating an optical waveguide in the KTP chip. In order to meet the phase-matching

29

requirements in addition to the wavelength requirements for the application, Type-II phase-matching is used, approximating the following polarization-entangled state[‡]:

$$|\psi\rangle = |H_{810}V_{1550}\rangle + |V_{810}H_{1550}\rangle. \tag{3.1}$$

As a consequence of being guided through the waveguide, the daughter photons exit the crystal collinearly and must be separated by wavelength using a DM. Due to the high confinement of the pump photon within the waveguide channel, a stronger pump electric field is produced, and therefore the source is inherently brighter for the same pump power. Furthermore, the significant length of the waveguide (1.6 cm) provides a long interaction length that is advantageous over bulk SPDC crystals (recall the probability of pair creation varies as L^2). To create the two independent processes needed for entanglement, the crystal is split into two poling periods, and therefore two separate phase-matching conditions must be met. A poling period of $\Lambda_1 = 27$ μm in the first half of the crystal produces the first term, $|H_{810}V_{1550}\rangle$, and a poling period of $\Lambda_2 = 58$ μm in the second half produces the second term, $|V_{810}H_{1550}\rangle$ (shown in Figure 3.1). One could in principle achieve the same effect with two separate crystals, but using a single one removes the challenging (and inefficient) task of coupling photons from one crystal to the next.

3.1.1 Experimental Setup

To characterize this waveguide source, a continuous-wave (CW) 532-nm diode-pumped solid-state (DPSS) laser from Thorlabs (DJ532-40) uses an 808-nm diode laser to pump a Nd:YAG laser at 1064 nm, which is then frequency doubled at 532 nm. The resulting diverging 532-nm beam is collimated to an approximate diameter of 1 mm using an N-BK7 Plano-Convex Lens (f= 100 mm) and travels through a half (Thorlabs - WPH05M-532) and quarter (Thorlabs - WPQ05M-532) waveplate which rotate the laser's output polarization state to horizontal (H) polarization before transmitting through a PBS (Thorlabs - PBS121). After the PBS, the laser has a definite horizontal polarization. The laser is then coupled into a Corning

---

[‡]We will see below that accounting for the spectral-temporal part of the wavefunction makes this an inadequate description, unless appropriate temporal compensation methods are employed.
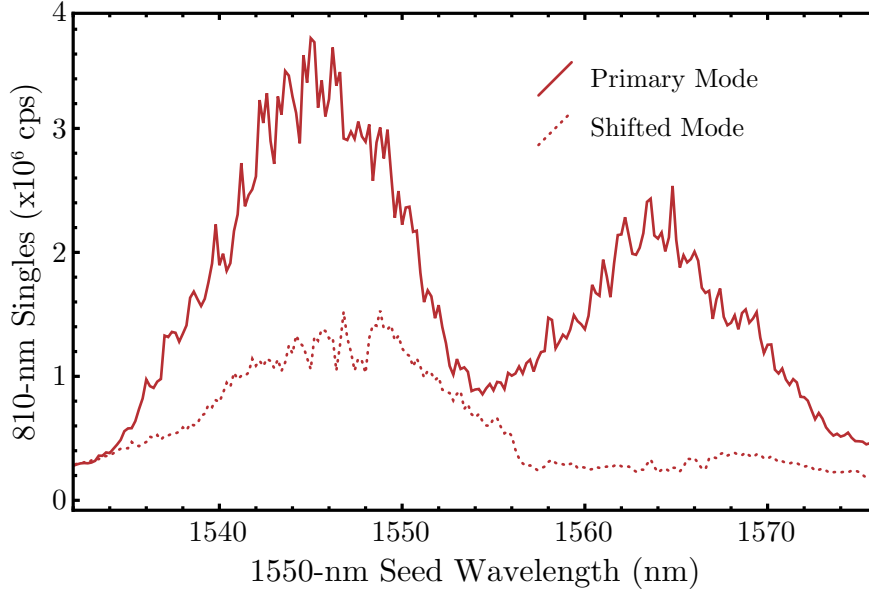
Figure 3.3: Pump Coupling Versus the Downconversion Spectrum: a slight change in the input coupling of the pump can change the downconversion spectrum. The red solid line shows the primary mode, i.e., the mode that is the result of a typical coupling optimization. The red dotted line shows the mode if the input coupling is slightly shifted. For more information on how these plots are made, see Section 3.2.3.

PM480 single-mode fiber that is fiber-pigtailed (glued) to the input of the waveguide. This fiber-pigtailing of the input allows for stabilization of the pump mode through the waveguide channel, and ideally would only pump the fundamental mode of the waveguide. Since the waveguide has to be wide enough to support the zeroth mode of the longest SPDC wavelength (1550 nm), the 532-nm pump beam is consequently multi-mode in the waveguide. The multi-mode nature of the pump beam within the waveguide, shown in Figure 3.2, allows for modal drifting between measurements, which affects the downconversion spectrum and causes unreliable results, as shown in Figure 3.3. To fix this, a fiber pigtail guarantees that the pump always couples into the same mode. Since the light goes through a fiber before the waveguide, but after its polarization is set, a half (Thorlabs - WPH05M-532) and quarter (Thorlabs - WPQ05M-532) waveplate are placed before the fiber in order to pre-compensate for any unitary polarization rotation in fiber. To calibrate these waveplates, a PBS is temporally placed after the waveguide and the waveplated are rotated to maximize power through the PBS; this ensures that the light exiting (and presumably entering) the waveguide is the desired horizontal polarization. Nevertheless, given that the channel is created in the surface of the crystal, the top of the channel has a much higher difference in
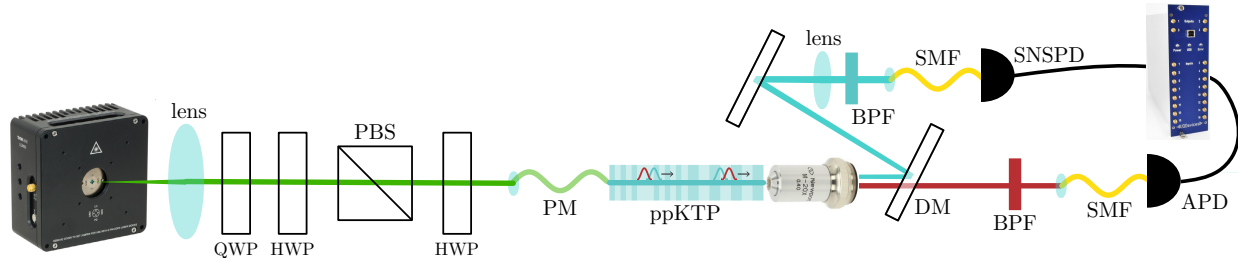
Figure 3.4: Experimental Setup for AdvR Nondegenerate Waveguide Source: a DPSS 532-nm laser is collimated using an aspheric lens and polarized using the PBS. Its transmission through the PBS is maximized using a half waveplate (HWP) and a quarter waveplate (QWP). After the PBS, an additional HWP aligns the pump polarization with the eigenmodes of the polarization-maintaining (PM) fiber. The laser is then coupled into the PM fiber pigtailed to the ppKTP waveguide input. SPDC occurs within the ppKTP crystal and the downconversion photons are coupled out of the waveguide using a microscope objective. A DM separates the downconversion photons by wavelength. The signal (red) beam (810 nm) is collimated using the microscope objective, transmits through the DM and then is coupled into a single-mode fiber (SMF) and detected by a silicon avalanche photodiode (APD). The idler (blue) beam (1550 nm) reflects off the DM, is collimated by an additional lens and then is coupled into a SMF and detected by superconducting nanowire detectors (SNSPDs). The detected photons are then counted in coincidence and processed using a UQDevices timetagger.

index of refraction between the waveguide itself and the surrounding medium (air) than for the other 'sides' of the waveguide (which each see bulk KTP), which causes uneven modal containment within the waveguide channel. From this, we expect a fundamental mode of the waveguide that does not have circular symmetry as a gaussian mode. This uneven mode makes perfectly matching the gaussian mode of the pump beam to that of the waveguide impossible, creating inherent coupling loss for this source.

To couple the downconversion photons out of the waveguide channel, a 20x microscope objective (Newport - M-20x) with effective focal length of 9.0 mm and 0.4 numerical aperture (NA) is placed at the crystal exit. The microscope objective is positioned a distance away from the crystal exit facet required to collimate the 810-nm photon beam. Due to the wavelength dependence of the objective focal length, a secondary lens is needed in the beam path of the 1550-nm photons (more on this later). Immediately after the microscope objective, a DM (thorlabs - DMSP950) separates the downconversion beams by wavelength, transmitting the 810-nm and 532-nm light through the DM and the reflecting the 1550-nm light. After the DM, the two beam paths are treated independently. All filtering, temporal compensation, and polarization measurements (discussed throughout this chapter) on one qubit are done separately from actions on the other qubit. Finally, the photons are coupled

into their respective fibers and detected in coincidence on separate detectors (See Figure 3.4). For 810 nm, a Silicon Avalanche Photodiode (Si-APD, Excelitas - SPCM-AQRH-13-FC) with a detection efficiency $> 60\%$ is used; for 1550 nm, Superconducting Nanowire Single Photon Detectors (SNSPDs) with cryogenic cooling and detection efficiencies of 90% are used. The output signal from the detectors is then processed on a UQDevices (UQD) Logic16 time-tagger (156-ps resolution; count rate of up to 190 MHz). The time-tagger signal is then analyzed on a computer using Mathworks MATLAB.

Ideally, both collection fibers would be single-mode fibers at the corresponding wavelength. Given the 1550-nm light is single mode within the waveguide, the 1550 idler photons can only be born into the fundamental mode of the waveguide; however, since the 810-nm light is multi-mode within the waveguide, the 810 signal photons can be born into multiple modes. This being said, using a single-mode fiber to collect the 810-nm photons could result in loss of the mode that would result in highest entanglement quality. As such, for characterization purposes, we temporarily use a multi-mode fiber in an effort to measure the entanglement quality over all collected modes.

3.2 Polarization Entanglement from a Waveguide

So, how do two photons become entangled in polarization just by having two photon pair sources within the same crystal? As was discussed earlier, the photon pairs made via two processes in the crystal are entangled if their joint state is not separable and the processes are indistinguishable. We have already met the former requirement by using Type-II phase-matching to create the general state, $|\psi\rangle = \alpha|H_{810}V_{1550}\rangle + e^{i\theta}\beta|V_{810}H_{1550}\rangle$. To satisfy the latter, metrics such as the spectral overlap of the downconversion processes and the temporal separation of the photons in the different terms must be optimized. A more correct description of the state coming from the waveguide would be: $|\psi\rangle = |H_{810}\rangle|t_{810,H}\rangle|V_{1550}\rangle|t_{1550,V}\rangle + |V_{810}\rangle|t_{810,V}\rangle|H_{1550}\rangle|t_{1550,H}\rangle$, where the new kets ($|t\rangle$) account for the various exit times of the different photon possibilities. Only if these terms can be made to factorize, i.e., $(|t_{810,H}\rangle|t_{1550,V}\rangle \approx |t_{810,V}\rangle|t_{1550,H}\rangle)$, can we obtain the simple maximally polarization-entangled state in Equation 3.1. Otherwise, tracing over the timing kets
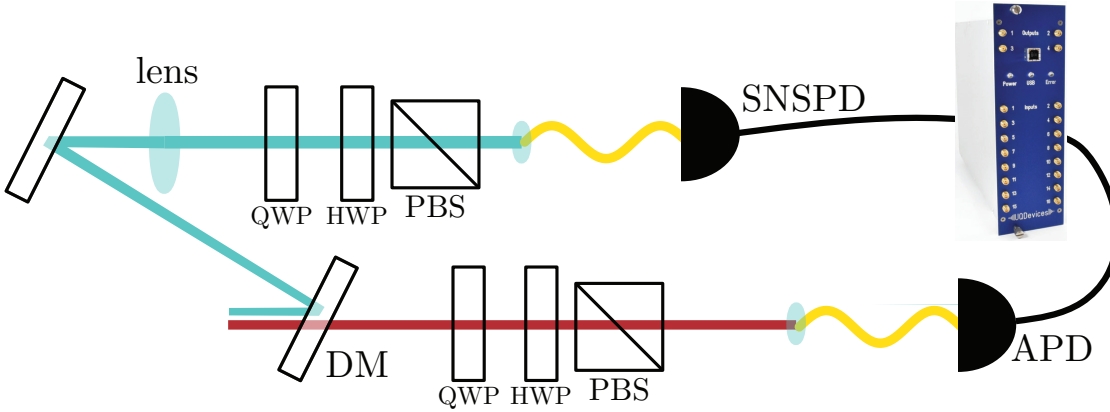
Figure 3.5: Experimental Setup of a State Tomography: a QWP, HWP, and PBS are placed in the paths of both photons after the DM in order to independently project the downconversion photons onto all six basis polarizations. The downconversion photons are then counted in coincidence and their coincidence rate is recorded for every two-qubit polarization combination.

will leave the polarization part of the wavefunction in a partially to fully mixed state, which can only be represented by a density matrix. In this section, we present general techniques for measuring and correcting the polarization entanglement of the downconversion photons, and discuss our waveguide source results.

3.2.1   Quantum State Tomography

To quantify the quality of entanglement from our source, we perform a two-qubit quantum state tomography on the downconversion state. To do so, a half-wave plate (HWP), quarter-wave plate (QWP), and PBS are put in both beam paths after the DM, as shown in Figure 3.5. Using these polarization optics, coincidences from all 36 two-qubit polarization combinations (6 polarizations from each path - H, V, D, A, R, L) are measured and a maximum likelihood estimate gives us the most probable density matrix ρ that could have produced the observed measurement results [37]. From this density matrix, many useful metrics can be calculated, such as the concurrence (a measure of the entanglement), the purity (how pure the two-photon polarization state is), and the fidelity (how well the measured state matches the desired theoretical state).

All polarization states live somewhere in/on the Poincaré sphere (the polarization-specific Bloch sphere); pure states live on the surface, whereas mixed states live inside, as shown in

Figure 3.6. Given the three-dimensional geometry of a sphere, in order to locate a state, measurements in three bases ($\{H, V\}$, $\{D, A\}$, and $\{R, L\}$) are made; Figure 3.7 gives a visual representation of a single-qubit state tomography on the Poincaré sphere, which is the polarization-specific Bloch sphere. The first measurement tells us, for example, on what slice of the sphere the state lives; it turns the three-dimensional shape into two dimensions. The second measurement tells us on what stripe across the slice that state lives, leaving us with a one-dimensional piece of the Poincaré sphere. Finally, the third measurement fully locates the state to a point on the sphere. In practice, the measurements will have at least statistical uncertainty, and possibly other uncertainty as well, e.g., arising from pump laser power drift. Therefore, as indicated in Figure 3.7, subsequent measurements only collapse the state to a region. Experimentally, we can accomplish this same locating scheme by independently projecting each qubit onto one of its 6 basis polarizations and measuring the corresponding coincidences.

By expanding on the one-photon case, to determine the 2-photon polarization state produced from the downconversion source, $6 \times 6 = 36$ measurements are made. Once all necessary measurements are made, the data can be processed using the Kwiat Group's Tomography Interface [38], which uses maximum likelihood estimation to calculate the density matrix that best could have produced the measured data. From the density matrix, the concurrence, purity, and fidelity can be calculated, giving concise metrics of how entangled the state is (the density matrix is the "complete picture," since everything else is derived from it).

The ideal density matrix[§] that corresponds to the $|\psi^+\rangle$ maximally entangled state is shown in Figure 3.8(a-c): (a) and (b) show the real and imaginary parts (none for $|\psi^+\rangle$), while (c) shows the absolute value $|\rho|$[¶]. The corresponding plots for the measured density matrix for our waveguide-based source of polarization entanglement are shown in Figure 3.8(d-f). The terms on the diagonal of the matrix ($|V_{810}V_{1550}\rangle\langle V_{810}V_{1550}|$, $|V_{810}H_{1550}\rangle\langle V_{810}H_{1550}|$, $|H_{810}V_{1550}\rangle\langle H_{810}V_{1550}|$, $|H_{810}H_{1550}\rangle\langle H_{810}H_{1550}|$) represent the relative amplitudes of the two-

---

[§]Note that there is no simple graphical representation like the Bloch/Poincaré sphere for these multi-qubit states.

[¶]The absolute value of ρ is a convenient visualization tool, since it shows what the real part of ρ would look like if all the phases on the off-diagonal terms were correctly set to zero.
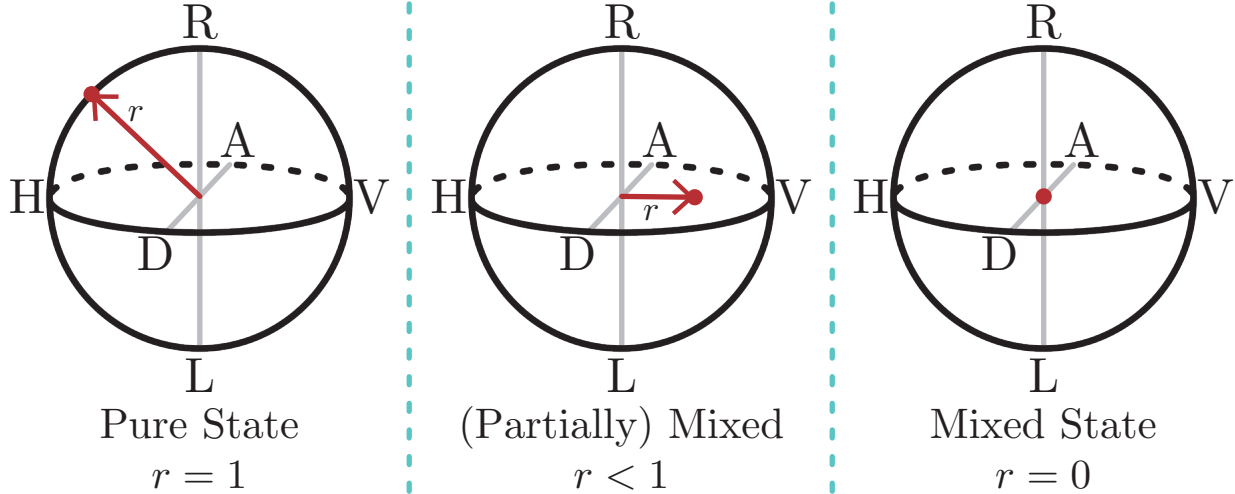
Figure 3.6: Single Qubit States on the Poincaré Sphere: the single-qubit polarization state can be represented using 3D vectors on the Poincaré sphere, which has a radius $r = 1$. A pure state will always live somewhere on the surface of the sphere, i.e., $r = 1$. A partially mixed state will live somewhere inside the sphere, i.e., $0 < r < 1$. A completely mixed state will live at the center of the sphere with radius $r = 0$.
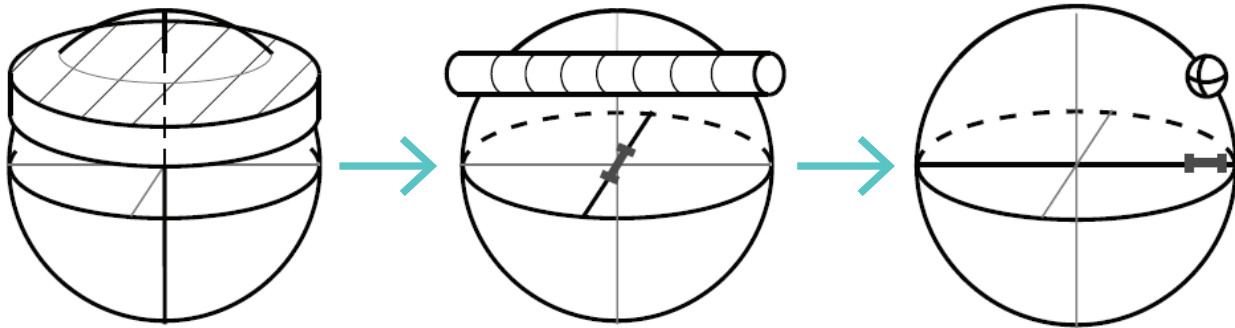
Figure 3.7: Poincaré Sphere Representation of State Tomography: by measuring the polarization state in three bases, the complete quantum state can be reconstructed and located on the Poincaré sphere.

qubit processes independently. The off-diagonal elements show the coherence between the two independent processes related to their entanglement. From the density matrix of the entangled state, three important metrics are calculated: concurrence (C), state purity (γ), and fidelity (F).

Concurrence and state purity are related, but an entangled state is inherently pure, while, a pure state is not necessarily entangled (consider the state $|HV\rangle$). Therefore, it is necessary to determine both metrics. A quantum state that is pure can be represented as a single vector in its Hilbert space, $\rho_{\text{pure}} = |\psi\rangle\langle\psi|$. A mixed state, on the other hand, is represented by a linear combination of pure states, $\rho_{\text{mixed}} = \sum p_i |\psi_i\rangle\langle\psi_i|$. Mathematically,
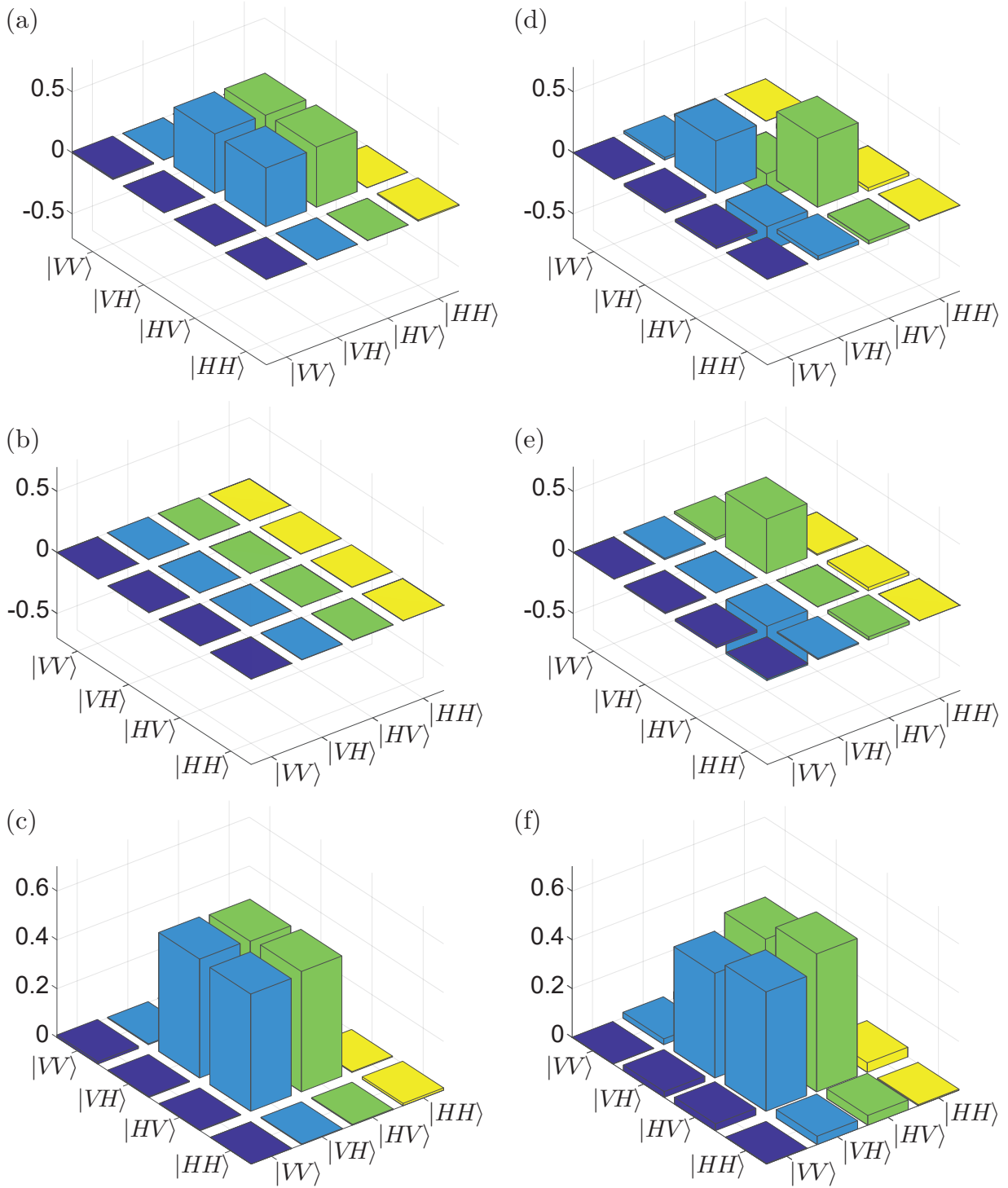
Figure 3.8: Theoretical and Measured Density Matrices: graphical representations of the (a) real, (b) imaginary, and (c) absolute value density matrix of the maximally entangled state, $|\psi^+\rangle$ and the (d) real, (e) imaginary, and (f) absolute value density matrix of the measured two-qubit quantum state. The axes are labeled with the first qubit corresponding to the signal (810 nm) photon and the second qubit corresponding to the idler (1550 nm) photon. The measured density matrix features our best results to date: an accidental-corrected state fidelity of $F = 0.986$, concurrence of $C = 0.983 \pm 0.004$, and purity of $\gamma = 0.990 \pm 0.005$.

the purity can be calculated from the density matrix as

$$\gamma \equiv tr(\rho^2), \tag{3.2}$$

with a lower limit of $1/d$, where d is the dimension of the Hilbert space, and an upper limit of 1. As an example, consider the following theoretical, ρ_{th}, and measured, ρ_e, density matrices:

$$\rho_{th} = \begin{pmatrix} 0 & 0 & 0 & 0 \\ 0 & 0.5 & 0.5 & 0 \\ 0 & 0.5 & 0.5 & 0 \\ 0 & 0 & 0 & 0 \end{pmatrix} \quad \text{and} \quad \rho_e = \begin{pmatrix} 0.01 & 0.01 & 0.01 & 0 \\ 0.01 & 0.61 & 0.32 & 0.02 \\ 0.01 & 0.32 & 0.38 & 0.02 \\ 0 & 0.02 & 0.02 & 0 \end{pmatrix}. \tag{3.3}$$

Here, $\gamma_e = tr(\rho_e^2) = 0.72$, compared with a lower limit of $1/(d = 4) = 0.25$. Another way of characterizing the purity is the entropy; since entropy is a measure of the disorder of a system, it makes sense that a pure state would have an entropy of zero. The Von Neumann entropy of a state is given by $S = -Tr(\rho \log \rho)$. Sometimes it is more convenient to consider the linearized form, the "linear entropy" S_L, defined as $S_L \equiv 1 - Tr\rho^2$. Therefore, one can relate the purity of the quantum state with its linear entropy as, $\gamma = 1 - S_L$.

The entanglement $E(\rho)$ of the state is related to the concurrence as

$$E(\rho) \equiv h\left(\frac{1 + \sqrt{1 - C^2}}{2}\right), \tag{3.4}$$

where $h(x) \equiv -x \log_2 x - (1 - x) \log_2(1 - x)$ [39]. Concurrence is considered a metric for entanglement that can be calculated directly from the density matrix, with a lower limit of zero and an upper (optimal) value of one:

$$C(\rho) = \text{Max}\{0, \lambda_1 - \lambda_2 - \lambda_3 - \lambda_4\}, \tag{3.5}$$

where λ_i is defined as the square root of the corresponding eigenvalue of $\rho\tilde{\rho} = \rho\big((\sigma_y \otimes \sigma_y)\rho^*(\sigma_y \otimes \sigma_y)\big)$, and σ_y refers to the corresponding Pauli matrix. If $C = 0$, then $E(\psi) = 0$; if $C = 1$ (maximally entangled), then $E(\psi) = 1$. Now we give an explicit example, using

38

the experimental density matrix. To calculate the concurrence, we begin by determining $\widetilde{\rho} = (\sigma_y \otimes \sigma_y)\rho_e^*(\sigma_y \otimes \sigma_y)$, which is the spin-flipped density matrix of ρ_e, and multiplying it by ρ_e:

$$\rho_e\widetilde{\rho} = \begin{pmatrix} 0.01 & 0.01 & 0.01 & 0 \\ 0.01 & 0.61 & 0.32 & 0.02 \\ 0.01 & 0.32 & 0.38 & 0.02 \\ 0 & 0.02 & 0.02 & 0 \end{pmatrix} \begin{pmatrix} 0 & 0 & 0 & -1 \\ 0 & 0 & 1 & 0 \\ 0 & 1 & 0 & 0 \\ -1 & 0 & 0 & 0 \end{pmatrix} \begin{pmatrix} 0.01 & 0.01 & 0.01 & 0 \\ 0.01 & 0.61 & 0.32 & 0.02 \\ 0.01 & 0.32 & 0.38 & 0.02 \\ 0 & 0.02 & 0.02 & 0 \end{pmatrix} \begin{pmatrix} 0 & 0 & 0 & -1 \\ 0 & 0 & 1 & 0 \\ 0 & 1 & 0 & 0 \\ -1 & 0 & 0 & 0 \end{pmatrix}$$

$$= \begin{pmatrix} 0 & -0.02 & -0.02 & 0 \\ -0.02 & 0.38 & 0.32 & -0.01 \\ -0.02 & 0.32 & 0.61 & -0.01 \\ 0 & -0.01 & -0.01 & 0.01 \end{pmatrix}$$

(3.6)

From here, we calculate the eigenvalues of the resulting matrix from Equation 3.6 and take their square root: $\lambda_1 = 0.80$, $\lambda_2 = 0.16$, and $\lambda_3 = \lambda_4 = 0$. Therefore, $\lambda_1 - \lambda_2 - \lambda_3 - \lambda_4 = 0.64$. Since this number is greater than zero, we find $C = 0.64$, which corresponds to an entanglement value of $E(C) = 0.50$. So, our example quantum state is considered partially entangled (In the following sections we discuss how to improve the entanglement of that state).

The final metric calculated from the density matrix is the state fidelity, which is a measure of how closely the measured density matrix matches the theoretical one for the desired state, and ranges from 0 to 1. Mathematically, the fidelity is defined as the overlap of the measured and theoretical density matrices [40]:

$$F(\rho, \sigma) \equiv |\langle\psi_\rho|\psi_\sigma\rangle|^2 = \left(tr\sqrt{\sqrt{\rho}\sigma\sqrt{\rho}}\right)^2 = F(\sigma, \rho). \tag{3.7}$$

For our example state, its fidelity to the theoretical state is 0.81.

This example quantum state represents the absolute value[‖] of a measured state from our

---

[‖]The reason we consider the absolute value of the density matrix is because it is experimentally trivial to go from the actual value to the absolute value; a liquid crystal phase retarder or a simple tilting of a birefringent waveplate can correct any phase between the two terms of the quantum state.
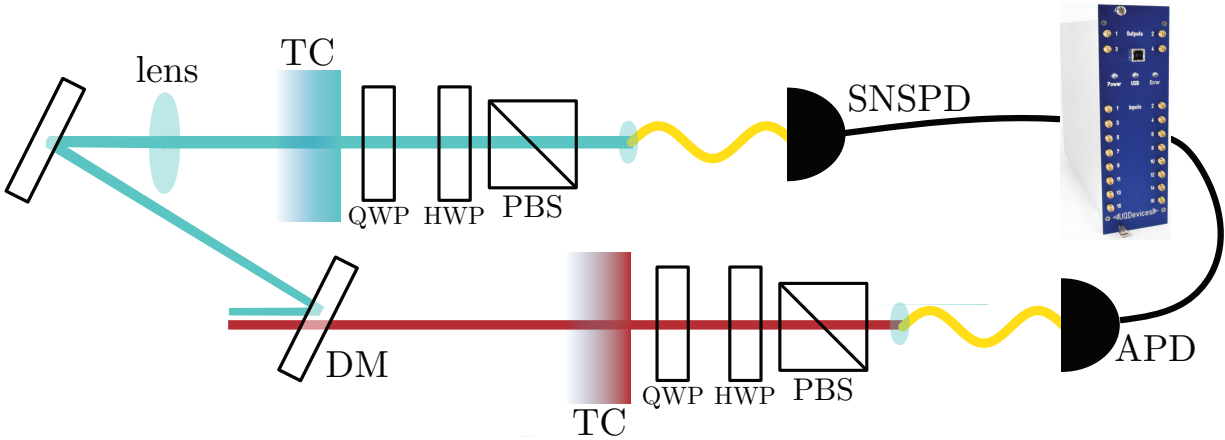
Figure 3.9: Temporal Compensation Experimental Setup: in order to temporally compensate our entanglement source, we add additional birefringent temporal compensation (TC) crystals with a width set to recombine the wave packets of the different polarization components for each downconversion wavelength. The gradient represents the same-color downconversion photons becoming re-overlapped as they travel through the TC crystal.

waveguide-based entanglement source. The state purity, concurrence, and fidelity are insufficiently high for our desired application; typically, a usable source for a quantum communication application like quantum key distribution would feature metrics exceeding, e.g., 0.97. To optimize these values, various adjustments can be made in order to increase the indistinguishability of the contributing processes, including compensating for any group-velocity walk-off within the crystal (temporal compensation) and matching the spectral properties of the processes. The following sections will highlight the effect of temporal and spectral optimization on our measured entanglement state.

3.2.2 Temporal Compensation

As discussed in Section 2.4, the group velocity of wavepackets** within a nonlinear crystal is both wavelength- and polarization-dependent. Given that the waveguide-based source includes combinations of three different wavelengths and two different polarizations, calculating the relative times at which the photons exit the crystal is non-trivial. To begin, the group velocities are determined for the pump and the four downconversion wavepackets in-

---

**For discussion of temporal compensation, it is helpful to model photons as discrete wave packets of light, so we will temporarily switch terminology in this section, i.e., it does not matter that those wavepackets could be produced at any time by the (continuous) pump.

dependently. From Equation 2.27 and the indices of refraction given in Figure 2.4, the group velocities in waveguide ppKTP are estimated to be:

$$v_g(H_{532}) = 1.54 \times 10^8 \, \mathrm{m/s}$$
$$v_g(V_{810}) = 1.55 \times 10^8 \, \mathrm{m/s}$$
$$v_g(H_{1550}) = 1.68 \times 10^8 \, \mathrm{m/s}$$
$$v_g(H_{810}) = 1.64 \times 10^8 \, \mathrm{m/s}$$
$$v_g(V_{1550}) = 1.61 \times 10^8 \, \mathrm{m/s}. \tag{3.8}$$

Next, the lengths through which each wavepacket travels is determined. The photons for the first process $V_{810}H_{1550}$ will be (on average[††]) created in the middle of the first half of the crystal and then travel through the remaining 3/4 of the length of the crystal[‡‡]. Using the lengths described in Figure 3.10, the time it takes for a downconversion photon created in the first half to exit the crystal is equal to the time it takes for the pump photon (H_{532}) to travel through l_1 plus the time it takes for the downconversion photon to travel through the remaining crystal length l_2. This time is different for each photon in the pair since they have differing wavelengths and polarizations. Similarily, the photons for the second process will be created in the center of the second half of the crystal and then travel the remaining 1/4 of the length of the crystal. Therefore, the total time for each photon born in the second half of the crystal will be the time it takes for the pump photon to travel through l_3 plus the time it takes for the downconversion photons from the second process to travel through l_4. For example, the exit time for the H_{1550} photon is $t_{H_{1550}} = l_1/v_g(H_{532}) + l_2/v_g(H_{1550})$, whereas the exit time for V_{1550} is $t_{V_{1550}} = l_3/v_g(H_{532}) + l_4/v_g(V_{1550})$. Given that the waveguide source has a poling configuration that creates $V_{810}H_{1550}$ in the first half of the crystal and $H_{810}V_{1550}$ in the second half, the exit times for $V_{810}, H_{1550}, H_{810}$, and V_{1550} are 103.21 ps, 97.31 ps,

---

[††]As discussed in Section 2.4, the photon pairs are born throughout the entire length of the crystal; however it is convenient and mathematically appropriate to approximate all of them being born in the center.

[‡‡]Note: the index of refraction is not affected by the poling process, so Equation 2.27 applies to both halves of our dual-poled crystal.
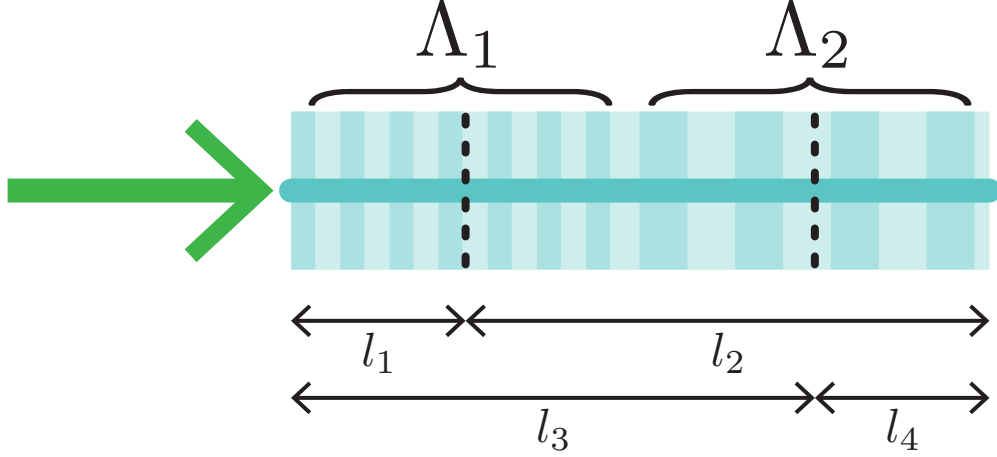
Figure 3.10: Propagation Lengths for Temporal Compensation in Consecutively Poled Waveguide: shown are the lengths used to calculate the temporal compensation for the consecutively poled waveguide-based source. The pump travels a distance $l_1(l_3)$ before downconverting into the $V_{810}H_{1550}$ $(H_{810}V_{1550})$ processes. The $V_{810}H_{1550}$ $(H_{810}V_{1550})$ processes then travel a distance of l_2 (l_4).

102.10 ps, and 102.59 ps, respectively. These numbers mean that the H_{1550} photon leaves the crystal $102.59 - 97.31 = 5.28$ ps earlier than the V_{1550} photon, but the H_{810} photon leaves only $103.21 - 102.10 = 1.11$ ps ahead of the V_{810} photon. Note that we only care about the relative times of the different polarizations for each wavelength independently; it is irrelevant if the different colors exit at different times, i.e., if their wavepackets do not overlap, since they will be separated and detected individually anyway. One question immediately arises: Are these time offsets "large" or "small"? The answer of course depends on the effective width of the photon wavepackets given by $\tau_c = \lambda^2/c\Delta\lambda$, where $\Delta\lambda$ is the FWHM bandwidth of the photon in question[§§]. For example, the narrowest bandwidth filter used has a bandwidth of $\Delta\lambda_{1550} = 1.4$ nm, corresponding to a $\tau_c = 5.72$ ps. Therefore, compensation will require slowing down the horizontally polarized photons with respect to the vertically polarized photons. It is important to note here that the photons created in the first half of the crystal still experience walk-off as they travel through the second half of the crystal.

A simulation of how the wavepackets travel through the crystal is shown in Figure 3.11, where the three time periods, t_1, t_2, t_3, represent the time before the pump photon reaches

---

[§§]More precisely, it is the bandwidth of the detected photon. Therefore, one can in principle reduce the need for temporal compensation by using narrowband spectral filters before the detectors. However, this comes at the cost of reducing the source effective brightness.
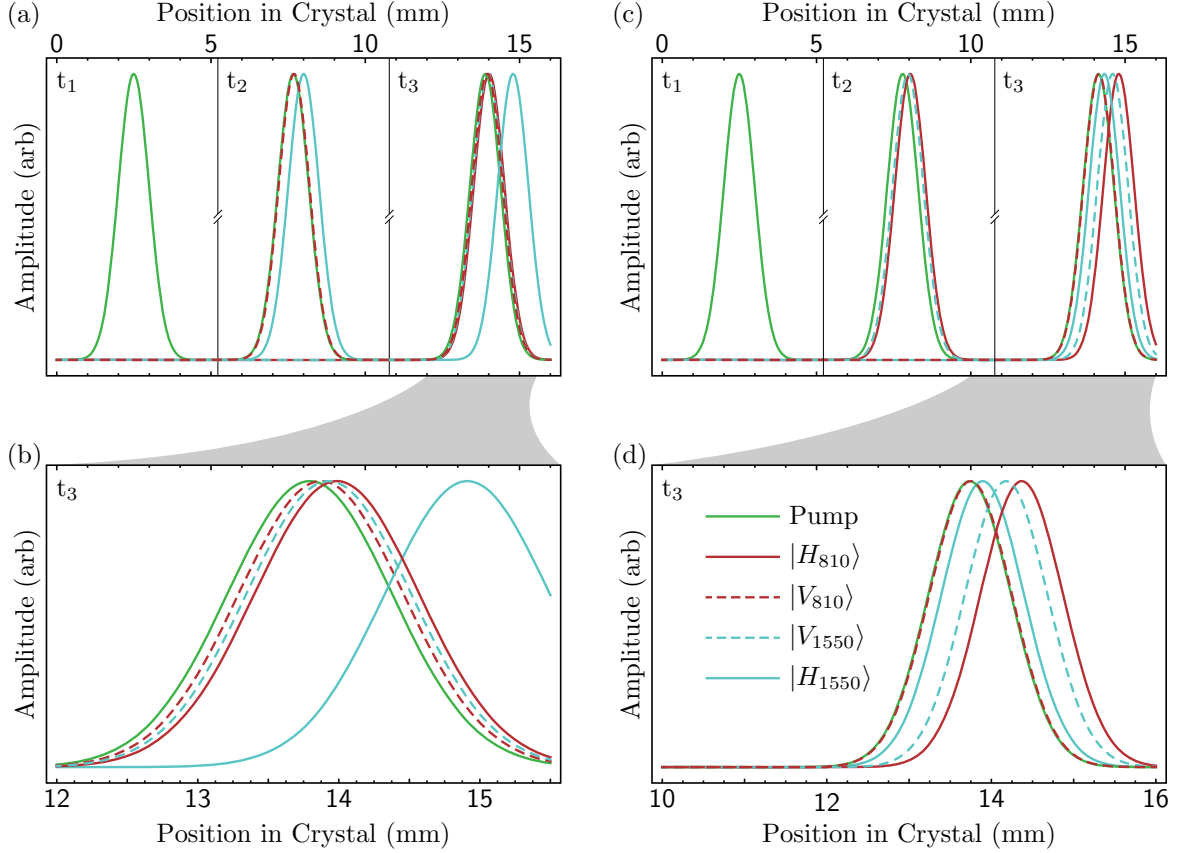
Figure 3.11: Waveguide Temporal Compensation Simulation: (a) represents a crystal geometry, where $|V_{810}H_{1550}\rangle$ ($|H_{810}V_{1550}\rangle$) is created in the first (second) half of the crystal. (b) is a zoomed look at t_3 of (a). (c) represents a crystal geometry where $|H_{810}V_{1550}\rangle$($|V_{810}H_{1550}\rangle$) is created in the first (second) half of the crystal. (d) is a zoomed look at t_3 of (c).

the center of the first section of poling, the time between the centers of the first and second sections, and the time after the center of the second section of poling, respectively. The simulation also gives two different poling orientations: one where the process $|H_{810}V_{1550}\rangle$($|V_{810}H_{1550}\rangle$) is created in the first(second) half of the crystal, and vice versa (i.e., pumping the crystal in the other direction). This simulation gives a visible expectation for the temporal order in which the photons should theoretically leave the crystal. The orientation for the current waveguide poling periods is shown in Figures 3.11(a) and (b) where $V_{810}H_{1550}$ ($H_{810}V_{1550}$) is created in the first (second) half of the crystal. Figures 3.11(c) and (d) show the photon exit times if the order of the poling period was reversed.

To compensate for the group velocity walk-off within the crystal, thereby erasing any temporal distinguishing information, the calculated exit times are converted into a length
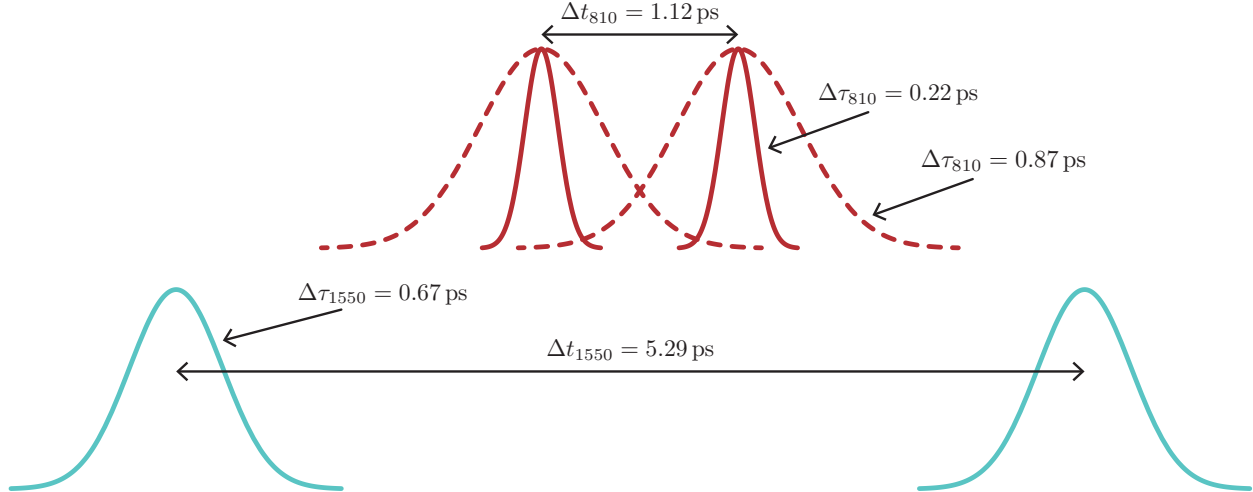
Figure 3.12: Downconversion Wavepackets with Coherence Time and Group Velocity Walkoff: the coherence time τ (width) of the wavepacket is determined by the filters used in each wavelength path; a narrower filter bandwidth corresponds to a longer coherence time. The group velocity walkoff Δt from the ppKTP crystal gives the separation of the centers of the wavepackets. In order for there to be any entanglement between the two processes, the wavepackets must have some overlap. Here, the dashed red wavepackets would seemingly result in some small amount of entanglement. However, entanglement will only be possible if there is simultaneous overlap for both wavelengths. For those wavepackets that do not overlap (the red solid and blue solid), an additional birefringent crystal after the source is required to overlap the wavepackets.

of birefringent crystal, e.g., calcite, through which the downconversion photons then travel after the DM as shown in Figure 3.9. The important metric is the relative exit time between the two downconversion photons of the same wavelength (one from each pair). For example, the time used for calculating the necessary length of calcite to temporally combine the 810-nm photons is $\Delta t_{810} = |t_{V_{810}} - t_{H_{810}}| = 1.11$ ps, and $\Delta t_{1550} = |t_{V_{1550}} - t_{H_{1550}}| = 5.28$ ps for the 1550-nm photons. To convert the exit times into birefringent element width, one can typically obtain the Sellmeier equation from the crystal manufacturer's website and use it to determine the index of refraction for the wavelength and polarization of the downconversion photons. Once the indices of refraction are known, the width can be determined using the methods described in Section 2.4. For example, the Sellmeier equations for calcite taken from the Newlight Photonics Inc website is: $n_o^2 = 2.69705 + 0.0192064/(\lambda^2 - 0.01820) - 0.0151624\lambda^2$ and $n_e^2 = 2.18438 + 0.0087309/(\lambda^2 - 0.01018) - 0.0024411\lambda^2$. Therefore, we calculate that we need samples of length 9.71 mm and 2.08 mm, respectively, for the 1550- and 810-nm photons.

Up until now, the discussion of group velocity walk-off and temporal compensation in-

cluded wavepackets described only by their average location in time. This simplification is helpful in estimating the amount of birefringent material required for perfect compensation; however, it ignores the fact that these wavepackets have some width in the form of their coherence time, $\Delta\tau = \lambda^2/c\Delta\lambda$, where $\Delta\lambda$ can be determined by the bandwidth of the narrowband filters used in the individual paths of the downconversion photons[¶¶], and λ is the vacuum wavelength. If the wavepackets' widths are larger than the temporal separation of their centers, they will partially overlap, and therefore the polarization part of the quantum state will be partially entangled. This partial overlap allows for optimization of the temporal compensation by plotting the concurrence with respect to birefringent crystal thickness. As shown in Figure 3.12, given the poling configuration relevant to Figure 3.11(b), the group velocity walkoff Δt for the 810-nm wavepackets is 1.11 ps and for the 1550-nm wavepackets is 5.28 ps. For the 810-nm side, a 10-nm filter gives a coherence time $\Delta\tau_{810} = 0.22$ ps and a 2.5-nm filter gives a coherence time $\Delta\tau_{810} = 0.87$ ps. For the 1550-nm side, a 12-nm filter gives $\Delta\tau_{1550} = 0.67$ ps. We then see that an alternate solution to fixing the group velocity walkoff would be to use very narrowband filters; however, for example, the 1550-nm side would require a filter with a bandwidth $\Delta\lambda \leq 1.5$ nm, which, as will be shown in Section 3.2.3, would end up throwing away the majority of the downconversion pairs, resulting in overall low detected photon pair rates. Therefore, the preferred method is to add temporal compensation in the downconversion paths in order to improve the entanglement of the state without degrading the overall source efficiency.

To show the effect of temporal compensation on the entanglement of the polarization state, state tomographies are taken for various lengths of the additional birefringent temporal compensation crystal placed in each downconversion path, as shown in Figure 3.13. The concurrence and purity for these measured density matrices are calculated and fit to a parabola, $y = a(x-h)^2+b$, where h is the calcite width that yields the optimal entanglement metrics. Figure 3.14(a) shows the measured concurrence and purity for different calcite widths in the 1550 path; from these two parabolas, we can take the weighted average of

---

[¶¶]Because we count in coincidence, the relevant effective bandwidth of each photon is the product of the width of the actual filter transmission spectrum (e.g., 0.9 between $\lambda_{\mathrm{min,filter}}$ and $\lambda_{\mathrm{max,filter}}$, and zero outside this range) and the inferred spectrum from the conjugate photon's filter, where $\lambda_{s,\mathrm{max}} = (\lambda_p^{-1} - \lambda_i^{\mathrm{min}})^{-1}$ and $\lambda_{i,\mathrm{min}} = (\lambda_p^{-1} - \lambda_s^{\mathrm{max}})^{-1}$.
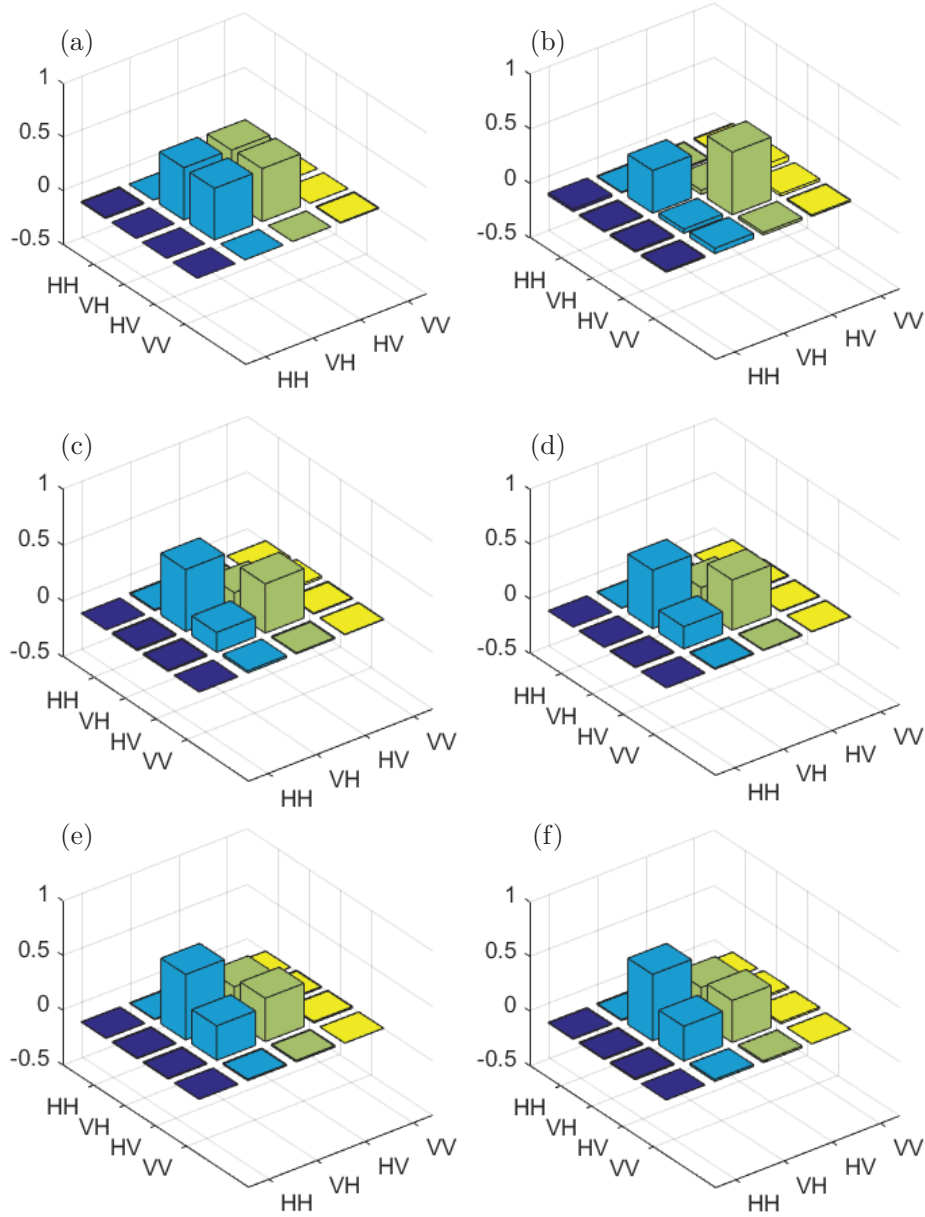
Figure 3.13: The Effect of Temporal Compensation on the Density Matrix of the Entanglement State: results of the two-qubit state tomographies performed on the downconversion photons from the waveguide-based entanglement source with varying amounts of temporal compensation. (a) The ideal density matrix for the maximally entangled state. (b) No temporal compensation: $C = 0.05$; $\gamma = 0.49$. (c) Temporal compensation in the 810-nm path (no compensation in 1550-nm path): $C = 0.35$; $\gamma = 0.56$. (d) Additional temporal compensation in the 810-nm path (no compensation in 1550-nm path): $C = 0.40$; $\gamma = 0.58$. (e) Temporal compensation in the 1550-nm path (in addition to 810-nm compensation from (d)): $C = 0.62$; $\gamma = 0.71$. Additional temporal compensation in the 1550-nm path (in addition to 810-nm compensation from (d)): $C = 0.63$; $\gamma = 0.72$. The total widths of the compensation elements are not specified for these measurements, as a combination of crystals were used, including tunable compensation wedges with lengths that could not be precisely measured. For a more precise measure of the relationship between the polarization entanglement and the amount of temporal compensation, see Figures 3.14 and 3.15.

Figure 3.14: Temporal Compensation Parabola Fit for 1550-nm Calcite: (a) the concurrence and purity versus the calcite thickness added in the 1550-nm beam path. A parabolic fit was used to find the calcite width that yielded the maximum entanglement metrics. (b) The density matrix fringes which represent the probability of getting a click (detecting a photon) when projecting the state onto $\Delta\theta$ (x-axis), which is the polarization angle between the two photons in a pair when $|D\rangle = \frac{1}{\sqrt{2}}(|H\rangle + |V\rangle)$ is projected onto one photon in the pair and an arbitrary linear polarization state is projected onto the other photon using the HWPs in the tomography setup. The equation $P = \langle D\Delta\theta|(|\rho|)|D\Delta\theta\rangle$ demonstrates this projection. For example, when $\Delta\theta = 0$, $P = \langle DD|(\rho)|DD\rangle$. The different curves represent different values of calcite widths.

the peaks and use that to estimate the amount of calcite needed for optimal entanglement. Figure 3.14(b) shows the fringes from which the max visibility is calculated and represents the probability of getting a click (detecting a photon) when projecting the state onto $\Delta\theta$, which is the polarization angle between the two photons in a pair when $|D\rangle = \frac{1}{\sqrt{2}}(|H\rangle + |V\rangle)$ is projected onto one photon in the pair and an arbitrary linear polarization state is projected onto the other photon using the HWPs in the tomography setup. The equation, $P = \langle D\Delta\theta|(|\rho|)|D\Delta\theta\rangle$ demonstrates this projection, where $|\rho|$ is the absolute value of the measured density matrix. We then do the same measurement with calcite in the 810-nm side, as shown in Figure 3.15. From these parabolic fits, we find that the ideal amount of calcite is 7.10±0.02 mm in the 1550 path and 0.43±0.06 mm in the 810-nm path. These numbers are significantly different from the expected values; however, given that the Sellmeier equations are empirical measures of the indices of refraction, some error is expected due to discrepancies between crystal growths and the doping mechanism used in the waveguide process. By tuning the temporal compensation, we achieve a concurrence of $C = 0.871 \pm 0.005$ and purity of $\gamma = 0.877 \pm 0.005$.
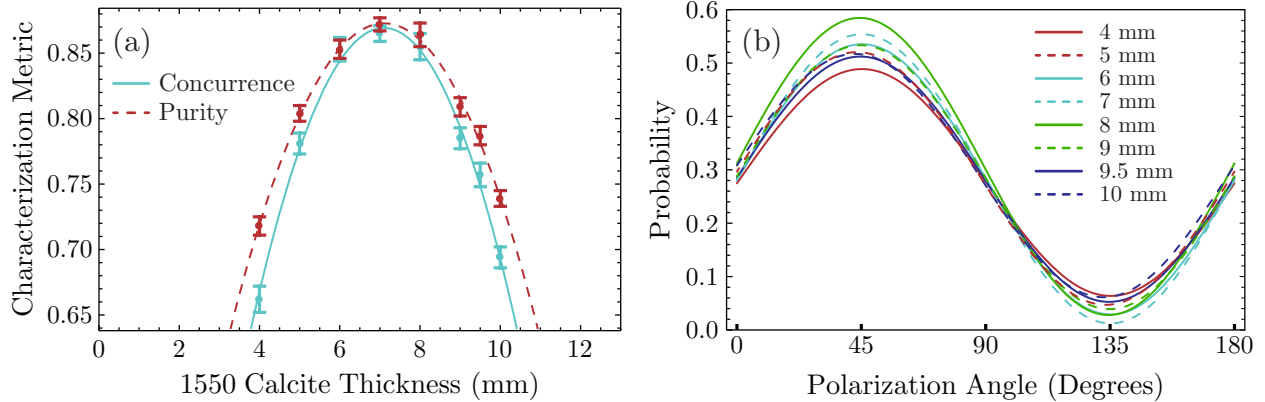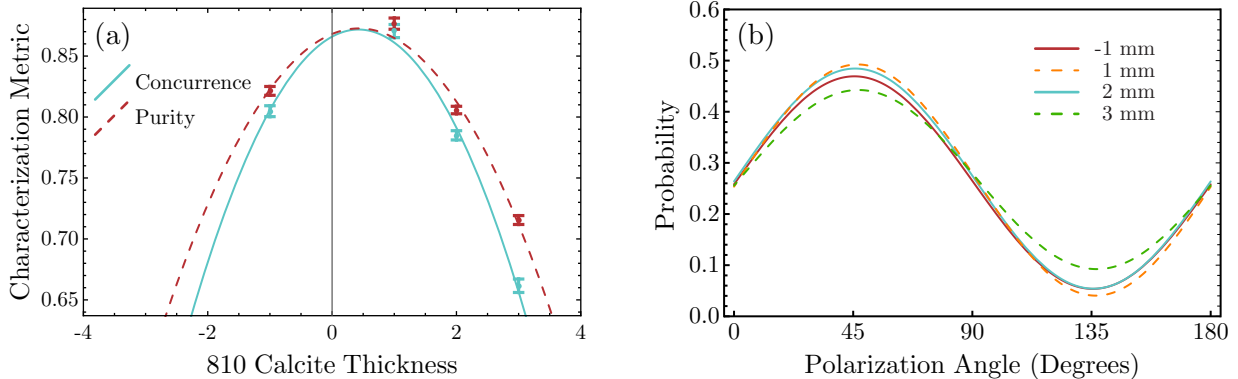
Figure 3.15: Temporal Compensation Parabola Fit for 810-nm Calcite: (a) the concurrence and purity versus the calcite thickness added in the 810-nm beam path with 7 mm of calcite in the 1550-nm arm. A parabolic fit was used to find the calcite width that yielded the maximum entanglement metrics. (b) The density matrix fringes which represent the probability of getting a click (detecting a photon) when projecting the state onto $\Delta\theta$ (x-axis), which is the polarization angle between the two photons in a pair when $|D\rangle = \frac{1}{\sqrt{2}}(|H\rangle + |V\rangle)$ is projected onto one photon in the pair and an arbitrary linear polarization state is projected onto the other photon using the HWPs in the tomography setup. The equation $P = \langle D\Delta\theta|(|\rho|)|D\Delta\theta\rangle$ demonstrates this projection. The different curves represent different values of calcite widths.

3.2.3 Measuring the Parametric Downconversion Spectrum

Even with perfect temporal compensation, if the two processes $|H_{810}V_{1550}\rangle$ and $|V_{810}H_{1550}\rangle$ do not have indistinguishable spectra, the entanglement of the state will be degraded. To measure the spectra of the processes, we can perform one of two measurements: stimulate the downconversion process with a tunable seed laser centered at one of the downconversion wavelengths [41], or use a tunable narrow filter on the downconversion output to directly measure the counts versus the filter central wavelength. The former method uses energy conservation and a tunable seed laser to control the wavelength of the measured downconversion photon. Figure 3.16 shows how this is done experimentally: a tunable seed laser (Agilent) around 1550 nm is coupled via free space into the waveguide*** and the 810-nm "singles" (clicks on a single detector) are recorded. Since we are using type-II phase matching for our source, the seed laser will have a polarization orthogonal to the polarization of the 810-nm collected downconversion photon, e.g., the 1550-nm seed laser is horizontally (vertically) polarized and the 810-nm photons are vertically (horizontally) polarized. By plotting the singles counts versus the seed wavelength, a reconstruction of the spectral shape of the

---

***Note: This method of in-coupling the 1550-nm seed laser only works with a crystal that is not fiber pigtailed; the pigtail-fiber for the 532-nm pump will not propagate the 1550-nm light.
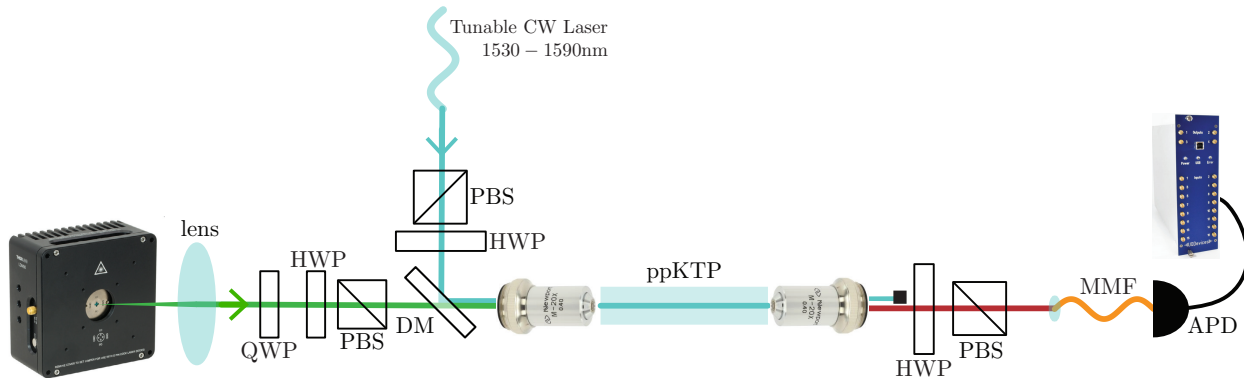
Figure 3.16: Experimental Setup of Stimulated Parametric Downconversion: in addition to the original waveguide setup, a tunable laser is also coupled into the ppKTP waveguide and "seeds" the downconversion process. Due to energy conservation, each seed wavelength will result in a pair being created with one photon having the seed wavelength and the other photon having a wavelength that satifies energy conservation (assuming a particular pump wavelength); the likelihood of such a pair being created is directly proportional to the number of photons in and hence the power of the seed laser, and, more importantly, to the intrinsic probability such a pair would be created via spontaneous downconversion. The non-seed-wavelength photon is then detected and the number of counts versus seed wavelength is recorded. A HWP in the paths of both the seed photon and the collected photon is used to control the spectrum being measured ($H_{810}V_{1550}$ or $V_{810}H_{1550}$). Here, we are seeding with a tunable laser around 1550 nm and collecting the 810-nm downconversion photons.

process is formed. From this data, we can compare the spectra of the two processes and determine how to make the two processes more indistinguishable (i.e., by matching the amplitudes, bandwidths, and central wavelengths, as shown in Figure 3.17(b)). Alternatively, using a tunable filter (Newport TBF-1550-1.0-FCAPC with 0.05-nm tuning resolution) on the downconversion output allows for direct measurement of the downconversion spectra without the need to stimulate the process, e.g., with input fiber pigtailed sources, or if no precisely tunable seed laser is available. The tunable filter method is useful in cases where stimulated downconversion is not possible, but suffers from much lower rates than the stimulated downconversion technique; for fiber-pigtailed sources, the downconversion wavelengths cannot always be guided through the input pump fiber. For this waveguide source, both methods are used and show consistent results (Figure 3.18).

The simplest correction of any distinguishing features is to tune the central wavelength of the downconversion processes by changing the temperature of the entanglement source. Since the indices of refraction, and therefore phase-matching conditions, are temperature dependent [42], tuning the nonlinear crystal temperature allows the two downconversion

49
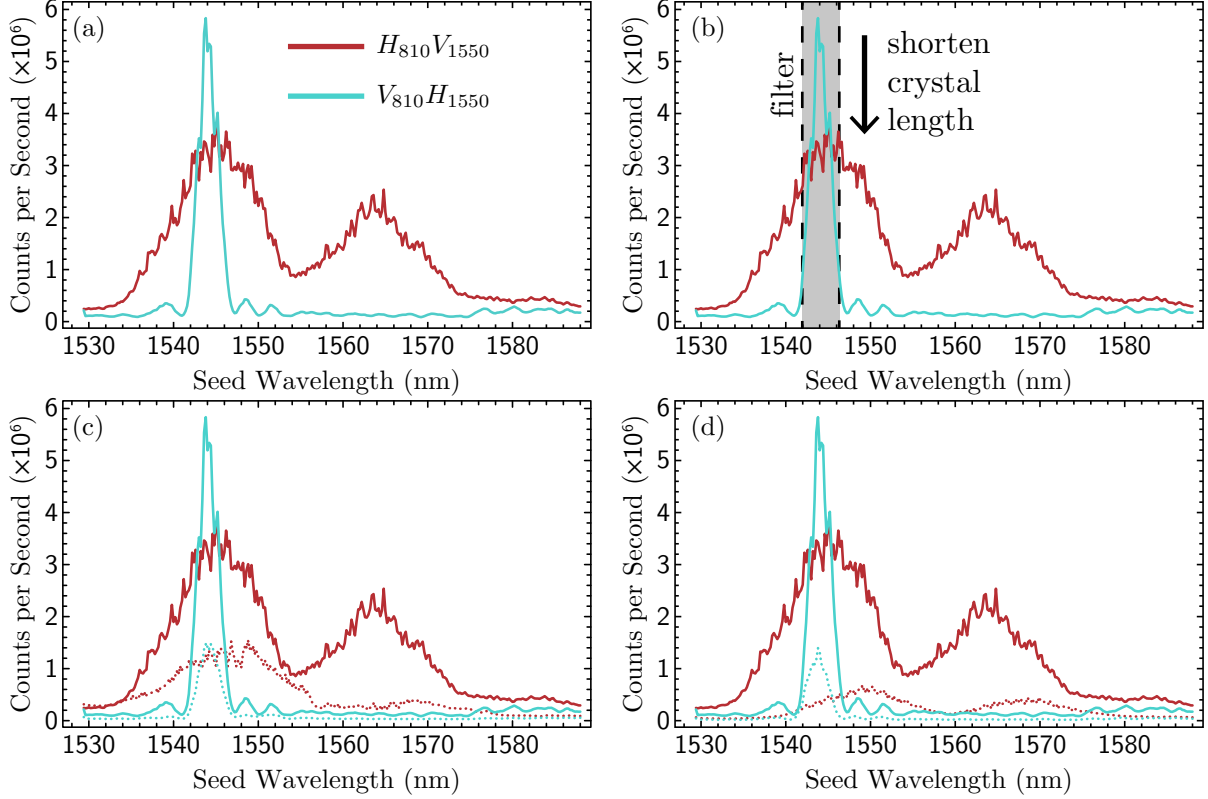
Figure 3.17: Stimulated Downconversion Measurements of the Downconversion Spectrum: (a) results of the stimulated downconversion measurement showing the optimal overlap of the two processes. The red (wider) curve represents the process $H_{810}V_{1550}$, and the blue (narrower) curve representes the process $V_{810}H_{1550}$. The secondary peak of the red curve (centered at 1564 nm) is an example of how the interacting triplet modes discussed in Section 2.5 can affect the downconversion spectra. (b) Removing distinguishing characteristics using filtering (gray shade) or reducing the length of one side of the crystal - which will also increase the bandwidth of the spectrum. (c) Comparing the spectra of different modes. The dotted curves show the spectrum when the pump is coupled into a less efficient waveguide mode[†††]. (d) Comparing the spectra versus temperature. The dotted curves show the spectrum at 30° C, whereas the spectral overlap of the two processes is improved at 40° C.

processes to overlap. Figure 3.19 shows how the two processes change with temperature, measured using the stimulated downconversion method: the x-axis is the seed wavelength for the stimulated downconversion; the y-axis is the crystal temperature; the plot color represents the counts per second measured. For the $H_{810}V_{1550}$ process, the spectrum peak changes by 10 nm for a temperature change of $\approx 30°$ C, whereas for the $V_{810}H_{1550}$ process, the peak is largely unaffected, only changing by about 2 nm over the same temperature range. This behavior is helpful for overlapping the processes, because the temperature tuning can essentially move the spectrum of the $H_{810}V_{1550}$ process on top of the $V_{810}H_{1550}$ spectrum without worrying about the latter peak moving. For the free-space coupled scheme, the
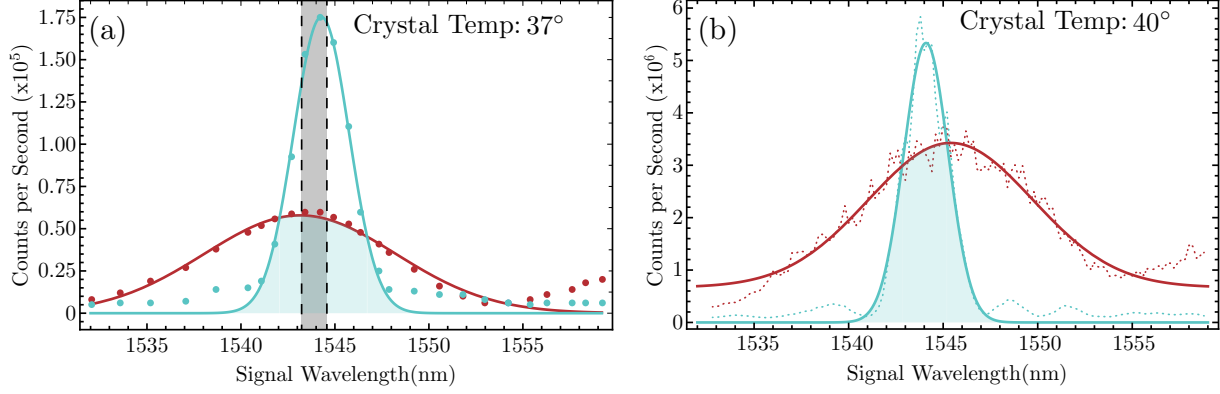
Figure 3.18: A Comparison of Methods for Measuring the Downconversion Spectra: the spectra of the waveguide downconversion source was measured twice: (a) using a tunable filter to measure the spontaneous idler counts vs. downconversion wavelength (here we detected the 1550-nm photons) for the fiber-coupled source; (b) using Stimulated Downconversion with a nominal seed wavelength of 1550 nm for the free-space source. The solid curves represent a gaussian fit of the dotted spectral data. The red curves represent the $|H_{810}V_{1550}\rangle$ process and the blue curves represent the $|V_{810}H_{1550}\rangle$ process. The blue-shaded areas show the overlap of the two gaussian fits and the grey-shaded area represents the bandwidth of the narrowband filter used. The difference in operating temperatures can be attributed to differing temperature calibrations for the temperature controllers used in the free-space and fiber-coupled scenarios.

optimal overlap temperature was found to be 40° C.

Once the spectra are overlapped via temperature tuning, the relevant part of the spectral data can be fit to gaussian curves[‡‡‡] $f_1(\omega)$ and $f_2(\omega)$ (Figure 3.18):

$$|\psi\rangle = \frac{1}{\sqrt{I_1 + I_2}} \int f_1(\omega)|H_\omega V_{\omega_s}\rangle + f_2(\omega)|V_\omega H_{\omega_s}\rangle d\omega, \qquad (3.9)$$

where $I_i = \int |f_i(\omega)|^2 \, d\omega$, $f_i(\omega) \approx Ae^{-(\omega-\omega_o)^2/2\sigma^2}$, ω is the seed/filter wavelength at a nominal value of 1550 nm, ω_s is the signal wavelength at a nominal value of 810 nm, and ω_o is the central wavelength of the gaussian fit. The estimated maximum entanglement fidelity (assuming perfect temporal compensation) can be calculated as follows[§§§]:

[‡‡‡]Technically, the downconversion processes should be modeled with $\text{sinc}^2 \omega$ functions; however, gaussians approximate the data well and actually better approximate the $H_{810}V_{1550}$ process due to the waveguide triplet-mode effect [32].

[§§§]Note this is only one side of the joint spectrum. In order to get a complete picture and more accurate estimate of the expected entanglement, a joint spectrum is useful. Unfortunately, we do not have the resources to perform such a measurement. However, since we have a narrowband pump, we can use this spectrum as an approximation of our complete downconversion spectrum.
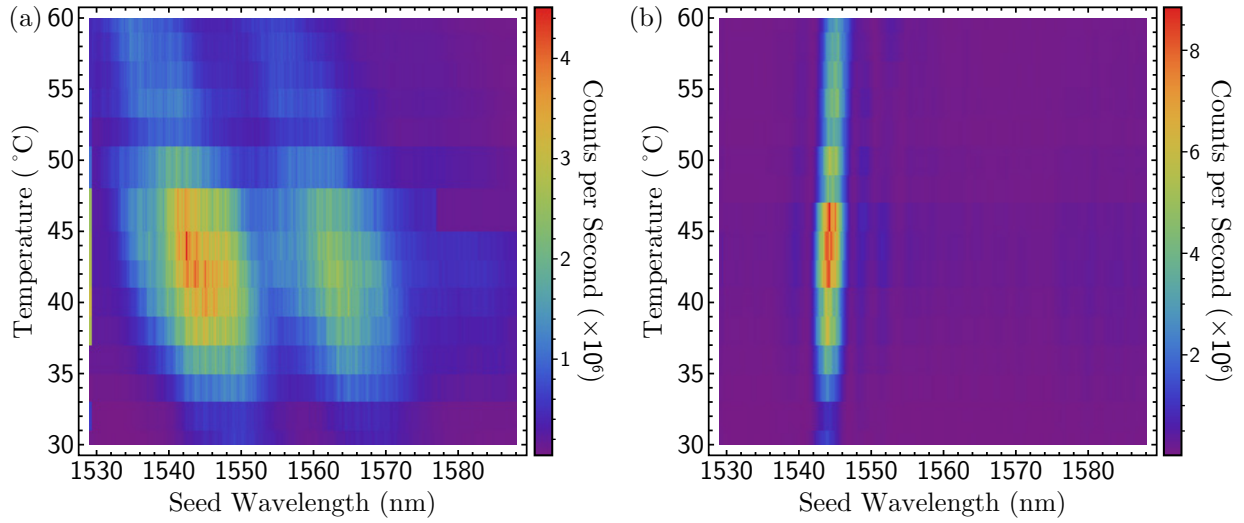
Figure 3.19: Downconversion Spectra Versus Crystal Temperature: simulated downconversion measurements showing how the downconversion spectra changes with crystal temperature for (a) the $H_{810}V_{1550}$ process and (b) the $V_{810}H_{1550}$ process.
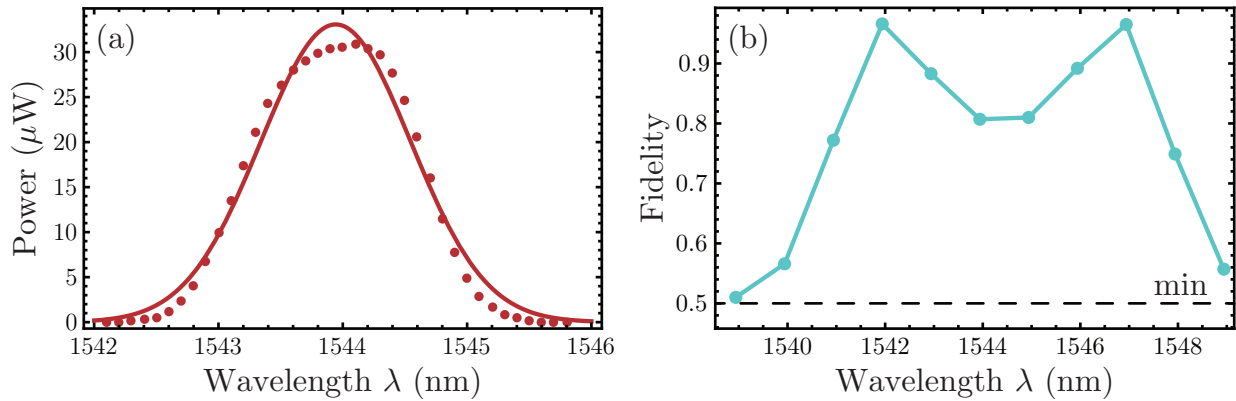
Figure 3.20: Measuring the Expected Fidelity Versus Filter Central Wavelength: (a) the measured bandwidth of a tunable filter with 0.05-nm tuning resolution (Newport TBF-1550-1.0-FCAPC) at central wavelength 1543.94 nm, fit to a gaussian curve. (b) The simulated expected fidelity versus central wavelength of the tunable filter. The peaks on either side of the center are due to the fact that the amplitudes of the two processes are more equal as the filter moves away from the center of the two processes.

$$|\langle\psi^+|\psi\rangle|^2 = \int |\frac{1}{\sqrt{2}}(\langle H_\omega V_{\omega_s}| + \langle V_\omega H_{\omega_s}|)(\frac{1}{\sqrt{I_1+I_2}})(f_1(\omega)|H_\omega V_{\omega_s}\rangle + f_2(\omega)|V_\omega H_{\omega_s}\rangle)|^2 \, d\omega$$

$$= \frac{1}{2(I_1+I_2)} \int |(f_1(\omega) + f_2(\omega)|^2 \, d\omega$$

$$= \frac{1}{2(I_1+I_2)} \left(\int |f_1(\omega)|^2 \, d\omega + \int f_1(\omega)f_2^*(\omega) \, d\omega + \int f_2(\omega)f_1^*(\omega) \, d\omega + \int |f_2(\omega)|^2 \, d\omega \right)$$

$$= \frac{1}{2(I_1+I_2)} \left(I_1 + 2\int |f_2(\omega)f_1(\omega)| \, d\omega + I_2 \right)$$

$$= \frac{1}{2} + \frac{1}{I_1+I_2} \int |f_2(\omega)f_1(\omega)| \, d\omega. \tag{3.10}$$

For the overlap shown in Figure 3.18(a) (with no narrowband filter), the calculated maximum fidelity with the maximally entangled state, $|\psi^+\rangle$, is 0.81. For the overlap shown in Figure 3.18(b), the calculated maximum fidelity is 0.97, where here we assume a FWHM filter bandwidth of $\Delta\lambda = 1.4$ nm, as shown by the gray-shaded area in Figure 3.18(b), which defines the limits of integration for Equation 3.10. If we simulate varying the center wavelength of the filter and plot the fidelity (Figure 3.20), we find that the optimal positioning for the filter central wavelength is not centered on the two processes. We believe this is because as the filter moves away from the center of the two processes, the amplitudes of the two processes become more evenly matched. We show this experimentally by tuning the central wavelength of our filter to maximize the entanglement fidelity, as shown in Figure 3.21. Figure 3.21(a) is an example of a pure state ($\gamma_a = 0.930 \pm 0.005$) that has low entanglement ($C_a = 0.088 \pm 0.019$) and fidelity ($F = 0.543$) due to the fact that only one process is efficiently collected (filter center: $\lambda_a = 1547.9$ nm). Figures 3.21(b) and (d) show filter locations (center: $\lambda_b = 1546.4$ nm and $\lambda_d = 1544.2$ nm) that yield higher non-optimal purities ($\gamma_b = 0.923 \pm 0.009$ and $\gamma_d = 0.951 \pm 0.005$), concurrence ($C_b = 0.825 \pm 0.011$ and $C_d = 0.953 \pm 0.004$), and fidelity ($F_b = 0.905$ and $F_d = 0.965$). Finally, Figure 3.21(c) shows the filter location (center: $\lambda_d = 1545.7$ nm) that resulted in the best metrics yet from this source ($\gamma_c = 0.990 \pm 0.005$, $C_c = 0.983 \pm 0.004$ and $F = 0.986$).

By widening the limits of integration, we find that the fidelity hits a simulated lower limit of $F = 0.82$ at a filter FWHM $\Delta\lambda = 20$ nm centered at 1545 nm, which is equivalent to
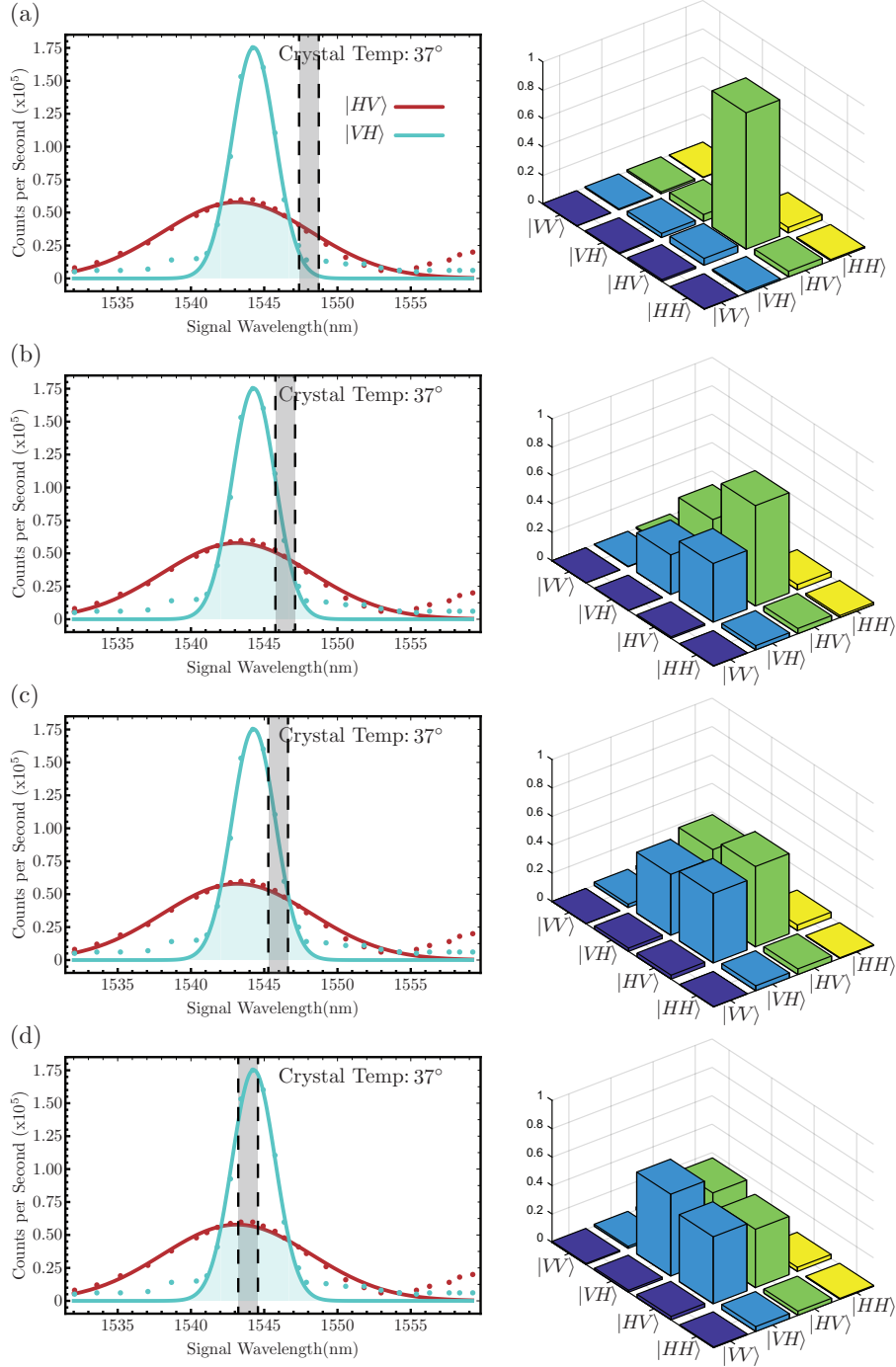
Figure 3.21: The Measured Density Matrix Versus Filter Central Wavelength: by scanning the central wavelength of a tunable narrowband filter (collection bandwidth represented by gray-shaded area), the entanglement metrics vary. (a) is an example of a pure state ($\gamma_a = 0.930 \pm 0.005$) that has low entanglement ($C_a = 0.088 \pm 0.019$) and fidelity ($F = 0.543$) due to the fact that only one process is efficiently collected. (b) and (d) show filter locations that yield higher non-optimal purities ($\gamma_b = 0.923 \pm 0.009$ and $\gamma_d = 0.951 \pm 0.005$), concurrence ($C_b = 0.825 \pm 0.011$ and $C_d = 0.953 \pm 0.004$), and fidelity ($F_b = 0.905$ and $F_d = 0.965$). (c) shows the filter location that resulted in the best metrics yet from this source ($\gamma_c = 0.990 \pm 0.005$, $C_c = 0.983 \pm 0.004$ and $F = 0.986$).

the case where we do not use any filtering beyond filtering the pump. To increase the source fidelity without the use of very narrowband filtering, the part of the crystal that creates the $V_{810}H_{1550}$ process (the tall, narrow peak), can be polished down in order to shorten the interaction length and decrease the strength of the downconversion process in order to match the amplitude of the other process. By shortening the section, the bandwidth of the spectrum for that process should widen, better matching the bandwidth of the other process. This final step must be accomplished by our collaborators at AdvR, Inc. By matching the inherent downconversion spectra instead of using narrowband filtering, we can improve the overall brightness of the source since we will no longer post-select on a small subset of pairs. Currently, we can achieve 10^5 810-nm singles counts, 10^4 1550-nm singles counts, and ~ 450 cps in coincidence per mW of pump power. As a comparison, the metrology experiment presented in Chapter 4 requires 10^4 cps in coincidence¶¶¶.

In conclusion, we have experimentally demonstrated the first-ever (to our knowledge) highly nondegenerate source of polarization-entangled photon pairs in a waveguide with an accidental-corrected state fidelity of $F = 0.986$, concurrence of $C = 0.983\pm0.004$, and purity of $\gamma = 0.990\pm0.005$. These metrics are suitable for the aforementioned quantum information and metrology protocols and present great progress towards creating integrated photonic sources with optimal SWaP for mobile quantum networks. Further work can be done to improve the source entanglement by better-matching the process spectra and by lowering the occurrence of accidental coincidences (i.e., coincidences that are not a result of both photons from one pair being detected coincidentally: two-pair events; leaking pump; background). Additionally, by alleviating the need for narrowband filtering through spectral matching, we can vastly improve the brightness of the source (current brightness is ≈ 450 pairs/s/mW).

¶¶¶Waveguides suffer from low heralding efficiency (the ratio between coincidence counts and singles) due to the reflections off the output facet of the downconversion crystal, e.g., if one photon from a pair reflects off the output facet, but the other photon from the pair transmits, then the transmitting photon will be recorded as a singles count and not a coincidence count.

Chapter 4

Application: Attosecond Metrology

One application of a highly nondegenerate polarization-entanglement source is to use the high frequency detuning of the downconverted photons to achieve ultra-high resolution interferometer-based timing resolution. An interferometer capable of performing quantum interference of frequency-entangled photons may be used to perform spatial measurements on the nanometer scale or smaller while possessing inherent robustness against optical background noise, optical dispersive effects, and optical losses. Combining HOM (introduced in Section 1.1.2) and Mach-Zehnder interference allows a nondegenerate polarization-entangled two-qubit state, transformed into a frequency-entangled state, to produce attosecond-level timing resolution without the need for an ultra-broadband light source. Such a device has a multitude of applications that include but are not limited to: remote and contactless detection of vibrations such as those originating from machinery or sound waves, non-invasive high-resolution probing of delicate materials (e.g., biological tissues), and stealth measurements secure against spoofing attacks. A proof-of-principle of this interferometer scheme was accomplished by Chen et al. [43]; however, they used a detuning of only a few tens of THz (corresponding to tens of nanometers), limiting their resolution to 640 attoseconds (190 nm) over 104 trials. With the highly nondegenerate photon pairs produced from sources in our lab, we expect to achieve a resolution on the order of a few attoseconds ($\sim$ nanometers), which represents a two orders-of-magnitude improvement. In this chapter, the theory behind this claim* will be presented along with the experimental setup and preliminary results. The advantages of this method will be contrasted with classical interference techniques and its potential applications will be discussed.

---

*Credit is given to Spencer Johnson for working on the theory and experiment and Colin Lualdi for working on the experiment for this project.
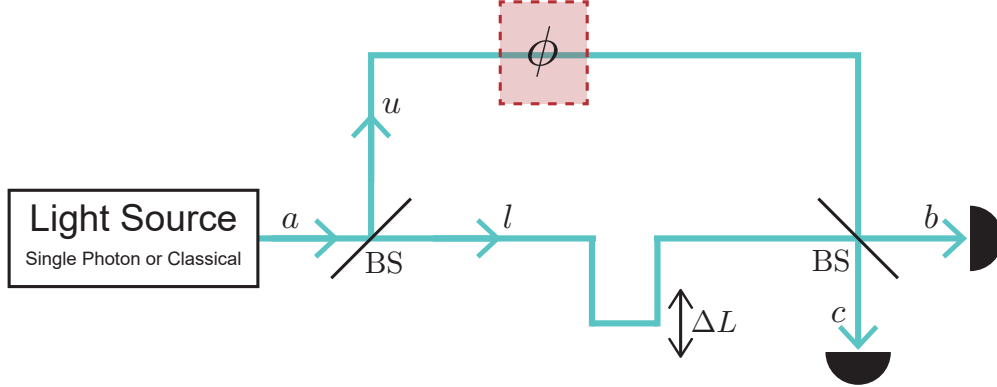
Figure 4.1: A standard Mach-Zehnder interferometer. A photon in mode a is incident on a 50:50 BS, after which it is in a superposition of the upper (u) path and the lower (l) path. The two modes are recombined on a second 50:50 BS and split again into two modes, b and c. A variable delay ΔL is placed in the lower path in order to adjust the timing between the upper and lower modes.

4.1 Classical Mach-Zehnder and Quantum HOM Interferometry

The proposed quantum metrology experiment combines two types of interference: Mach-Zehnder (classical) and HOM (quantum). In a standard Mach-Zehnder interferometer, a single photon (or classical wave) in mode a is incident on a 50:50 BS, splits into two different modes and is then recombined on a second 50:50 BS[†]. The photon in the superposition of two modes after the second BS is then collected onto detectors, as shown in Figure 4.1. Mathematically, we can represent this transformation by tracking the photon's modes as it travels through the interferometer. First, the single photon in mode a splits into two paths on a 50:50 BS:

$$|1\rangle_a \rightarrow \frac{1}{\sqrt{2}}(|1\rangle_l + i|1\rangle_u),\tag{4.1}$$

where u and l represent the upper and lower paths, respectively, and the factor of i in the second term is picked up from the reflection off of the BS. The upper and lower paths are assumed to be equal in length, a requirement that can be accomplished using an optical delay line in one of the two paths, as shown in Figure 4.1. A phase shift in the upper arm presents itself as an $e^{i\phi}$ multiplicative factor on the second term:

[†]This is true for all classical interferometers, e.g., the Michelson interferometer, in addition to the Mach-Zehnder interferometer. In this work, the Mach-Zehnder is treated, as it is the specific interferometer geometry used for this experiment.

$$|1\rangle_a \rightarrow \frac{1}{\sqrt{2}}(|1\rangle_l + ie^{i\phi}|1\rangle_u). \tag{4.2}$$

The two paths then recombine on the second BS. To do this transformation, all four possibilities have to be accounted for: the photon traveled in the upper mode u and reflects off the second BS (mode b), the photon traveled in the upper mode u and transmits through the BS (mode c), the photon traveled in the lower mode l and transmits through the BS (mode b), and the photon traveled in the lower mode and reflects off the BS (mode c). Mathematically, we can represent this as the upper and lower modes becoming superpositions of modes b and c:

$$|1\rangle_u \rightarrow \frac{1}{\sqrt{2}}(i|1\rangle_b + |1\rangle_c)$$
$$|1\rangle_l \rightarrow \frac{1}{\sqrt{2}}(|1\rangle_b + i|1\rangle_c). \tag{4.3}$$

Combining Equations 4.2 and 4.3, the final state at the detectors can be represented as

$$|1\rangle_a \rightarrow \frac{1}{\sqrt{2}}(|1\rangle_l + ie^{i\phi}|1\rangle_u) \rightarrow \frac{1}{\sqrt{2}}(\frac{1}{\sqrt{2}}(|1\rangle_b + i|1\rangle_c)) + ie^{i\phi}(\frac{1}{\sqrt{2}}(i|1\rangle_b + |1\rangle_c))$$
$$= \frac{1}{2}\big((1 - e^{i\phi})|1\rangle_b + i(1 + e^{i\phi})|1\rangle_c\big), \tag{4.4}$$

corresponding to a detector signal that oscillates with respect to the phase ϕ in the upper path (plotted in Figure 4.3(a)):

$$P(b) = |\frac{1}{2}(1 - e^{i\phi})|^2 = \frac{1}{2}(1 - \cos\phi) \tag{4.5}$$
$$P(c) = |\frac{i}{2}(1 + e^{i\phi})|^2 = \frac{1}{2}(1 + \cos\phi). \tag{4.6}$$

This shows that small differences in the effective length of either path, changing the relative phase ϕ, produces sinusoidal interference fringes at the interferometer output. One will
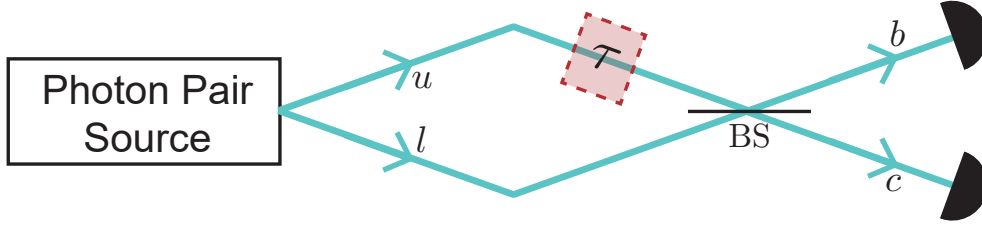
Figure 4.2: A standard HOM interferometer. An entangled photon pair with each photon in a different mode is incident on a 50:50 BS. The output modes, b and c are then detected. If the photons are indistinguishable and arrive simultaneously at the beamsplitter, the probability of coincident photon detections is zero.

gain the maximum phase sensitivity when the signal varies linearly with ϕ, i.e., around $\phi = \pi/2, 3\pi/2, \cdot$. We see immediately that the relative parameter is the slope of the interferometer response, $dR/d\phi$, where $R \equiv (P(c) - P(b))/(P(c) + P(b)) = \cos\phi$. Furthermore, shorter wavelength will result in higher resolution metrology. Given that optical frequencies have wavelengths of hundreds of nanometers, Mach-Zehnder optical interferometers can be used to make high-resolution measurements with accessible and easy-to-use light sources.

Such "classical" interference suffers, however, from several drawbacks that limit its utility. For example, the phase sensitivity of the interferometer can be degraded when dispersive media (such as the material used to induce the relative phase, ϕ) is introduced, e.g. for testing purposes, into one of the interferometer's paths. Since photon wavepackets have a finite bandwidth, the wavelength-dependent refractive index of the dispersive media will cause the relative phase acquired by each frequency component to differ, thereby reducing the phase resolution with washed-out interference fringes. A similar reduction in fringe visibility occurs when the interferometer experiences unbalanced loss in one path compared to the other. Next we see that two-photon interference can be used to achieve similar capabilities, but with robustness to relative loss, noise, and dispersion.

HOM interference, introduced in Section 1.1.2, differs from Mach-Zehnder interference as the input is a two-photon quantum state in two different modes $|1\rangle_l|1\rangle_u$ (Figure 4.2), instead of a one-photon state that is split into a superposition of two modes on an initial BS. For example, a photon pair produced from a degenerate frequency SPDC source is a suitable input state to a HOM interferometer. Using the same techniques as with the Mach-Zehnder interferometer, the probability of detection in modes b and c can be written as,
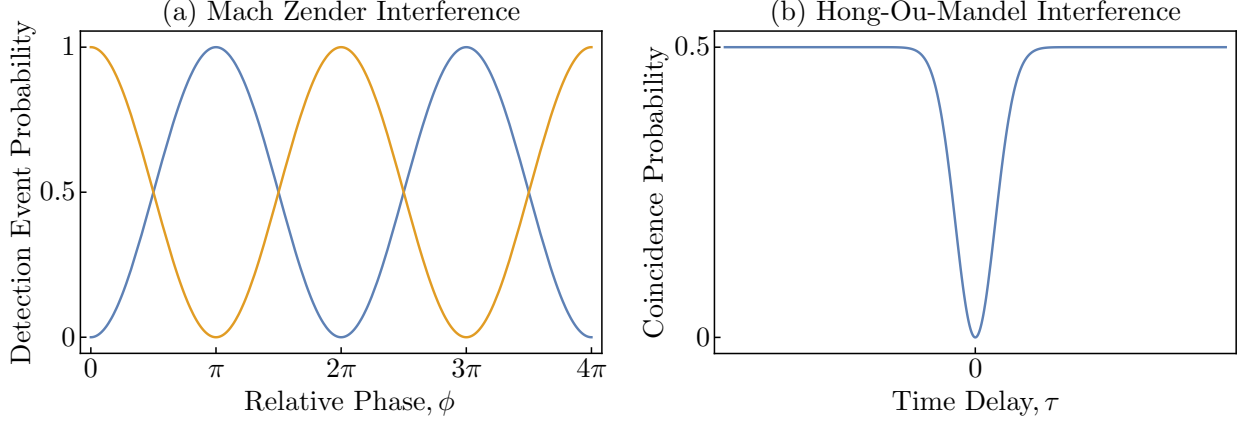
Figure 4.3: (a) A plot of the probabilities of detection, $P(b)$ and $P(c)$, for detectors in path b and c, respectively. (b) The coincidence probability, $P(b,c)$, with respect to the time delay, τ.

$$|1\rangle_l|1\rangle_u \rightarrow \frac{1}{2}\big(|1\rangle_b + i|1\rangle_c\big)\big(i|1\rangle_b + |1\rangle_c\big)$$

$$= \frac{1}{2}\big(i|1\rangle_b|1\rangle_b + |1\rangle_b|1\rangle_c - |1\rangle_c|1\rangle_b + i|1\rangle_c|1\rangle_c\big)$$

$$= \frac{1}{2}\big(i|1\rangle_b|1\rangle_b + i|1\rangle_c|1\rangle_c\big) = \frac{1}{2}\big(i\sqrt{2}|2\rangle_b + i\sqrt{2}|2\rangle_c\big)$$

$$P(b) = |\frac{i\sqrt{2}}{2}|2\rangle_b|^2 = \frac{1}{2} = P(c). \tag{4.7}$$

As seen in Section 1.1.2, if the two photons are indistinguishable, the two coincident terms cancel out ($P(b,c) = 0$) and the photons are either both in mode b or both in mode c with 50% probability. However, this derivation assumes photons with zero bandwidths, which is not realistic. In practice, the photons will have a non-zero bandwidth 2σ, and any time delay τ between the two photons arriving at the BS will introduce distinguishability. Defining the photon wavepacket as $|1\rangle \equiv \int f_i(\omega)a^\dagger(\omega)d\omega|0\rangle$ where $f_i(\omega) \propto e^{\frac{-(\omega-\omega_i)^2}{2\sigma^2}}$, the coincidence probability can be rewritten as

$$P(b,c) = \frac{1}{2}\big(1 - e^{-2\sigma^2\tau^2}\big), \tag{4.8}$$

as shown in Figure 4.4. Therefore, by placing a detector in modes b and c and scanning through the photons' relative time-of-arrival, one will observe a dip in the coincidence prob-

ability when the photons arrive simultaneously.

In contrast to the Mach-Zehnder interference, HOM interference is independent of relative phase and relative loss. To understand this, consider again the case of monochromatic HOM interference with a factor of $\sqrt{\tau}e^{i\phi}$, e.g., in the upper arm before the beamsplitter. The new input state will be $|\psi\rangle = \sqrt{\tau}e^{i\phi}|1\rangle_u|1\rangle_l$, which does not change the overall effect of the coincident processes canceling. We can also consider the effect of noise on the detectors, either from background or detector dark counts. The effect is substantially reduced compared to a classical interferometer, since here the minimum is only increased if there are coincident noise counts, i.e., both detectors must receive them. Finally, if the photons used as inputs to a HOM interferometer are energy entangled, i.e., described as $\int |\omega_p/2 + \omega\rangle_s|\omega_p/2 + \omega\rangle_i \, d\omega$, then it has been shown that the HOM dip visibility is not affected by odd orders of group velocity dispersion [44]. However, as mentioned above, a monochromatic HOM interference is unrealistic. Since the photons are wavepackets with some bandwidth, a relative phase between the two paths will affect the distinguishability of the photons, which will degrade the interference visibility. However, HOM interference is relatively robust to this phase as the typical width of the HOM dip is $\sim 100\mu$m which is much bigger than its corresponding phase. Thus, although the phase does affect the intereference visibility, it does not negate the cancellation effect at $\tau = 0$ and overall has a small effect on the performance of the interferometer. The resolution of HOM interference measurements is determined by the overall width of the HOM dip, which is inversely related to the photons' bandwidth 2σ. Consequently, one must perform HOM interference with ever-larger-bandwidth photons to measure increasingly small differences in relative time-of-arrival; however, it is nontrivial to produce such ultra-broadband photon.

In the derivation above we assumed the photons had the same frequency; for standard HOM, a frequency detuning between the two input photons would result in a supression of the HOM dip, as the two destructively interfering processes - both photons transmitted or both photon reflected - are then distinguishable. For example, if the signal and idler wavelengths are 806 and 814 nm, respectively, the frequency detuning would be $\Delta\omega = c(1/806\,\text{nm} - 1/814\,\text{nm}) = 23$ THz. Given a photon bandwidth 2σ on the order of tenths of nanometers, the HOM dip would already be surpressed by 47 orders of magnitude. To circumvent this

issue, a frequency-entangled input state is used. Consider a HOM interferometer with an input state entangled in frequency and with some relative temporal delay in the upper path:

$$|\psi_{in}\rangle = \frac{1}{\sqrt{2}}\big(e^{i\omega_2\tau}|\omega_1\rangle_l|\omega_2\rangle_u + e^{i\omega_1\tau}|\omega_1\rangle_u|\omega_2\rangle_l\big) = \frac{1}{\sqrt{2}}\big(|\omega_1\rangle_l|\omega_2\rangle_u + e^{i(\omega_1-\omega_2)\tau}|\omega_1\rangle_u|\omega_2\rangle_l\big). \quad (4.9)$$

As with the previous HOM interference protocol, this state is incident on a 50:50 BS with output modes b and c, resulting in 4 possible results depending on ω and which path was taken:

$$
\begin{aligned}
|\omega_1\rangle_l &\to \frac{1}{\sqrt{2}}(|\omega_1\rangle_b + i|\omega_1\rangle_c) \\
|\omega_1\rangle_u &\to \frac{1}{\sqrt{2}}(i|\omega_1\rangle_b + |\omega_1\rangle_c) \\
|\omega_2\rangle_l &\to \frac{1}{\sqrt{2}}(|\omega_2\rangle_b + i|\omega_2\rangle_c) \\
|\omega_2\rangle_u &\to \frac{1}{\sqrt{2}}(i|\omega_2\rangle_b + |\omega_2\rangle_c).
\end{aligned}
\quad (4.10)
$$

Combining these results with the input state in Equation 4.9, the total output state can be written and simplified as,

$$
\begin{aligned}
|\psi_{out}\rangle &= \frac{1}{2\sqrt{2}}\big((|\omega_1\rangle_b + i|\omega_1\rangle_c)(i|\omega_2\rangle_b + |\omega_2\rangle_c) \\
&\quad + e^{i(\omega_1-\omega_2)\tau}(i|\omega_1\rangle_b + |\omega_1\rangle_c)(|\omega_2\rangle_b + i|\omega_2\rangle_c)\big) \\
&= \frac{1}{2\sqrt{2}}\big((i|\omega_1,\omega_2\rangle_b + |\omega_1\rangle_b|\omega_2\rangle_c - |\omega_1\rangle_c|\omega_2\rangle_b + i|\omega_1,\omega_2\rangle_c) \\
&\quad + e^{i(\omega_1-\omega_2)\tau}(i|\omega_1,\omega_2\rangle_b - |\omega_1\rangle_b|\omega_2\rangle_c + |\omega_1\rangle_c|\omega_2\rangle_b + i|\omega_1,\omega_2\rangle_c)\big) \\
&= \frac{1}{2\sqrt{2}}\big((1 + e^{i(\omega_1-\omega_2)\tau})(i|\omega_1,\omega_2\rangle_b + i|\omega_1,\omega_2\rangle_c) \\
&\quad + (1 - e^{i(\omega_1-\omega_2)\tau})(|\omega_1\rangle_b|\omega_2\rangle_c - |\omega_1\rangle_c|\omega_2\rangle_b)\big),
\end{aligned}
\quad (4.11)
$$

which gives a coincidence probability of:

$$P(b,c) = 2 * |\frac{1}{2\sqrt{2}}(1 - e^{i(\omega_1 - \omega_2)\tau})|^2$$

$$= \frac{2}{8}(1 - e^{i(\omega_1 - \omega_2)\tau})(1 - e^{-i(\omega_1 - \omega_2)\tau})$$

$$= \frac{1}{4}\left(2 - (e^{i(\omega_1 - \omega_2)\tau} + e^{-i(\omega_1 - \omega_2)\tau})\right)$$

$$= \frac{1}{2}\left(1 - \cos\left((\omega_1 - \omega_2)\tau\right)\right). \tag{4.12}$$

Finally, accounting for the non-zero bandwidth of the photon wavepackets (assuming identical bandwidths), the final output state is

$$P(b,c) = \frac{1}{2}\left(1 - \cos\left((\Delta\omega)\tau\right)e^{-2\sigma^2\tau^2}\right), \tag{4.13}$$

where $\Delta\omega$ is the frequency detuning of the two input photons. This is reminiscent of both the Mach-Zehnder count probability and the HOM coincidence probability and is plotted in Figure 4.4. Since the frequency of the fringes within the overarching HOM dip is dependent on the frequency detuning $\Delta\omega$ of the downconversion photons (opposed to the photons' bandwidths in conventional HOM), going to large detunings allows for high-frequency oscillations and higher time-resolving ability. For example, using the detuning given by the sources featured in this work ($\Delta\omega = \omega_{810} - \omega_{1550} \approx 177$ THz), a timing resolution of a few attoseconds is possible. This approach retains the primary advantages of HOM - resilience to dispersion, unbalanced loss, and background noise - with the precision of classical interferometry.

Our scheme is very similar to "quantum optical coherence tomography" schemes that have been proposed and demonstrated [45–49]. Like our system, these schemes involve performing two-photon quantum interference using pairs of entangled photons and demonstrate robustness against dispersion, loss, and background noise. However, in these systems the measurement resolution is limited by the bandwidth of the photons used. While this has been partially resolved with the use of ultra-broadband photons, use of such photons make
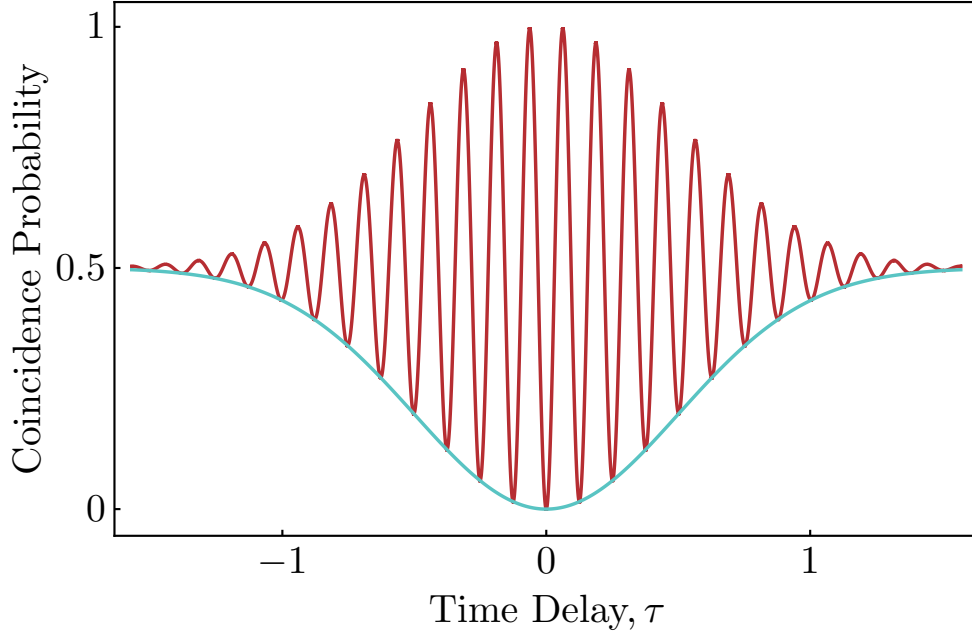
Figure 4.4: A plot of the coincidence probability vs time delay for a HOM interferometer. The red curve shows the coincidence probability for the frequency-entangled HOM interference and the blue curve shows the coincidence probability for standard HOM interference.

these systems very challenging to calibrate, e.g., the transmission of the interferometer arms should be uniform across the spectrum. Our system does not use ultra-broadband photons; instead we use narrowband, but highly non-degenerate photons, resulting in much better sensitivity while also making the system far easier to calibrate, by virtue of the narrowband nature of the photons.

4.2 Experimental Design and Results

To realize frequency-entangled HOM interference resulting in a timing resolution of a few attoseconds, we use a source of highly nondegenerate polarization-entangled photon pairs and convert their polarization entanglement into frequency entanglement. To do so, the entangled photon pairs are split by polarization on a highly achromatic PBS (Optosigma, custom-coating, Tp > 95%, Rs > 97%, Ts:Tp = 1:1000,) as shown in Figure 4.5. The PBS reflects the vertically polarized photons into the upper path and transmits the horizontally polarized photons into the lower path. Using a HWP (Newlight Photonics, retardance: 810 nm: 0.502 λ; 1550 nm: 0.504 λ, transmission: 810 nm: >99.5%; 1550 nm: >99.5%)
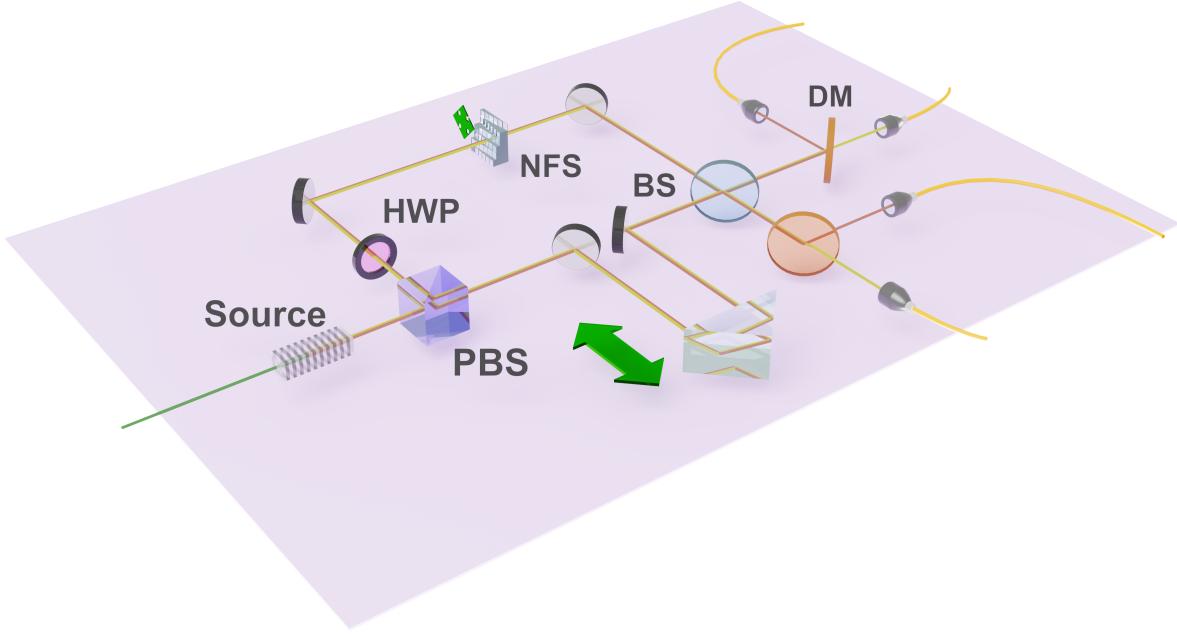
Figure 4.5: Experimental setup for frequency-entangled HOM interference. A two-qubit polarization-entangled quantum state impinges on a PBS. The vertically polarized photons are reflected into the upper path and their polarization is rotated to horizontal using a HWP set at 45°; and the horizontally photons are transmitted into the lower path. The two paths are then recombined on a 50:50 BS. A trombone-based optical delay is added to the lower path in order to adjust the upper and lower path lengths. A nano-fabricated sample (NFS) is shown in the upper path as an example of a dispersive test element. After the 50:50 BS, the photon state is split again on two DM, which allows for detection of the two wavelengths on different types of detectors. The photons are then coupled into single-mode fibers and directed to their respective detectors.

in the upper path, the polarization of vertically polarized photons is rotated to horizontal. Now, photons in both the upper and lower paths are horizontally polarized and the new photon state is entangled in frequency instead of polarization:

$$\begin{aligned}
|\psi\rangle &= \frac{1}{\sqrt{2}}\big(|H_{\omega_1}V_{\omega_2}\rangle + |V_{\omega_1}H_{\omega_2}\rangle\big) \\
&\rightarrow \frac{i}{\sqrt{2}}\big(|\omega_1\rangle_l|\omega_2\rangle_u + |\omega_1\rangle_u|\omega_2\rangle_l\big) \otimes |H\rangle.
\end{aligned} \tag{4.14}$$

The photons are then recombined on a 50:50 BS (Optosigma, custom-coating, Ts = Tp = 50%±10%)[‡] and the output state can be treated as before in the frequency-entangled

---

[‡]Note that it is somewhat important that the BS splitting ratio be ≈ 50/50 for both incident wavelengths.
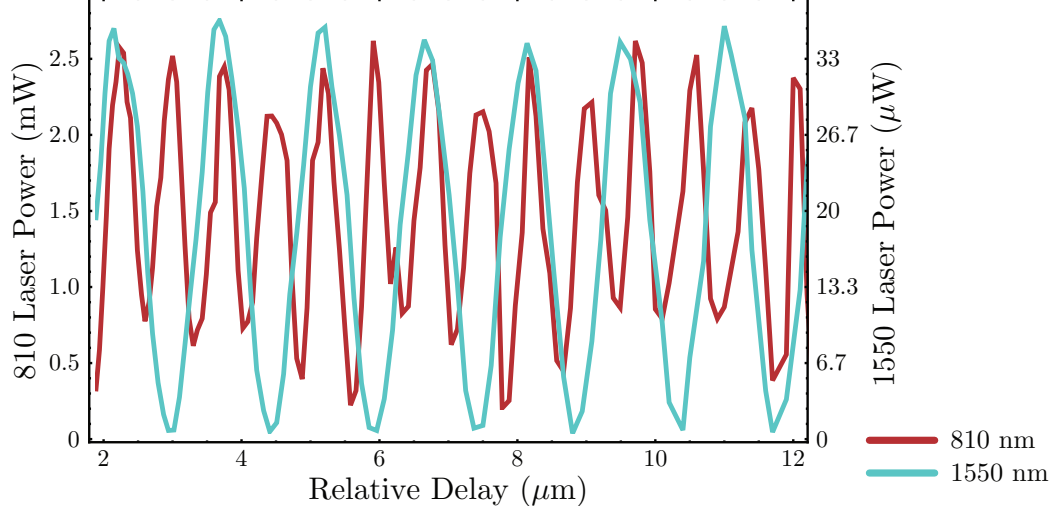
Figure 4.6: Fringes showing the dual-wavelength capabilities of the interferometer scheme. The red curve shows the 810-nm interference fringes and the blue curve shows the 1550-nm interference fringes.

HOM derivation. The two output modes of the 50:50 BS are sent through dichroic mirrors (Thorlabs - DMLP950) and split by frequency, allowing the use of different detectors for the two wavelengths. This separation does not affect the distinguishability of the photons, and so allows us to directly measure coincident and non-coincident events without compromising interferometer visibility. The outputs of the DMs are then coupled into single-mode fibers for their respective wavelengths and sent to separate SNSPDs that are optimized for 810 nm (Quantum Opus) and 1550 nm (JPL). For optimization of the resulting interference fringes, two broadband mirrors (Thorlabs, PF10-03-M03, R>97% for 800 nm - 20 μm) are placed on a hybrid piezo- and actuator-driven translation stage (PI, sub-nm step sizes and mm travel) for a trombone-style variable path delay. Finally, for the actual fringe measurement, a rotating phase-inducing glass window with a rotation axis perpendicular to the beam path provides a variable phase in the upper path of the interferometer. Later, this optic will be replaced with actual test samples that we can probe using our interferometer.

Thus far, we have measured the dual-wavelength capabilities of our interferometer; Figure 4.6 shows the resulting classical interference fringes for both 810- and 1550-nm light with fringe visibility of $\approx$ 79% and $\approx$ 98%[§], respectively, while adjusting the path delay

---

[§]These measurements were made using off-the-shelf beamsplitters. We can attribute the jagged 810-nm fringes to multiple reflections off the beamsplitters interfering. We believe once we replace the current beamsplitters with the custom-coated dual-wavelength beamsplitters, we will achieve high fringe visibility for 810-nm light. Note also that such multi-reflection fringes are only possible if the coherence length of the

with the trombone. Given the high-fidelity polarization entanglement achieved with the consecutively poled waveguide SPDC source, the final step will be interfacing this source with the dual-wavelength interferometer. Once the interfacing is optimized, an experimental demonstration of the interference beat shown in Figure 4.4 is possible. For interfacing, it is sufficient that the two paths for a given frequency arrive simultaneously (to within the reciprocal bandwidth). Different colors need not arrive simultaneously, since they will be measured by different detectors anyway. With this system we expect to achieve a time resolution below 10 attoseconds (nanometer-scale path difference) for 10^4 photon pairs, representing an improvement of ~ 2 orders of magnitude compared to [43].

4.3 Applications

There are countless mechanisms that can introduce small time delays in one path of an interferometer, ranging from mechanical vibrations to non-uniform surface topography of materials like biological tissues. Our method can be utilized to perform measurements on such systems with a resolution comparable to or surpassing other existing measurement and interferometry techniques, and in environments where existing technologies are unable to obtain reliable measurements due to factors such as unwanted noise, loss, incompatible materials, and stealth considerations. This need for precise, non-destructive measurements is of increasing importance in the engineering of nanofabricated devices as well as the study of biological materials. However, precise measurements of many materials can be challenging with current methods. These measurements typically rely on classical interference to achieve nanometer-scale resolution as discussed in Section 4.1. This limits the number of applicable systems, as classical interference has reduced precision in the presence of noise and when looking at lossy and dispersive materials such as biological tissue and glass. Further, the powers required to utilize classical interference can cause heating of the sample and other measurement devices, such as in the case of atomic force microscopy (AFM). These advantages altogether will enable novel sensing schemes in regimes beyond the ca-

---

light is greater than the path length between the offending optical surfaces; this will not be the case with our SPDC photons.

pabilities of state-of-the-art classical interferometers. Possible applications utilizing these new capabilities to advance current technology include: stealth and security (make unobstructive measurements via single photons and use entanglement to protect against spoofing attacks), differential ranging (conduct short- or long-distance differential ranging in lossy dispersive environments with low photon fluxes), precision tomography (probe the topography of highly dispersive or lossy thin films), and medical imaging (perform non-invasive, high-resolution imaging of delicate tissues via quantum optical coherence tomography). In addition to enabling new technologies, the results from our proposed work will guide future research steps. For instance, it is an open question whether it is possible to optimize the entangled state used for specific sensing applications (e.g., entanglement between more than two frequencies, additional time-bin entanglement, etc.). We are also interested in the possibility of leveraging the narrowband nature of the photons used by our system to achieve new capabilities beyond ease of path-length matching and robustness against dispersion. Furthermore, since our system only performs measurements at the single-photon level, the ability to collect enough light for rapid measurements is a concern. However, modern SPDC sources generate a large number of single photons in a short amount of time [21], allowing one to reach high resolutions in only a fraction of a second. Therefore, we believe probing is not limited to static samples; one can also perform measurements on dynamic systems, such as analyzing blood flow through blood vessels by measuring minute displacements of the vessel wall due to vibrations induced by flowing fluids.

In conclusion, the hundred-fold improvement in resolution offered by our proposed interferometer will enable, for the first time, sensing on the attosecond (nanometer) scale via HOM interference without the need for ultra-broadband sources –the individual frequencies ω_1 and ω_2 have bandwidths below 1 THz, which reduces dispersion effects and simplifies interferometer calibration by virtue of much wider HOM dips. Furthermore, the use of HOM interference as the primary mechanism undergirding our measurement scheme offers the following main benefits: dispersion resistance (facilitates high-resolution probing of dispersive materials), robustness against loss (permits characterization of lossy materials with great precision), noise resilience (enables measurements in presence of background (noise) photons), and information efficiency (allows achieving higher resolutions with fewer photons).

Chapter 5

Degenerate Source of Polarization Entangled Photon Pairs

Although highly nondegenerate sources have their application in space-based quantum communication and ultra-high-resolution quantum metrology, there are situations where it is preferable to have a degenerate source of polarization entangled photon pairs. Drone-based quantum key distribution or entanglement swapping would allow for re-configurable quantum networks near the surface of the Earth. For example, the Navy could use such drone-based links to send secure information between ships by flying the drones well above the turbulent air on the ocean's surface. By choosing a waveguide-based SPDC source with downconversion wavelengths $\lambda_i = \lambda_s = 808$ nm, entangled photons can be sent between drones without degrading the SWaP of the drone system. It is also quite convenient to produce downconversion photons at such wavelengths since a small diode-based laser can be used, as will be shown in this chapter. Additionally, 808-nm photons can be detected using Silicon APDs, which are small in size and low in weight and work at room temperature* (i.e., do not need to be cryogenically cooled). Downconversion wavelengths at 808 nm are also suitable for atmospheric transmission because shorter wavelengths diffract less through the atmosphere (than, e.g., telecom wavelengths), but also are outside of the Chappuis atmospheric absorption [50] that ranges from 400 to 650 nm (peaking at 575 and 603 nm). To realize this type of source, our collaborators at AdvR, Inc developed a nearly fully integrated source of degenerate photon pairs that are entangled in polarization, using an external 50:50 BS and post-selecting on coincidences. This source boasts a concurrence of 0.80 and a state purity of 0.81 without any external narrowband filtering nor temporal compensation; further improvements are expected.

---

*the detector modules can operate at room temperature; the APD's themselves are cooled with small thermoelectric coolers (TEC) to reduce the detector dark counts.

5.1 Experimental Setup

A pulse driver with a repetition rate of 10 MHz and pulse width of 2.5 ns drives a volume-holographic-grating (VHG)-stabilized diode. As will be discussed in Section 6, the settings of the pulse driver can be manipulated to improve the spectral purity (i.e., spectral unentanglement) of the source. The resulting 5 mW of pulsed light at 808 nm is collimated and then coupled into a polarization-maintaining (PM) fiber as shown in Figure 5.1. The pump light in this first PM fiber is then coupled directly into a second PM fiber using a fiber mating sleeve. This secondary fiber is pigtailed to a magnesium-doped lithium niobate ridge waveguide in which SHG occurs; this SHG process takes two of the 808-nm pump photons and combines them into a higher-energy daughter photon at 404 nm. The coupling efficiency of 808-nm and 404-nm light through the SHG waveguide was 54% and 33%, respectively [25]. Recalling back to Section 2.1, the SHG process is the opposite process of SPDC, but happens at a much higher rate (since there are many more 808-nm photon pair combinations) than the SPDC process thereby resulting in a bright photon beam at 404 nm. For this specific source, the peak SHG conversion efficiency is 46%/W [25], so we expect an output of (5 mW×0.46 = 2.3 mW); in practice we observed ≈ 7 μW of 404-nm pump light at the exit of the output PM fiber. The output of the SHG waveguide is pigtailed into an additional PM fiber. By tightly wrapping the SHG output fiber around a 1-cm post, the fiber can act as a spectral filter with transmission inversely proportional to the number of wraps. This is effective since the output fiber of the SHG module is single-mode for 404 nm (PM400 Fiber), thereby forcing most of the 808-nm mode into the fiber cladding, where it is easily removed via fiber mode-stripping[25]. Empirically, the sufficient number of wraps can be found simply by changing the temperature of the SHG crystal such that the necessary SHG phase-matching conditions are no longer met, i.e., there are no 404-nm photons being produced, and measuring the signal exiting the output fiber with respect to the number of wraps around the post.

Having sufficiently filtered the 808-nm pump, the output fiber guides the 404-nm SHG photons into a second PPLN waveguide where degenerate SPDC occurs ($404\,\text{nm} \rightarrow 808\,\text{nm}+ 808\,\text{nm}$). The 404-nm coupling efficiency through the SPDC module was 50% and 808-nm
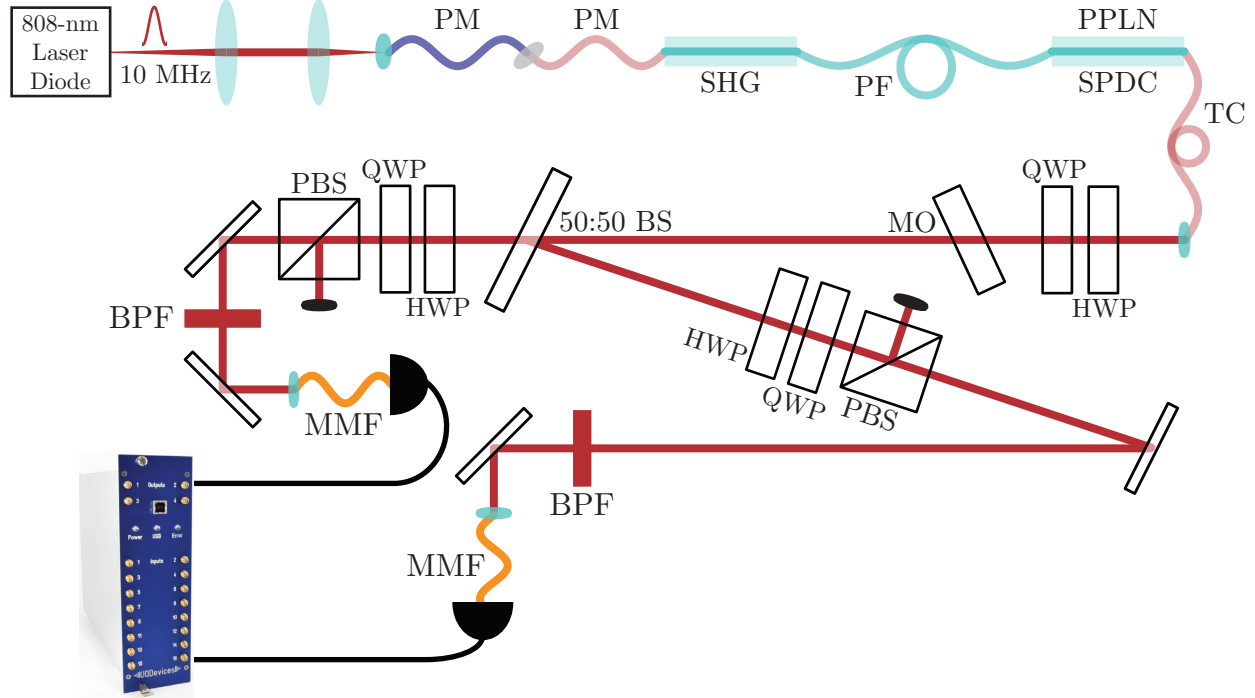
Figure 5.1: The experimental setup for the degenerate beamsplitter polarization-entanglement source. A 10 MHz pulsed laser at 808 nm is focused using two lenses into a polarization-maintaining (PM) fiber and then directly coupled (using a mating sleeve) into a PM fiber that acts as the input to the SHG crystal. The 808-nm photons then upconvert into 404-nm photons through the SHG process. The 808- and 404-nm photons are then guided into another PM fiber that is coiled around a 1 cm-diameter post, in order to filter out the 808-nm pump photons (pump-filter: PF). The 404-nm photons are then guided into the PPLN SPDC crystal where they downconvert into a pair of 808-nm photons. The resulting photons (404-nm SPDC pump and 808-nm downconversion photons) are then guided into a temporal compensator (TC), a final PM fiber that is cut to a length that will compensate for any group velocity walkoff in the SPDC PPLN.. The photons exiting the PM fiber are then launched into free space and collimated using an aspheric lens. Initial waveplates (HWP and QWP) are used to compensate any polarization transformation by the fiber with respect to the plane of the optical table and a tilted multi-order waveplate (MO) is used to correct any residual phase between H and V. Finally, the photons split evenly at the 50:50 beamsplitter (BS) and are sent through state tomography polarization optics and coupled into multi-mode fibers (MMF). The 404-nm upconversion photons are filtered out using bandpass filters (BPF - Semrock LL01-810-12.5 - $\Delta\lambda = 3.1$ nm) around 810-nm before the MMF. The filter is rotated around its vertical axis in order blue-shift the filter to be centered around 808 nm. The 808-nm SPDC photons are detected in coincidence, using two excelitas APD photon counters and a UQD timetagger.

out-coupling efficiency was 58% [25]. Using type-II phase-matching, the two-qubit polarization state produced is $|H_{808}V_{808}\rangle$, which is not yet a two-qubit polarization-entangled state[†]. The downconversion photons are then guided into the PPLN output pigtailed PM fiber which is nominally cut to a length that fully compensates for any group velocity walkoff within the PPLN (≈ 65 cm), alleviating any need for additional external temporal compensation (see Section 5.2 for further explanation).

The resulting (404-nm pump and 808-nm downconversion) photons are then collimated and launched into free-space using an aspheric lens with an 11-mm focal length coated for 800-nm light. A HWP and QWP are used to compensate for any unitary polarization rotation caused by the fiber system and a tiltable multi-order waveplate is used to test the necessity of any external temporal compensation (See Section 5.2). Once these adjustments are made, a 50:50 BS splits the photons equally along two paths, reflected $|r\rangle$ and transmitted $|t\rangle$, which results in the following state transformation:

$$
\begin{aligned}
|H\rangle \otimes |V\rangle &\to \frac{1}{\sqrt{2}}(|t\rangle_H + i|r\rangle_H) \otimes \frac{1}{\sqrt{2}}(|t\rangle_V + i|r\rangle_V) \\
&\to \frac{1}{2}(|t\rangle_H|t\rangle_V + i|t\rangle_H|r\rangle_V + i|r\rangle_H|t\rangle_V - |r\rangle_H|r\rangle_V,
\end{aligned} \tag{5.1}
$$

where the i accounts for the $\pi/2$ phase shift on reflection off the 50:50 BS. Post-selecting on coincidences, i.e., scenarios where one photon reflects and the other transmits, we end up with the following (normalized) maximally entangled state:

$$
|\psi^+\rangle = \frac{1}{\sqrt{2}}(|t\rangle_H|r\rangle_V + |r\rangle_H|t\rangle_V) = \frac{1}{\sqrt{2}}(|H\rangle_t|V\rangle_r + |V\rangle_t|H\rangle_r) \tag{5.2}
$$

where the first qubit represents the photon detected in the transmitted port and the second qubit represents the photon detected in the reflected port[‡]. Once the photons are split into two paths, bandpass filters ($\Delta\lambda_{FWHM} = 20.2nm$; Semrock - FF01-810/10-25) are used to

---

[†]Here we omit the temporal part of the total wavefunction, which would indicate that an $|H\rangle$ photon exits the PPLN at a different time than its sister $|V\rangle$ photon.

[‡]Here we have implicitly assumed that the $|H\rangle$ and $|V\rangle$ photons exit the PPLN with the same wavelength, and exit the temporal compensation PM fiber at the same time.

block the 404-nm pump light and the downconversion photons are collected into multimode fibers and detected on Silicon APDs (Perkin-Elmer, $\eta \approx 60\%$). As with the nondegenerate sources, a state tomography as described in Section 3.2.1 is used to characterize the state produced by the entanglement source.

5.2   Results

To measure and optimize the entanglement quality of this source, state tomographies are performed with respect to various parameters, including SPDC temperature, laser temperature, and external temporal compensation. The entanglement visibility is also directly measured by setting the polarization of one path to D and rotating the polarization of the other path over 180°. The final concurrence, state purity, and fidelity are then calculated from the density matrix.

5.2.1   Optimizing the System Temperatures

Given the mechanics of this entanglement source, three temperatures are controlled within the system using thermoelectric coolers (TEC): the temperature of the pulsed laser diode, the temperature of the SHG crystal, and the temperature of the SPDC crystal. As will be shown, the SPDC temperature is the most critical for controlling the entanglement of the system. This is to be expected, as the SPDC temperature shifts the downconversion wavelengths away from degeneracy; in this case, the interfering processes at the 50:50 BS (H transmitted/V reflected, or V transmitted/H reflected) become distinguishable. The other two temperatures may affect the efficiency of the source by changing the mode of the pump laser light (if a higher-order mode is emitted, it will not couple into fiber as efficiently) and by changing the efficiency of the SHG process. As part of the source characterization the concurrence was measured with respect to both the SPDC temperature (Figure 5.2) and the laser temperature (Figure 5.3); the temperature dependencies are then plotted and fit to a parabola ($y = ax^2 + bx + c$), used to determine the optimum operating temperature.

For the data shown in Figure 5.2(a), the 808-nm laser temperature is held at 25.1 °C
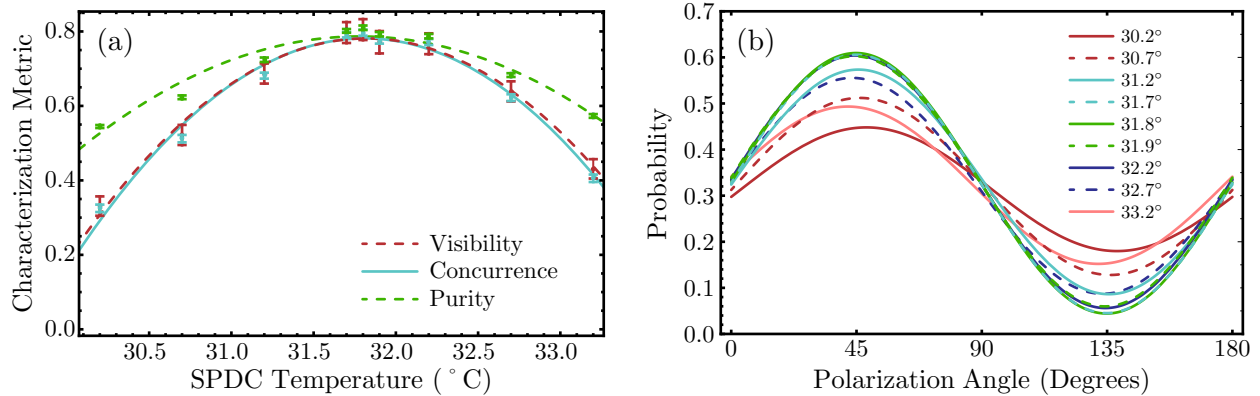
Figure 5.2: (a) The measured values and fitted parabolas of the max visibility, visibility, concurrence, and purity for varying SPDC temperatures. (b) The density matrix fringes from which the max visibility is calculated and represents the probability of getting a click (detecting a photon) when projecting the state onto $\Delta\theta$, which is the polarization angle between the two photons in a pair when $|D\rangle = \frac{1}{\sqrt{2}}(|H\rangle + |V\rangle)$ is projected onto one photon in the pair and an arbitrary linear polarization state is projected onto the other photon using the HWPs in the tomography setup. The equation, $P = \langle D|\langle\Delta\theta||\rho||D\rangle|\Delta\theta\rangle$ demonstrates this projection.

and the SPDC temperature is varied between 30.2 °C and 33.2 °C, as shown in Table 5.1. The concurrence, purity, and visibility have been previously defined; however, we now introduce a new parameter: max visibility. The max visibility accounts for any arbitrary unitary transformations that may appear within the source and measurement system, and recalculates the expected entanglement visibility directly from the density matrix. Figure 5.2(b) shows the fringes from which the max visibility is calculated and represents the probability of getting a click (detecting a photon) when projecting the state onto $\Delta\theta$, which is the polarization angle between the two photons in a pair when $|D\rangle = \frac{1}{\sqrt{2}}(|H\rangle + |V\rangle)$ is projected onto one photon in the pair and an arbitrary linear polarization state is projected onto the other photon using the HWPs in the tomography setup. The equation, $P = \langle D\Delta\theta||\rho||D\Delta\theta\rangle$ demonstrates this projection, where $|\rho|$ is the absolute value of the measured density matrix. The "max visibility" is then extracted as (max-min)/(max+min). From the parabolas fit to the data in Table 5.1, the optimal temperatures are measured to be 31.82±0.03 °C for the visibility, 31.79±0.05 °C for the purity, and 31.80±0.03 °C for the concurrence, which gives us an average optimal SPDC temperature of 31.807±0.004 °C.

The same measurement is then made except now the SPDC temperature is held at 31.8 °C while the laser diode temperature is varied. The resulting data is shown in Table 5.2 and

SPDC Temp (°C)	D/A Visibility	Conc	Purity
30.2	0.331±0.026	0.325±0.010	0.545±0.004
30.7	0.522±0.027	0.512±0.010	0.623±0.005
31.2	0.687±0.027	0.681±0.008	0.724±0.006
31.7	0.797±0.028	0.791±0.007	0.802±0.005
31.8	0.805±0.028	0.797±0.008	0.810±0.006
31.9	0.771±0.030	0.775±0.008	0.793±0.006
32.2	0.767±0.028	0.772±0.008	0.787±0.006
32.7	0.639±0.027	0.622±0.009	0.683±0.005
33.2	0.431±0.026	0.406±0.010	0.573±0.005

Table 5.1: Measured entanglement parameters with varying SPDC waveguide temperature and constant laser temperature (25.1 °C).

Laser Temp (°C)	D/A Visibility	Concurrence	Purity
21.1	0.791±0.029	0.786±0.009	0.802±0.007
23.1	0.768±0.029	0.765±0.008	0.785±0.006
25.1	0.805±0.028	0.797±0.008	0.810±0.006
27.1	0.769±0.029	0.768±0.008	0.788±0.006
29.1	0.777±0.031	0.762±0.008	0.784±0.006

Table 5.2: Measured entanglement parameters with constant SPDC temperature (31.8 °C) and varying 808-nm pump laser temperature.

is plotted in Figure 5.3. This data shows that the entanglement parameters remain fairly constant (varying no more than ±2.3% over a range of 8 °C) with a slight peak at 25.1 °C. All further measurements are made with the SPDC temperature at 31.8 °C and the laser diode temperature of 25.1 °C.

5.2.2 Verifying the System Temporal Compensation

The photons in the downconverted pair have orthogonal polarizations and therefore experience a certain amount of walk-off from each other due to the birefringence of the waveguide and of the output fiber, as discussed in Section 2.4. To compensate for this walk-off, our collaborators at AdvR use a technique that leverages the birefringence of the output PM fiber to undo the temporal walk-off caused by the crystal. This is done simply by orienting the eigenmodes of the fiber such that the fiber birefringence acts oppositely to the waveguide
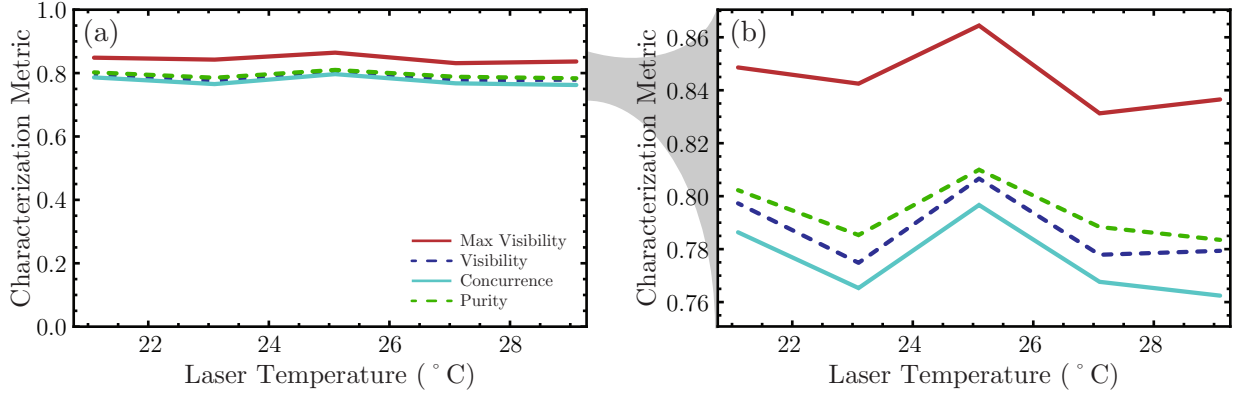
Figure 5.3: (a) The measured values of the max visibility, visibility, concurrence, and purity for varying laser diode temperatures. (b) A zoomed-in plot of (a). The four parameters remain fairly constant over 8 °C variation in laser temperature.

birefringence, and then choosing the correct length of fiber [25]. AdvR measures the amount of temporal compensation necessary by using an external Michelson interferometer with a beamsplitter measurement on the output, and adjusting the path length of one arm until a coincidence minimum is measured. Through this technique, AdvR found that the net amount of temporal walk-off caused by the crystal plus one meter of PM fiber was 0.75 ps. Accounting for the group-velocity walkoff in the PM fiber of 2.1 ps/m, they they shortened the fiber by 35 cm in order for the photons to leave the fiber system with nominally zero walk-off.

To verify the accuracy of this method, additional temporal compensation was added before the 50:50 BS using calcite and quartz crystals[§] with the fast axis in the vertical or horizontal positions. Positive thickness indicates the fast axis is in the horizontal position; "Negative" thickness indicates the fast axis is in the vertical position. The results are shown in Table 5.3 and plotted in Figure 5.4. The same calculations were done as when optimizing the SPDC temperature, and the resulting optimal temporal compensation widths were found to be 0.079±0.053 mm for the visibility, 0.042±0.078 mm for the purity, and 0.077±0.053 mm for the concurrence, which gives us an average optimal external compensation width of only 0.071±0.012 mm (0.036 ps). Given that the walk-off induced in the PPLN waveguide of the

---

[§]The plot in Figure 5.4 features an x-axis labeled as "calcite thickness." It is important to note that an additional quartz multi-order waveplate was used to measure the -0.05 and 0.05 mm data points; however, the equivalent calcite thickness was calculated based off the estimated quartz thickness used.

Calcite Thickness (mm)	D/A Visibility	Concurrence	Purity
-1.0	0.171±0.027	0.166±0.012	0.501±0.003
-0.5	0.490±0.030	0.483±0.011	0.609±0.006
-0.05	0.719±0.035	0.761±0.011	0.786±0.008
0	0.805±0.028	0.797±0.008	0.810±0.006
0.05	0.742±0.036	0.738±0.009	0.768±0.007
0.5	0.524±0.030	0.520±0.010	0.626±0.006
1.0	0.340±0.028	0.334±0.011	0.545±0.004

Table 5.3: Entanglement parameters with varying temporal compensation thickness at 31.8 ° SPDC temperature and 25.1 ° laser temperature.
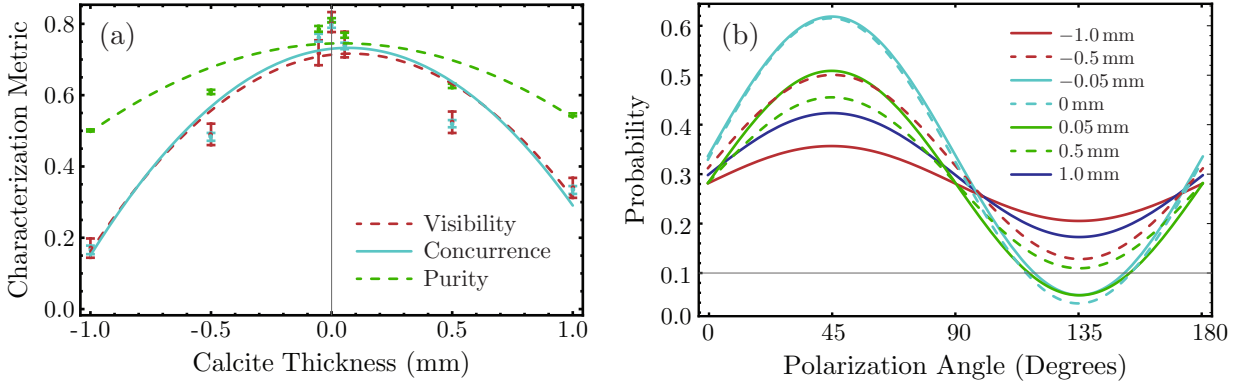
Figure 5.4: (a) The measured values and fitted parabolas of the max visibility, visibility, concurrence, and purity for varying Temporal Compensation. (b) The density matrix fringes from which the max visibility is calculated and represents the probability of getting a click (detecting a photon) when projecting the state onto $\Delta\theta$, which is the polarization angle between the two photons in a pair when $|D\rangle = \frac{1}{\sqrt{2}}(|H\rangle + |V\rangle)$ is projected onto one photon in the pair and an arbitrary linear polarization state is projected onto the other photon using the HWPs in the tomography setup. The equation, $P = \langle D\Delta\theta||\rho||D\Delta\theta\rangle$ demonstrates this projection.

source is estimated to be 0.75 ps, AdvR was able to compensate their system using their fiber method within 5% of perfect compensation.

5.2.3 Optimized Entanglement Measurements

Once the various parameters were optimized, a final state tomography was performed, yielding the density matrix shown in Figure 5.5(b), to be compared with the theoretical expected density matrix in Figure 5.5(a). We found that the output state of the integrated system was slightly rotated and so a QWP and HWP were placed in the beam path before the 50:50
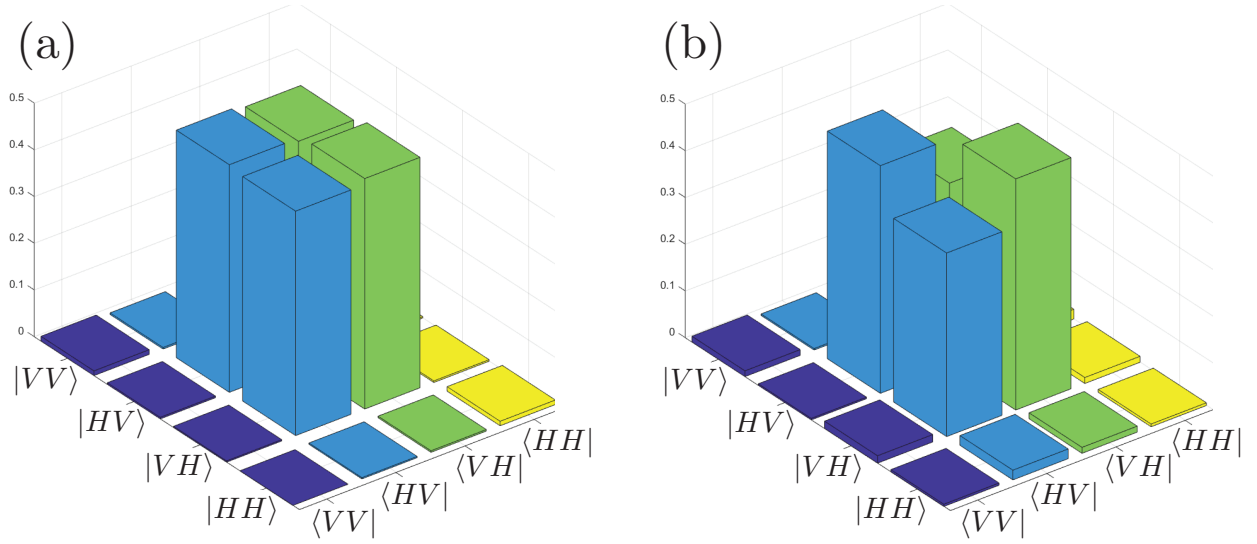
Figure 5.5: (a) The theoretical state tomography for the two-qubit state: $|\psi^+\rangle = \frac{1}{\sqrt{2}}(|HV\rangle + |VH\rangle)$. (b) The measured state tomography for AdvR's degenerate beamsplitter polarization-entanglement source. The calculated fidelity between these two states is $F = 0.90$.

BS to correct for the rotation. The addition of the QWP did decrease the concurrence and purity slightly ($C = 0.797 \pm 0.008$ and $\gamma = 0.810 \pm 0.006$ versus $C_{rot} = 0.771 \pm 0.010$ and $\gamma_{rot} = 0.793 \pm 0.008$, however, the state fidelity increased from $F = 0.88$ to $F_{rot} = 0.90$.

Finally, a direct measurement of the D/A visibility was made by setting the polarization in one arm of the tomography polarization optics to $\langle D| = \frac{1}{\sqrt{2}}(\langle H| + \langle V|)$ and measuring the coincidences for different angles of the HWP in the other arm of the tomography polarization optics. The results are shown in Figure 5.6 along with the calculated curve from the density matrix (using the same method as in Figure 5.2(b) and Figure 5.4(b)). These results show clear fringes with a visibility of 0.77 ± 0.03.
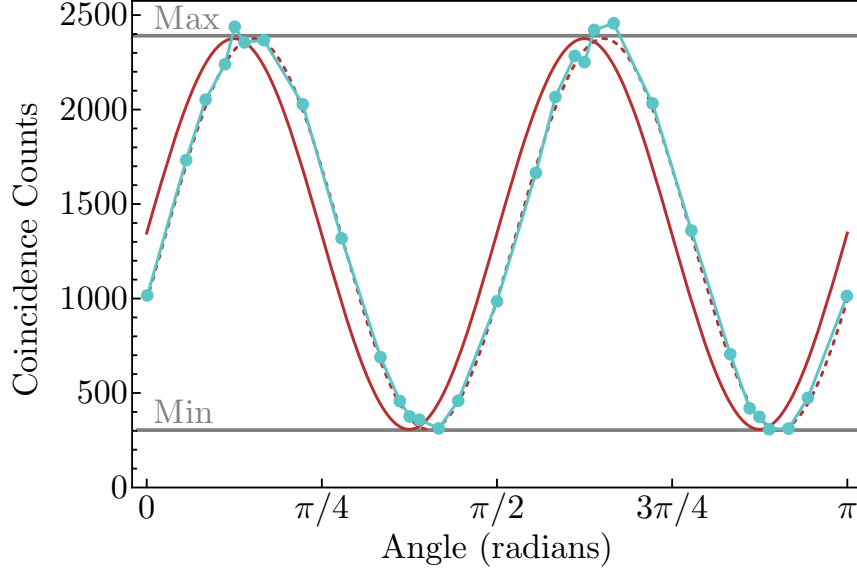
Figure 5.6: Coincidence Counts per Half Waveplate Angle. The blue curve represents measured values. The red curve shows the calculated visibility fringes from the measured density matrix. The red dotted curve shows the calculated visibility fringes from the measured density matrix with a 5° polarization shift to match the blue curve.

5.3 Conclusion

Through these measurements of the degenerate waveguide-based polarization-entanglement source developed by AdvR, we find an optimized maximum concurrence of $C = 0.797 \pm 0.008$, state purity of $\gamma = 0.810 \pm 0.006$, and state fidelity of 0.90, with a corresponding maximum entanglement visibility of 0.864. We also observed that the original temporal compensation implemented by AdvR was very nearly optimal; moreover, our results indicate that there is no compensation correction that would significantly increase the source quality (i.e., concurrence). We conclude, then, that the most likely underlying cause for imperfect entanglement is a lack of symmetry in the energy spectra of the SPDC downconversion photons, e.g., the spectra look trapezoidal[¶]. One way to test this will be to apply a narrowband spectral filter to one of the SPDC photons; this should recover near perfect concurrence unless there is some other underlying mechanism that is causing the H and V photons to be distinguishable. A home-built tunable narrowband grating-based filter is currently being built as a proof-of-concept before purchasing a custom bandpass filter.

[¶]Note that unlike the nondegenerate source, here we do not have the option of using stimulated downconversion to measure the spectrum, as there would be no easy way to filter out the seed laser.

Chapter 6

Conclusion

We have experimentally demonstrated the first-ever (to our knowledge) highly nondegenerate source of polarization-entangled photon pairs in a waveguide with an accidental-corrected state fidelity of $F = 0.986$, concurrence of $C = 0.983 \pm 0.004$, and purity of $\gamma = 0.990 \pm 0.005$. These metrics are suitable for the aforementioned quantum information and metrology protocols and present great progress towards creating integrated photonic sources with optimal SWaP for mobile quantum networks. Further work can be done to improve the source entanglement by better-matching the process spectra and by lowering the occurrence of accidental coincidences. Additionally, by alleviating the need for narrowband filtering through spectral matching, we can vastly improve the brightness of the source (current brightness is ≈ 450 pairs/s/mW). An interferometer-based attosecond-resolution metrology experiment that requires a highly nondegenerate source of polarization-entangled photon pairs was introduced as a possible application for this waveguide source. We have demonstrated the dual-frequency capabilities of the interferometer with 1550-nm and 810-nm interference fringe visibility of $\approx 98\%$ and $\approx 79\%$, respectively.

We have also demonstrated a waveguide-based degenerate source for drone-based entanglement distribution with accidental-corrected state fidelity of $F = 0.90$, concurrence of $C = 0.797 \pm 0.008$, and purity of $\gamma = 0.810 \pm 0.006$. Although these metrics are below the requirements for use in drone-based quantum information protocols, we are confident that through narrowband filtering of the spectra using a home-built grating-based filter ($\Delta\lambda \approx 0.1 - 0.2$ nm), the resulting metrics will be sufficient. This source is an important step in mobile quantum networks due to its fiber-based temporal compensation and nearly fully integrated design.

Appendix A

Beam-Displacer-Based Source of Polarization-Entangled Photon Pairs

Developing a usable source of highly nondegenerate polarization-entangled photon pairs that boasts high state fidelity and brightness without the need for external temporal compensation, narrowband spectral filtering, and active stabilization would be enabling for multiple applications, e.g., quantum networking, space-based quantum communication, and even quantum metrology, as we discuss in Chapter 4. Thus far, an optimal source has yet to be found; however, various source designs have been proposed and now implemented that meet at least one of the aforementioned specifications. We have already discussed the waveguide source that has the potential to surpass bulk optics both in brightness and portability. Now, we will discuss both a beam-displacer-based source of polarization-entangled photon pairs. This source design is quite costly in terms of number of bulk components needed; however, the expected brightness is on par with waveguide sources without the need for temporal compensation. Furthermore, the beam displacer source has already given results with high entanglement fidelity, albeit in an unstable configuration.

Polarization-entangled sources based on beam displacers to pump two adjacent sections of a single crystal have been shown to enable record-high heralding efficiency; because of this, one such source was used in the recent National Institute of Standards and Technology (NIST) experiment that definitively showed a loophole-free violation of Bell's inequality [51]. However, that implementation produced degenerate pairs of photons at 1550 nm. To our knowledge, no one has reported on a non-degenerate source of polarization-entangled photons until now. And as discussed below, the new source actually employs a pair of crystals, which reduces the number of waveplates needed. The expected advantages of the beam displacer source developed by our collaborators at Oak Ridge National Laboratory (ORNL)*

---

*This source was commissioned as part of our Phase 2 NASA project to use hyper-entangled (polarization and time bin) nondegenerate photons to demonstrate superdense teleportation [8]. It was designed, constructed, and initially characterized by ORNL collaborators, Nick Peters and Brian Williams.
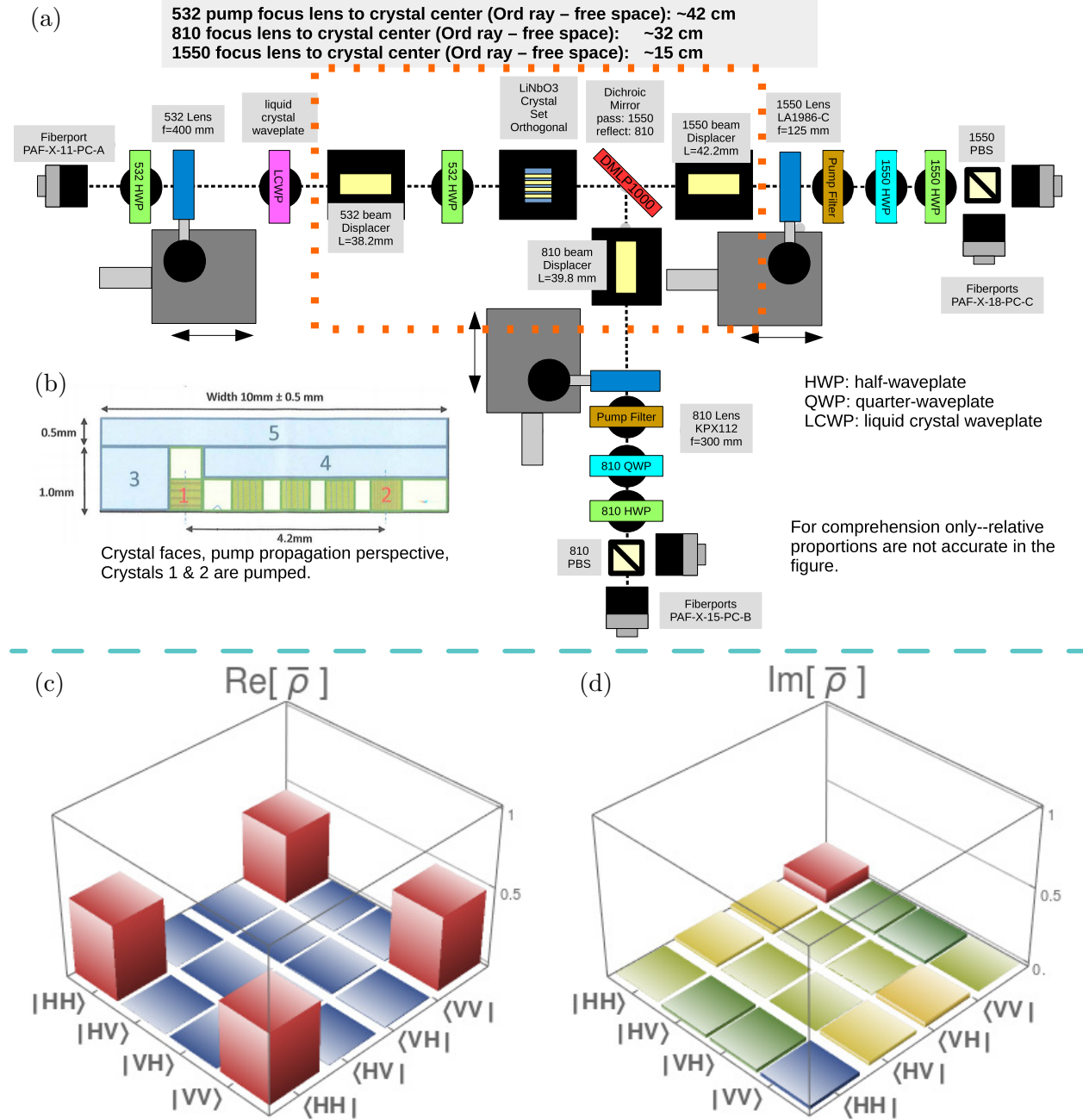
Figure A.1: (a) The proof of concept results from our collaborators at Oak Ridge National Laboratory. For their results, tweakers were used to optimize beam separation to better match the crystal separation. Later, new beam displacers were placed in the setup in an attempt to better match the crystal separation without the use of tweakers. This modified source is the one that we are currently characterizing at UIUC. (b) The design of the Covesion downconversion crystal. The two crystals used to create the two processes are labeled with 1 and 2. The white spaces in these crystals represent non-poled areas. The crystals labeled 3-5 are used as spacers for a snug fit within the crystal oven mount. (c) The real part of the measured density matrix. (d) the imaginary part of the measured density matrix.

[52] include high brightness and robustness against group velocity walk-off. Our ORNL collaborators demonstrated a proof-of-concept of this source for the desired wavelengths (810 nm and 1550 nm) (see Figure A.1); however, optimization of the entanglement fidelity required use of inherently unstable "tweakers" (i.e. pieces of glass) for adjustment within the source. To rid the source of instability, new source components were designed and implemented and the untested source was sent to our group for full characterization. The proof-of-concept achieved a state fidelity of $F = 0.955 \pm 0.001$ with the maximally entangled $|\phi^+\rangle$, state purity of 0.937 ± 0.001, a brightness of 1M pairs/s per mW of pump power, and a heralding efficiency of 0.23 (although they estimate a maximum of heralding effiency of 0.81). The characterization of the current version is still in progress; however, we have seen some evidence of sufficient brightness ($\approx 10^4$ pairs/s per mW) and are able to pump both entanglement processes, albeit not concurrently. We believe the current issue with the source is the new components chosen by ORNL over-compensated for the lack of tweakers. We expect to measure high-fidelity entanglement once further adjustments are made. The remaining discussion of this source will pertain to the current version and our efforts here at UIUC.

A frequency-doubled (1064 nm + 1064 nm $\to$ 532 nm) pulsed laser (rep rate = 80 MHz) is coupled into a 20-m single-mode fiber and launched into the source system using a fiber port (PAF-X-11-PC-A, f=11.0 mm) provided to us by ORNL (Figure A.2). This fiber port collimates the 532-nm pump beam in a beam waist of 1.80 mm. The pump beam then travels through a HWP (WPH05M-532) and QWP (WPQ05M-532), which rotate the pump polarization preferentially[‡] to horizontal (H) polarization. The resulting light travels through a PBS which puts the light into a definite H polarization state by ideally reflecting all light that is not horizontally polarized. The now horizontally polarized pump beam transmits through an additional HWP that rotates its polarization to diagonal (D) polarization (an equal combination of H and vertical (V) polarization); the beam then goes through a lens (f= 533 mm - verified via direct measurement and imaging techniques) on a translation stage for eventually focusing into the SPDC crystals. The translation stage is for optimizing

---

[‡]The light from the laser may be slightly unpolarized, thus it may be impossible to rotate all the light to horizontal polarization.
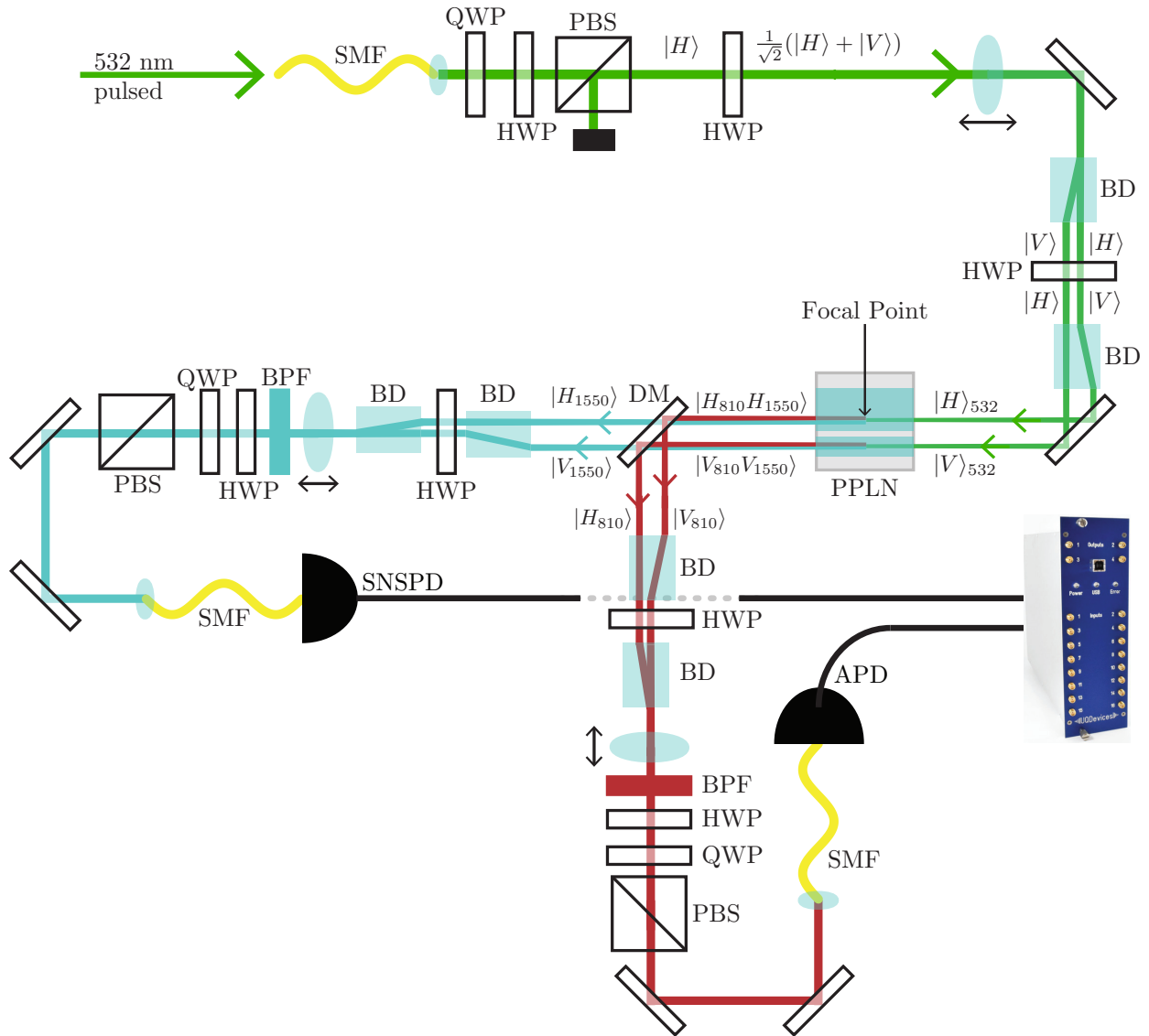
Figure A.2: Experimental Setup for the ORNL Source of Polarization-Entangled Photon Pairs. SMF - single-mode fiber, QWP - quarter waveplate, HWP - half waveplate, PBS - polarizing beamsplitter, BD - beam displacer, PPLN - periodically poled lithium niobate downconversion crystals, DM - dichroic mirror, BPF - bandpass filters, SNSPD - superconducting nanowire photodetectors, APD - avalanche photodiode. A pulsed 532-nm laser is diagonally polarized and focused using a f= 533 mm lens. The path is then separated into two beam paths based on polarization (horizontal polarization in one path and vertical in the other) using a BD - HWP - BD set of optics. The separated beams then pump two individual PPLN crystals (type-0 phase-matching) rotated at 90° with respect to each other to produce pairs of photons with equal polarization ($|H_{810}H_{1550}\rangle$ and $|V_{810}V_{1550}\rangle$). The downconversion photons are then split by wavelength on a DM and the same-wavelength beams are recombined on their respective BD-HWP-BD paths[†]. A removable HWP-QWP-PBS set can be used for performing quantum state tomographies. The downconversion photons are then coupled into SMF and detected on APDs (810 nm) or SNSPDs (1550 nm) depending on their wavelength.

the focal point with respect to the midpoint of the downconversion crystals (accounting for the crystal refractive index) which should maximize the source heralding efficiency. After the lens, the beam reflects off a mirror and is sent through a set of calcite beam displacers (BD, dimensions given in Figure A.1) and a HWP. The diagonally polarized pump light is split into two beams by polarization; the horizontally polarized component of the beam transmits directly through the beam displacer, whereas the vertically polarized component deflects at an angle $\approx 6°$. Now, there are two beams (one H-polarized and one V-polarized) that transmit through a HWP@45° that rotates the beams' polarizations by 90° ($H \rightarrow V$ and $V \rightarrow H$). The two beams now travel through a second beam displacer, which further increases the separation between the two beams[§]. Since the beam that was originally V-polarized is now H-polarized, it will transmit through the beam displacer undeflected. The beam that was originally H-polarized, however, will now deflect further away (again by $\approx 6.3°$) from the other beam within the beam displacer due to the polarization rotation from the HWP. After the set of beam displacers, we measured the beam separation to be ≈ 4.7 mm by imaging the two beams onto a standard ruler.

The separated, focusing, polarized pump beams now reflect off a second mirror into the downconversion crystals (the original crystal configuration is shown in Figure A.1(b)), which are mounted inside of a TEC temperature controller oven and heated to 123° C. The TEC oven is mounted on a 6-axis stage for optimizing the downconversion efficiency. The SPDC crystals use type-0 phase-matching to downconvert the H (V) polarized pump beam to a pair of H (V) polarized downconversion photons at 810 nm and 1550 nm. The resulting maximally entangled state is thus $|\phi^+\rangle = \frac{1}{\sqrt{2}}(|H_{810}H_{1550}\rangle + |V_{810}V_{1550}\rangle)$[¶]. The SPDC chip for one of the entanglement processes is a MgO-doped PPLN crystal optimized for a 515 nm pump with nine 0.5-mm-wide grating areas with poling periods ranging from 6.00 to 8.36 μm, each supporting the creation of downconversion pairs that may or may not be efficiently produced at the desired wavelengths (more on this later). Each grating

---

[§]The reason for which two beam displacers are used instead of one longer one is so that both beams experience the same path length and ideally arrive at the crystal simultaneously. If only one long beam displacer was used, then the vertical (deflected) photons would have a longer path length.

[¶]Note that we are not concerned with what maximally entangled state is produced since we can easily switch between the four maximally entangled states using local operations (waveplates).

is separated by 0.2-mm-wide of unpoled crystal. The crystal chip is AR-coated to $R < 1\%$ at 515 nm and $R < 1.6\%$ at 650-1030 nm for both the input and output. The chip for the other process is an identical crystal with only a single grating section with a poling period of 7.40 μm; however, it is rotated by 90° (about the beam propagation axis) such that the angle between the input polarization and optic axis of the crystal is the same for both processes. This last point holds great importance for this source scheme; since each beam has its polarization at the same angle with respect to the optic axis, the photons of the same wavelength will experience the same velocity within the crystal and as such there should not be group-velocity walk-off between same-color photons. This source design thus alleviates any need for temporal compensation (disregarding any tuning required to compensate for imperfections in the crystals or beam path lengths), greatly simplifying the optimization parameters (i.e., temporal compensation, spectral overlap, modal overlap, etc.) for the source.

Assuming the beam separation matches the separation between the single crystal (#1 in Figure A.1(b)) and the grating area of the second crystal (#2 in Figure A.1(b)) that most efficiently produces downconversion photons at 810 and 1550 nm, both downconversion processes ($|H_{810}H_{1550}\rangle$ and $|V_{810}V_{1550}\rangle$) will be produced concurrently. The resulting 810 (1550) nm downconversion photons then reflect (transmit) off a longpass dichroic mirror (DMLP950) with cutoff wavelength of 950 nm. The remaining pump beam also reflects of the dichroic mirror. Now there are four beam paths (spatial modes) separated by wavelength and polarization: $|H_{810}\rangle$, $|V_{810}\rangle$, $|H_{1550}\rangle$, and $|V_{1550}\rangle$. The $|H_{810}\rangle$ beam transmits undeflected through a BD and a HWP that rotates its polarization to V_{810}. It then travels through a second BD that deflects it at $\approx 6°$. The $|V_{810}\rangle$ deflects through the first BD at $\approx 6°$, at which point its polarization is rotated to H_{810} by the HWP. It then travels undeflected through the 2nd BD. The BDs are cut to a length such that on exit of the second BD, the H_{810} and V_{810} spatial modes should overlap completely; see Figure A.1(a) for all nominal crystal lengths. The two 1550-nm beam paths go through the same process after transmitting through the DM, however, the BDs in the 1550-nm path are cut to a length such that on exit of the second BD, the two 1550-nm spatial modes are completely overlapped. Both the 810-nm and 1550-nm beams are collimated using plano-convex lenses on translation stages
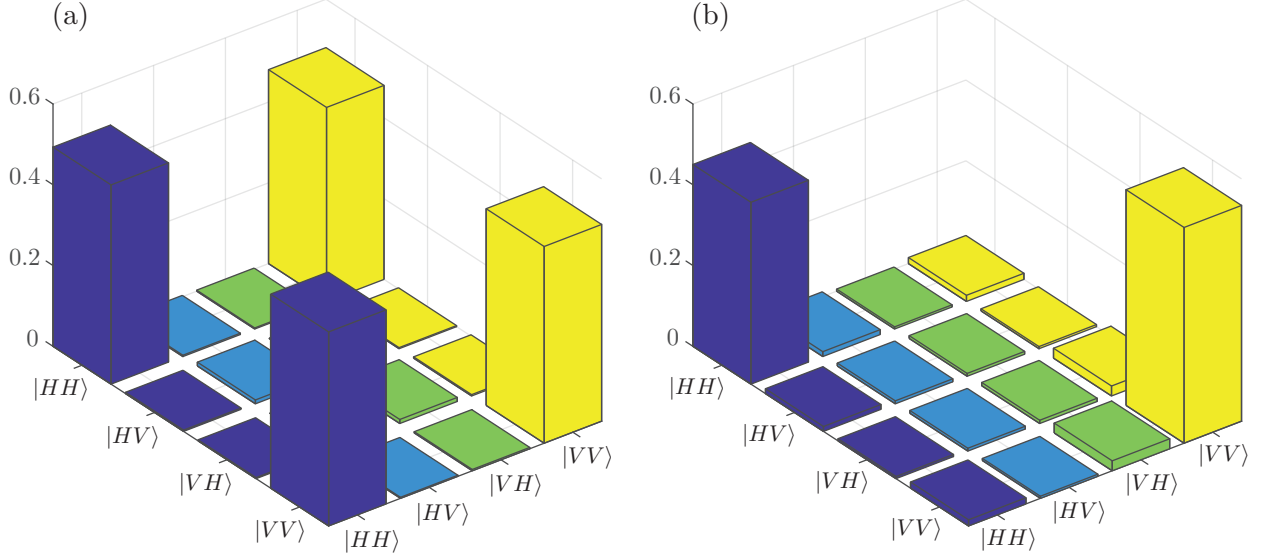
Figure A.3: (a) The theoretical density matrix for the maximally entangled $|\phi^+\rangle$. (b) The absolute value of the measured density matrix from the ORNL beam-displacer source. The corresponding concurrence is $C = 0.016$ and the purity is $\gamma = 0.49$.

with focal lengths f= 300 mm (Newport - KPX112) and f= 125 mm (Thorlabs - LA1986-C), respectively. Bandpass and longpass filters are also placed in the beam path to filter out any pump light and to increase the coherence length of the downconversion photons. A bandpass filter with a FWHM $\Delta\lambda = 10$ nm (Semrock - NIR01-1550/3-25) and a longpass filter with a cut-off wavelength of 715 nm (Thorlabs - FGL715M) are placed in the 1550-nm beam path. For the 810-nm path, a bandpass filter with a FWHM $\Delta\lambda = 20.2$ nm (Semrock - FF01-810/10-25) and the same longpass filter (FGL715M) are used.

At this point, the photons are in the same configuration as with the waveguide-based source from Chapter 3: H_{810} and V_{810} in one spatial mode and H_{1550} and V_{1550} in a separate spatial mode from the 810 photons; however, due to the design of the SPDC crystal set, these photons are also temporally overlapped, i.e. there is no need for temporal compensation. As such, the photons are coupled into their respective single-mode fibers and detected on their respective detectors (the 810 nm photons on APDs (Excelitas) and the 1550 nm photons on SNSPDs) and counted in coincidence. A removable HWP, QWP, and PBS can be placed in each downconversion beam path for performing a quantum state tomography to measure the density matrix of the resulting entanglement state, as was done with the waveguide-based source.

As of now, we can efficiently pump both processes, albeit not concurrently. We can pump both processes at the same time to balance the two polarization processes, at the loss of actual efficiency and without polarization entanglement because the spatial modes of the two processes do not perfectly overlap. Figure A.3 shows the measured state tomography when the crystal is set such that both processes are pumped inefficiently (i.e., we position the crystals such that each beam is slightly hitting its respective crystal - ideally the entire beam would be incident on the crystal). The resulting measured concurrence is $C = 0.016$ and purity is $\gamma = 0.49$, which are both insufficient for any application needing polarization-entangled photons. Since ORNL has already demonstrated polarization entanglement from a similar source, we are confident that the limiting factor is the source's ability to pump both processes efficiently and at the same time. To overcome this obstacle we have directly measured the difference between the crystal separation and the beam separation by diagonally polarizing the pump and translating the crystal perpendicularly to the beam paths while measuring the micrometer reading between the peaks in coincidence counts. With this measurement, we found the beam separation due to the BDs ($\approx$4.7 mm) was 0.36 mm wider than the crystal separation. Given that the crystals are only 0.5 mm wide, this discrepancy makes it impossible to efficiently pump both crystals with the pump beam going straight through the center of both crystals at the same time. We are currently working with the in-house UIUC Physics Department machine shop to make spacers to place between the crystals to increase their separation. Unfortunately, we have found this method quite unstable, since in order to keep the crystals from shifting within the oven, the spacer must be snug in the mount. However, since the spacers from the machine shop are metal and not necessarily adequately polished, we risk cracking the crystals if there is too much pressure on them from the spacers. Thus, an alternate option would be to order a completely new set of crystals where one of the crystals is much wider. This wide crystal would allow for greater flexibility in the spacing between the two crystals since the beam can be slightly off-centered without risking any beam clipping or unknown edge effects.

Appendix B

Home-Built Grating Spectrometer for Narrowband Filtering

For applications that require narrowband filter where one cannot measure the spectrum, it is advantageous to use a tunable filter in order to locate the ideal central wavelength of the filter before purchasing an expensive custom filter. Store-bought tunable filters can be either prohibitively expensive or inaccessible. One way to get around this issue is to build a grating-based tunable filter with filter bandwidths determined by the widths of the slits used and the grating density (the higher the density, the higher the resolution). To accomplish this narrowband filtering, the beam is focused into a 10-μm slit, which, in addition to a spherical mirror, acts as a beam expander, expanding the beam to the appropriate width for the required resolution (Figure B.1). The beam then diffracts off the grating (1200 grooves/mm) in different spatial modes depending on the wavelength of the light. The separate beams are then focused using a secondary spherical mirror into a 25-μm slit, positioned to transmit only one spatial mode corresponding to a narrowband frequency mode of the beam. The light that travels through the slit is then collimated and collected into a multimode fiber for detection. For modeling design parameters, see [53]. The example shown in Figure B.1 results in a filter bandwidth of $\Delta\lambda \sim 0.1 - 0.2$ nm at a central wavelength of 810 nm.
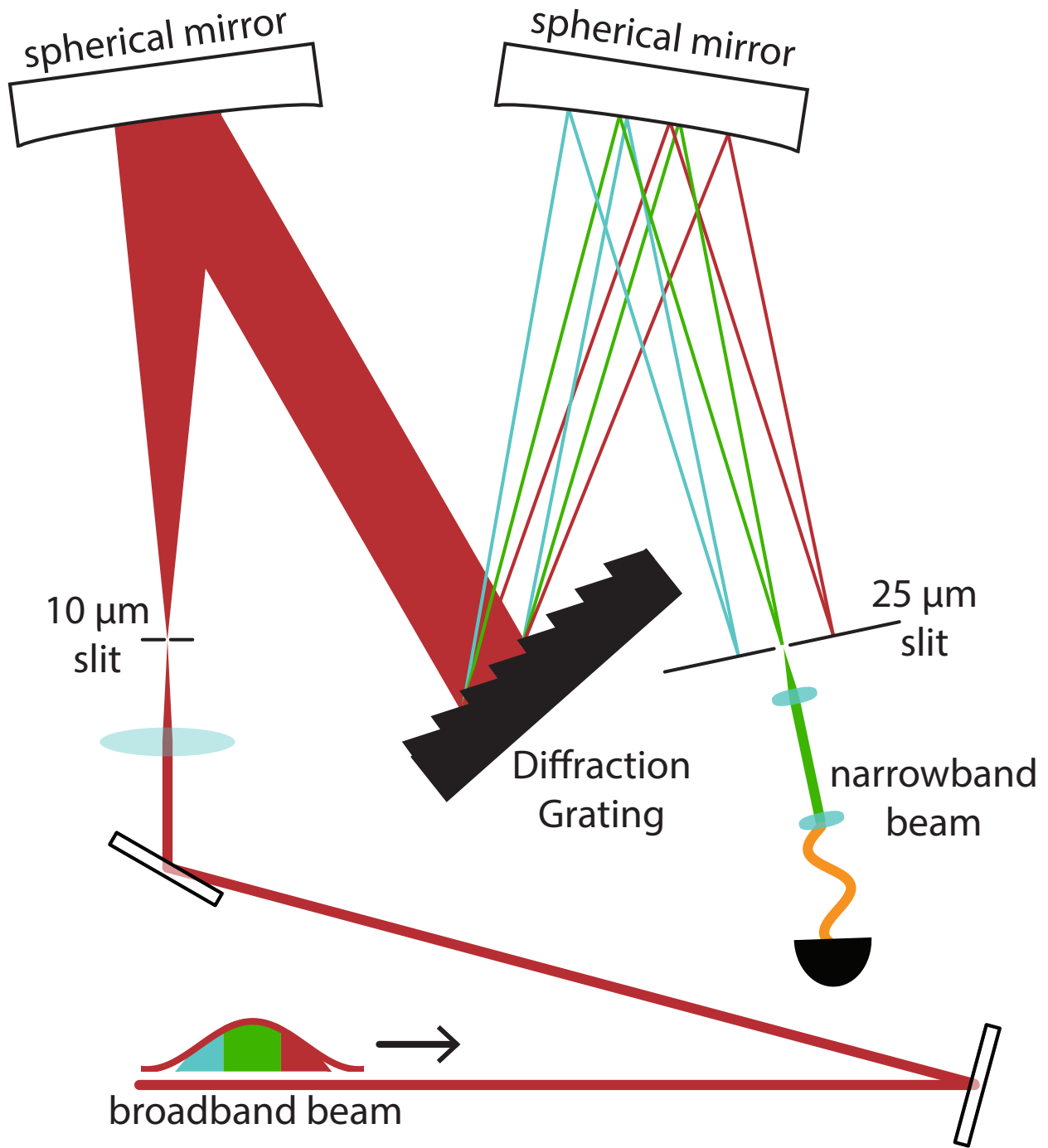
Figure B.1: Homebuilt Grating Spectrometer for Narrowband Filtering: the diffraction grating used in this example is a reflective ruled diffraction grating with a groove density of 1200 grooves/mm, a blaze angle of 26.73°, and blaze wavelength of 750 nm from Edmund Optics. The resulting filter bandwidth is $\Delta\lambda \sim$0.1-0.2 nm at a central wavelength of 810 nm.

Appendix C

Relevant Mathworks MATLAB Code

Included in this appendix are relevant Mathworks MATLAB codes for the projects included in this dissertation. A few of these codes are for automating processes that could be done by hand to make it easier on the researcher, e.g., an automated tomography code (tomo_auto) that rotates the waveplates in Thorlabs PRM1Z8 motorized precision rotation mounts and outputs a .csv file with the resulting singles, coincidences, and accidentals for analysis in our maximum likelihood estimation code. Also included is a code for automating the stimulated downconversion spectral measurements (spec_auto), which reads/writes from the Agilent Lightwave Measurement System that controls the tunable 1550-nm laser module used in those measurements. Spec_auto begins by initializing a GPIB connection to the Laser controller and then uses a "for loop" to iteratively measuring the 810 singles counts with respect to the laser wavelength read off of the laser module and records the data into a spreadsheet for analysis. The code ends by disconnecting the laser module. Finally, a code for calculating the temporal compensation of the consecutively poled highly nondegenerate waveguide source is shown. For this source geometry, the pump wavepacket downconverts, on average, in the middle of each half of the crystal, at times that account for the propagation time of the pump through the crystal. In the code, it is assumed that calcite is used to compensate for group velocity walk-off. The temporal compensation code begins by reading the wavelength- and polarization-dependent index of refraction values from a spreadsheet provided by AdvR. It then uses these values to calculate the group velocity for each wavelength and polarization combination (H_{532}, V_{810}, H_{810}, H_{1550}, V_{1550}). It then uses the calculated group velocities and input length values to calculate the different in exit times between same-color photons. Finally, the code converts the difference in exit times into a calcite width. The codes are color-coded based off the color notation used in MATLAB, however, it is important to note the green-colored comments that help the reader better understand the code.

```matlab
function tomo_auto(filename,outname,delay,counttime,fig)
begintime = clock;

%% Start up...
%% Do not if another APT window is open! A pop up window is
programmed as a reminder.
button = questdlg('About to launch the APT window -
                              do not run if another APT window is open.
                              Do you want to open the APT window?', ...
                  'Launch APT window', 'Yes', 'No', 'No');
if isempty(button)
      return
elseif length(button) == 2
      return
end

%% Create MATLAB Container for APT ActiveX Controller

fpos    = get(0,'DefaultFigurePosition'); % figure position
fpos(3) = 650; % figure window size; Width
fpos(4) = 450; % Height

fahwp = figure('Position', fpos,...
            'Menu','None',...
            'Name','APT GUI'); %810 HWP Controller
faqwp = figure('Position', fpos,...
            'Menu','None',...
            'Name','APT GUI'); %810 QWP Controller
fbhwp = figure('Position', fpos,...
            'Menu','None',...
            'Name','APT GUI'); %1550 HWP Controller
fbqwp = figure('Position', fpos,...
            'Menu','None',...
            'Name','APT GUI'); %1550 QWP Controller

%% Create APT ActiveX Controller

ahwp = actxcontrol('MGMOTOR.MGMotorCtrl.1',...
      [20 20 600 400 ], fahwp); %810 HWP Controller
aqwp = actxcontrol('MGMOTOR.MGMotorCtrl.1',...
      [20 20 600 400 ], faqwp); %810 QWP Controller
bhwp = actxcontrol('MGMOTOR.MGMotorCtrl.1',...
      [20 20 600 400 ], fbhwp); %1550 HWP Controller
bqwp = actxcontrol('MGMOTOR.MGMotorCtrl.1',...
      [20 20 600 400 ], fbqwp); %1550 QWP Controller
```

Figure C.1: MATLAB Code for Automating Tomography Measurement (Part 1). This function controls the waveplates for the different polarization settings, records the data into a .csv file, and outputs the most likely density matrix to fit the data using maximum likelihood estimation. This portion of the code sets up the frames for the APT ActiveX automatic waveplate controllers.

```matlab
%% Open all APT windows and set parameters and home

timeout = 180; % timeout for waiting for homing to finish

tomoSetup_aqwp(aqwp); % Setup the 810 QWP
tomoSetup_ahwp(ahwp); % Setup the 810 HWP
tomoSetup_bqwp(bqwp); % Setup the 1550 QWP
tomoSetup_bhwp(bhwp); % Setup the 1550 HWP

% First 0 is the channel ID (channel 1)
% Second 0 is to move immediately

aqwp.MoveHome(0,0); % Home the 810 QWP
ahwp.MoveHome(0,0); % Home the 810 HWP
bqwp.MoveHome(0,0); % Home the 1550 QWP
bhwp.MoveHome(0,0); % Home the 1550 HWP

%% Wait while the WPs move; timeout to avoid dead loop

t1 = clock;
while(etime(clock,t1)<timeout)
    pause(5);
    s1 = aqwp.GetPosition_Position(0);
    s2 = ahwp.GetPosition_Position(0);
    s3 = bqwp.GetPosition_Position(0);
    s4 = bhwp.GetPosition_Position(0);
    if (s1 == 0 && s2 == 0 && s3 == 0 && s4 == 0)
        disp('homed!')
        break
    end
end

%% Going through all waveplate settings and writing to data file

H = idlerHv2(counttime,delay,aqwp,ahwp,bqwp,bhwp);

V = idlerVv2(counttime,delay,aqwp,ahwp,bqwp,bhwp);

D = idlerDv2(counttime,delay,aqwp,ahwp,bqwp,bhwp);

A = idlerAv2(counttime,delay,aqwp,ahwp,bqwp,bhwp);

R = idlerRv2(counttime,delay,aqwp,ahwp,bqwp,bhwp);

L = idlerLv2(counttime,delay,aqwp,ahwp,bqwp,bhwp);
```

Figure C.2: MATLAB Code for Automating Tomography Measurement (Part 2). This function controls the waveplates for the different polarization settings, records the data into a .csv file, and outputs the most likely density matrix to fit the data using maximum likelihood estimation. This portion of the code calls the tomoSetup functions, which initialize the waveplates, and the idler (Figures C.4-C.7) functions, which go through all 36 measurement settings and records the data into an array.

```matlab
tomo = [H; V; D; A; R; L]; % Join Lists
cell2csv(filename,tomo);

%% Close file so it can be read/edited

fclose('all');
pause(1)

%% Running Tomography Processing Software

tomoconvert(filename,outname);       % Converts .csv into .tomo
twoQubitTomo(outname,fig);           % Maximum Likelihood Analysis
finaltime = etime(clock,begintime);  % Calculate Duration of Data Collection
disp(finaltime)                      % Display Duration

close all; % This closes all files and windows
```

Figure C.3: MATLAB Code for Automating Tomography Measurement (Part 3). This function controls the waveplates for the different polarization settings, records the data into a .csv file, and outputs the most likely density matrix to fit the data using maximum likelihood estimation. This portion of the code converts the data array into a .csv file, converts it to a file (.tomo) readable by the maximum likelihood estimation function (twoqubittomo) and outputs the density matrix.

```matlab
function H = idlerHv2(counttime,delay,aqwp,ahwp,bqwp,bhwp)

% countime is the integration time over which photons are counted
% delay is the delay between detectors
% aqwp = 810 QWP; ahwp = 810 HWP; bqwp = 1550 QWP; bhwp = 1550 HWP

timeout = 20;

%% Polarization = HR

pol='HR'; % Label the Polarization in the List
disp(pol)
waveplate_move(0,0,315,0,counttime,aqwp,ahwp,bqwp,bhwp); %set waveplate angles

% Wait while the WPs move; timeout to avoid dead loop
t1 = clock;
while(etime(clock,t1)<timeout)
    s1 = int32(aqwp.GetPosition_Position(0));
    s2 = int32(ahwp.GetPosition_Position(0));
    s3 = int32(bqwp.GetPosition_Position(0));
    s4 = int32(bhwp.GetPosition_Position(0));
    if (s1 == 0 && s2 == 0 && s3 == 315 && s4 == 0)
        disp('done')
        break
    end
end
pause(2)

% Record Singles, Coincidences, and Accidentals to Data File

[idler, signal, coinc, ac] = tomo(counttime,delay);
HR = {pol, idler, signal, coinc, ac};

%% Polarization = HL (Repeat for Every Polarization Combination with 810 = H)

pol='HL';
disp(pol)
waveplate_move(0,0,45,0,counttime,aqwp,ahwp,bqwp,bhwp);
```

Figure C.4: MATLAB Idler Sub-Function for Automating Tomography Measurements: Part 1. There are six idler functions corresponding to the six polarization states measured per qubit (idlerHv2, idlerVv2, idlerDv2, idlerAv2, idlerRv2, idlerLv2). Here is an example for one horizontally polarized qubit combined with the six different polarizations of the second qubit (H, V, D, A, R, L). This portion of the code sets the polarization of the second qubit to $R = \frac{1}{\sqrt{2}}(|H\rangle - i|V\rangle)$ and records the singles, coincidences, and accidentals of the polarization combination over some integration time. The values are then recorded into their respective list, which is later read by the tomo_auto function (Figure C.3).

```matlab
t1 = clock;
while(etime(clock,t1)<timeout)
    s1 = int32(aqwp.GetPosition_Position(0));
    s2 = int32(ahwp.GetPosition_Position(0));
    s3 = int32(bqwp.GetPosition_Position(0));
    s4 = int32(bhwp.GetPosition_Position(0));
    if (s1 == 0 && s2 == 0 && s3 == 45 && s4 == 0)
        disp('done')
        break
    end
end
pause(2)

[idler, signal, coinc, ac] = tomo(counttime,delay);
HL = {pol, idler, signal, coinc, ac};

%% Polarization = HH

pol='HH';
disp(pol)
waveplate_move(0,0,0,0,counttime,aqwp,ahwp,bqwp,bhwp);

t1 = clock;
while(etime(clock,t1)<timeout)
    s1 = int32(aqwp.GetPosition_Position(0));
    s2 = int32(ahwp.GetPosition_Position(0));
    s3 = int32(bqwp.GetPosition_Position(0));
    s4 = int32(bhwp.GetPosition_Position(0));
    if (s1 == 0 && s2 == 0 && s3 == 0 && s4 == 0)
        disp('done')
        break
    end
end
pause(2)

[idler, signal, coinc, ac] = tomo(counttime,delay);
HH = {pol, idler, signal, coinc, ac};

%% Polarization = HD

pol='HD';
disp(pol)
waveplate_move(0,0,0,22.5,counttime,aqwp,ahwp,bqwp,bhwp);
```

Figure C.5: MATLAB Idler Sub-Function for Automating Tomography Measurements: Part 2. The function continues as in Figure C.4, going through polarization combinations HL, HH, and HD, and recording the data into their respective list.

```
t1 = clock;
while(etime(clock,t1)<timeout)
    s1 = int32(aqwp.GetPosition_Position(0));
    s2 = int32(ahwp.GetPosition_Position(0));
    s3 = int32(bqwp.GetPosition_Position(0));
    s4 = int32(bhwp.GetPosition_Position(0));
    if (s1 == 0 && s2 == 0 && s3 == 0 && s4 == 23)
        disp('done')
        break
    end
end
pause(2)

[idler, signal, coinc, ac] = tomo(counttime,delay);
HD = {pol, idler, signal, coinc, ac};

%% Polarization = HV

pol='HV';
disp(pol)
waveplate_move(0,0,0,45,counttime,aqwp,ahwp,bqwp,bhwp);

t1 = clock;
while(etime(clock,t1)<timeout)
    s1 = int32(aqwp.GetPosition_Position(0));
    s2 = int32(ahwp.GetPosition_Position(0));
    s3 = int32(bqwp.GetPosition_Position(0));
    s4 = int32(bhwp.GetPosition_Position(0));
    if (s1 == 0 && s2 == 0 && s3 == 0 && s4 == 45)
        disp('done')
        break
    end
end
pause(2)

[idler, signal, coinc, ac] = tomo(counttime,delay);
HV = {pol, idler, signal, coinc, ac};

%% Polarization = HA

pol='HA';
disp(pol)
waveplate_move(0,0,0,337.5,counttime,aqwp,ahwp,bqwp,bhwp);
```

Figure C.6: MATLAB Idler Sub-Function for Automating Tomography Measurements: Part 3. The function continues as in Figure C.4, going through polarization combinations HV and HA, and recording the data into their respective list.

```matlab
t1 = clock;
while(etime(clock,t1)<timeout)
    s1 = int32(aqwp.GetPosition_Position(0));
    s2 = int32(ahwp.GetPosition_Position(0));
    s3 = int32(bqwp.GetPosition_Position(0));
    s4 = int32(bhwp.GetPosition_Position(0));
    if (s1 == 0 && s2 == 0 && s3 == 0 && s4 == 338)
        disp('done')
        break
    end
end
pause(2)

[idler, signal, coinc, ac] = tomo(counttime,delay);
HA = {pol, idler, signal, coinc, ac};

H = [HH; HV; HD; HA; HR; HL]; % Create List of Measured Values

disp('prog = 17%') % Display Progress

end
```

Figure C.7: MATLAB Idler Sub-Function for Automating Tomography Measurements: Part 4. The "H" array is created and the progress bar is printed.

```matlab
function [aa, bb, cc, dd] = tomo_general(counttime,delay,ttres,coincwind)

% counttime = integration time for counting photons
% delay = calibrated delay between detector arrival times
% ttres = timetagger resolution
% coincwind = coincidence window; typically 10*ttres

pause(counttime)
c = tt_coincidences(0,counttime,coincwind,[0,delay*ttres]);
aa=c(1,1); % 810(idler) singles count
bb=c(2,2); % 1550(signal) singles count
cc=c(1,2); % coincidence counts
pause(counttime)
acc=tt_coincidences(0,counttime,coincwind,[0,10000*ttres]);
% arbitrary delay for CW pump
% acc=tt_coincidences(0,counttime,coincwind,[0,(delay+80)*ttres]);
% 12 .5 ns delay for Vanguard
dd=acc(2,1); % accidentals
pause(counttime)

end
```

Figure C.8: MATLAB Code for Measuring Singles, Coincidences, and Accidentals

```matlab
function spec_auto(start,stop,increment,filename,counttime,ttres, coincwind)

% this code works for 3s count time and 10s dwell time
% start = start wavelength in nm
% stop = stop wavelength in nm
% increment = step size in nm
% filename = accepts .csv
% counttime = integration time for photon counting
% ttres = timetagger resolution
% coincwind = coincidence window; typically 10*ttres
% stop must be greater than start

%% Initializing GPIB Connection to Laser Controls

wav = visa('ni','GPIB0::20::INSTR');
fopen(wav);
wav.EOSMode = 'read&write';

%% Sending Commands to Laser

command_str=['sour0:chan1:wav ' num2str(start) 'NM'];
fprintf(wav,command_str);
fprintf(wav,'outp0 1');

%% Measuring and Recording Data

for n = 1:(((stop-start)/increment))+1

    fileID = fopen(filename,'a');
    c = tt_coincidences(0,counttime,coincwind,[0,delay*ttres]);
    data=[start+((n-1)*increment),c(1,1)]; % Record only 810 Singles
    fprintf(fileID,'%6.2f, %25f\n',data);
    pause(1)
    command_str=['sour0:chan1:wav ' num2str(start+(n*increment)) 'NM'];
    fprintf(wav,command_str);
    n;
    pause(2) % Pause before next data point
end

%% Disconnect from Laser and Close Data File

fclose(wav);
delete(wav);
clear wav
fclose('all');
```

Figure C.9: The MATLAB code for automating the spectral measurements using stimulated downconversion and a 1550-nm seed tunable laser.

```matlab
function [delta_t, exit_times] = temporal_delay_KAM(length1, length2, length3,
length4,index_file,lambda_p,lambda_i,lambda_s)

format long
[lambda, nz_bulk, ny_bulk, nz_wg, ny_wg]=textread(index_file,
'%f %f %f %f %f','delimiter',',','headerlines',1);

c=2.9979e14; %speed of light in vacuum, unit=micron/second

%% Convert lambdas to integers
lambda_i_int=round(lambda_i); %lambda_i = idler wavelength
lambda_i_intp=lambda_i_int+1;
lambda_s_int=round(lambda_s); %lambda_s = signal wavelength
lambda_s_intp=lambda_s_int+1;
lambda_p_int=round(lambda_p); %lambda_p = pump wavelength
lambda_p_intp=lambda_p_int+1;

%% group velocity for H532
ny_532=ny_wg(lambda==lambda_p_int);
ny_532plus=ny_wg(lambda==(lambda_p_intp));
%calculate dn/dlambda unit=1/nm
delta_ny_532=(ny_532-ny_532plus)/(lambda_p_int-lambda_p_intp);
vgy_532=c/(ny_532 - lambda_p_int*delta_ny_532);
ngy_532=c/vgy_532;

%% group velocity for V810
nz_810=nz_wg(lambda==lambda_i_int);
nz_810plus=nz_wg(lambda==(lambda_i_intp));
%calculate dn/dlambda unit=1/nm
delta_nz_810=(nz_810-nz_810plus)/(lambda_i_int-lambda_i_intp);
vgz_810=c/(nz_810 - lambda_i_int*delta_nz_810)
ngz_810=c/vgz_810;

%% group velocity for H810
ny_810=ny_wg(lambda==lambda_i_int);
ny_810plus=ny_wg(lambda==(lambda_i_intp));
%calculate dn/dlambda unit=1/nm
delta_ny_810=(ny_810-ny_810plus)/(lambda_i_int-lambda_i_intp);
vgy_810=c/(ny_810 - lambda_i_int*delta_ny_810);
ngy_810=c/vgy_810;

%% group velocity for H1550
ny_1550=ny_wg(lambda==lambda_s_int);
ny_1550plus=ny_wg(lambda==(lambda_s_intp));
%calculate dn/dlambda unit=1/nm
```

Figure C.10: MATLAB Code for Calculating Temporal Compensation: Part 1. This code is specific to the consecutively poled waveguide-based source featured in Chapter 3.

```matlab
delta_ny_1550=(ny_1550-ny_1550plus)/(lambda_s_int-lambda_s_intp);
vgy_1550=c/(ny_1550 - lambda_s_int*delta_ny_1550);
ngy_1550=c/vgy_1550;

%% group velocity for V1550
nz_1550=nz_wg(lambda==lambda_s_int);
nz_1550plus=nz_wg(lambda==(lambda_s_intp));
%calculate dn/dlambda unit=1/nm
delta_nz_1550=(nz_1550-nz_1550plus)/(lambda_s_int-lambda_s_intp);
vgz_1550=c/(nz_1550 - lambda_s_int*delta_nz_1550);
ngz_1550=c/vgz_1550;

%% travel times

%%V810H1550 --> H810V1550
t532_1=(length1)/vgy_532; %length of first half of the first part of crystal
t810_2=(length2)/vgz_810; %length of second half of the first part of crystal
t532_3=(length3)/vgy_532; %length of first half of the second part of crystal
t810_4=(length4)/vgy_810; %length of second half of the second part of crystal

t1550_2=(length2)/vgy_1550;
t1550_4=(length4)/vgz_1550;

tV810=t532_1+t810_2;
tH810=t532_3+t810_4;
tH1550=t532_1+t1550_2;
tV1550=t532_3+t1550_4;

%%H810V1550 --> V810H1550
% t532_1=(length1)/vgy_532;
% t810_2=(length2)/vgy_810;
% t532_3=(length3)/vgy_532;
% t810_4=(length4)/vgz_810;
%
% t1550_2=(length2)/vgz_1550;
% t1550_4=(length4)/vgy_1550;

% %H810V1550 --> V810H1550
% tV810=t532_3+t810_4;
% tH810=t532_1+t810_2;
% tH1550=t532_3+t1550_4;
% tV1550=t532_1+t1550_2;

exit_times=[tH810,tV810,tV1550,tH1550];
```

Figure C.11: MATLAB Code for Calculating Temporal Compensation: Part 2

```matlab
%% time differences for the two polarizations for each wavelength in seconds

delta_t810 = tH810-tV810;
delta_t1550 = tV1550-tH1550;



%% time difference between the earliest exit times for the two wavelengths in
seconds

[pre_comp_Calc810, crystal_thickness_Calc810]
        = temporal_delay_precomp_crystal_calc('Calc', ...
        [3000, pi/2, pi/2, 0], lambda_i/1000, [0;0;1], delta_t810);

[pre_comp_Calc1550, crystal_thickness_Calc1550]
        = temporal_delay_precomp_crystal_calc('Calc', ...
        [3000, pi/2, pi/2, 0], lambda_s/1000, [0;0;1], delta_t1550);

disp(['Temporal walkoff (consecutive) for ', num2str(lambda_i),
                ' nm = ', num2str(delta_t810), ' s'])
disp(['Calcite thickness for ', num2str(lambda_i),
                ' nm = ', num2str(crystal_thickness_Calc810/1000), ' mm'])

disp(['Temporal walkoff (consecutive) for ', num2str(lambda_s),
                ' nm = ', num2str(delta_t1550), ' s'])
disp(['Calcite thickness for ', num2str(lambda_s),
                ' nm = ', num2str(crystal_thickness_Calc1550/1000), ' mm'])
```

Figure C.12: MATLAB Code for Calculating Temporal Compensation: Part 3

Appendix D

Mathematica Code for Fitting and Optimizing Using Error Analysis

Many of the data analysis techniques used in this thesis required using Monte Carlo simulations to estimate the error in the measurement and then fitting data to parabolas for parameter optimization. Although there are many languages and calculation platforms that can be used for performing this type of data analysis, Wolfram Mathematica was the software of choice for this dissertation. Figures D.1-D.3 show an example code for fitting and analyzing temporal compensation data for both the signal and idler wavelengths of the highly nondegenerate waveguide-based source from Chapter 3. This code starts by putting the data into 2D arrays and the error into 1D lists. Anything labeled with a 'C' refers to concurrence and with a 'P' refers to purity. The wavelengths are also referred to accordingly. Once the data and error are in their respectives arrays or lists, the 'NonlinearModelFit' function is used to fit the data to a parabola, $A + \frac{1}{4b}(x-e)^2$, where 'e' is the optimization parameter that we want to find. In this function, the errors are added as 'Weights' as shown. The 'Normal' function is used to transform the fitting function output into something that can be read by other functions later in the code. We can now get more information from the fitting function by executing Input 276 as shown. The resulting tables will give us the estimated value and standard error for the 'e' values, which can later be used in a weighted average as shown at the bottom of the code. Finally, to plot the fits with data points and error bars, the data and error must be combined into new lists as shown in Input 280; the 'Show' function is used to combine a 'ListPlot' and a 'Plot' of the fit.

```
In[260]:= conc1550 = {{-2, 0.75785}, {0, 0.86518}, {2, 0.81479}, {4, 0.66729}};
          cerrors1550 = {0.015555, 0.012413, 0.014415, 0.017863};
          pur1550 = {{-2, 0.78419}, {0, 0.87254}, {2, 0.83616}, {4, 0.72685}};
          perrors1550 = {0.011997, 0.010271, 0.011168, 0.01209};

In[264]:= conc810 = {{1, 0.69552}, {2, 0.80241}, {3, 0.86931}, {5, 0.81724}};
          cerrors810 = {0.014653, 0.015297, 0.014587, 0.016153};
          pur810 = {{1, 0.7442}, {2, 0.8266}, {3, 0.87552}, {5, 0.83849}};
          perrors810 = {0.010094, 0.0125, 0.012883, 0.0127};

          parabolaC810 = NonlinearModelFit[conc810, A + 1/(4b) (x - e)^2, {{A, 0.95}, {b, -0.05}, {e, 2}},
             x, Weights → 1/cerrors810^2];

          parabolaC1550 = NonlinearModelFit[conc1550, A + 1/(4b) (x - e)^2, {{A, 0.95}, {b, -0.05}, {e, 2}},
             x, Weights → 1/cerrors1550^2];

          pC810 = Normal[parabolaC810];
          pC1550 = Normal[parabolaC1550];
          parabolaP810 = NonlinearModelFit[pur810, A + 1/(4b) (x - e)^2, {{A, 0.95}, {b, -0.05}, {e, 2}},
             x, Weights → 1/perrors810^2];

          parabolaP1550 = NonlinearModelFit[pur1550, A + 1/(4b) (x - e)^2, {{A, 0.95}, {b, -0.05}, {e, 2}},
             x, Weights → 1/perrors1550^2];|

          pP810 = Normal[parabolaP810];
          pP1550 = Normal[parabolaP1550];

In[276]:= parabolaC810[{"BestFit", "ParameterTable"}]
          parabolaP810[{"BestFit", "ParameterTable"}]
          parabolaC1550[{"BestFit", "ParameterTable"}]
          parabolaP1550[{"BestFit", "ParameterTable"}]
```

Out[276]= $\left\{ 0.874671 - 0.0275125 \, (-3.56393 + x)^2, \right.$

	Estimate	Standard Error	t-Statistic	P-Value
A	0.874671	0.00504505	173.372	0.00367194
b	-9.08677	0.58222	-15.6071	0.0407347
e	3.56393	0.0526289	67.7183	0.00940032

Out[277]= $\left\{ 0.880396 - 0.0205775 \, (-3.5785 + x)^2, \right.$

	Estimate	Standard Error	t-Statistic	P-Value
A	0.880396	0.00268327	328.106	0.00194028
b	-12.1492	0.524628	-23.1577	0.0274736
e	3.5785	0.0359512	99.5377	0.00639555

Out[278]= $\left\{ 0.861678 - 0.0161633 \, (-0.487178 + x)^2, \right.$

	Estimate	Standard Error	t-Statistic	P-Value
A	0.861678	0.0102272	84.2536	0.00755564
b	-15.4672	1.76786	-8.7491	0.0724497
e	0.487178	0.121852	3.99811	0.156029

Out[279]= $\left\{ 0.869685 - 0.0124359 \, (-0.573132 + x)^2, \right.$

	Estimate	Standard Error	t-Statistic	P-Value
A	0.869685	0.00898053	96.8411	0.00657362
b	-20.1031	2.45272	-8.19625	0.0772901
e	0.573132	0.125936	4.55096	0.137699

Figure D.1: Mathematica Code for Fitting and Optimizing Using Error Analysis: Part 1. This code is an example of how to fit data with error bars and do error analysis using Mathematica.

```
In[280]:= cerrorlist810 = Around[#[[1]], #[[2]]] & /@ Transpose[{conc810[[ ;; , 2]], cerrors810}];
        perrorlist810 = Around[#[[1]], #[[2]]] & /@ Transpose[{pur810[[ ;; , 2]], perrors810}];
        cerrorlist1550 = Around[#[[1]], #[[2]]] & /@ Transpose[{conc1550[[ ;; , 2]], cerrors1550}];
        perrorlist1550 = Around[#[[1]], #[[2]]] & /@ Transpose[{pur1550[[ ;; , 2]], perrors1550}];

In[284]:= Show[ListPlot[{Transpose[{conc810[[ ;; , 1]], cerrorlist810}],
          Transpose[{pur810[[ ;; , 1]], perrorlist810}]}, PlotRange → All, Frame → True,
        FrameLabel → {"810 Temporal Compensation", "Characterization Metric"},
        FrameStyle → Directive[Black, 14], PlotStyle → {Red, Blue}, PlotRange → All],
       Plot[{pC810, pP810}, {x, 0, 6}, PlotLegends → { "Concurrence", "Purity"},
        PlotStyle → {Red, Blue}, PlotRange → All]]
```
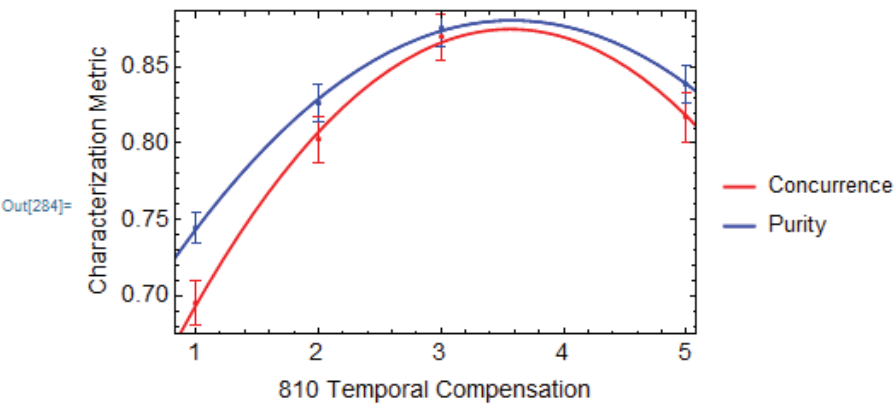


```
In[285]:= Show[ListPlot[{Transpose[{conc1550[[ ;; , 1]], cerrorlist1550}],
          Transpose[{pur1550[[ ;; , 1]], perrorlist1550}]}, PlotRange → All, Frame → True,
        FrameLabel → {"1550 Temporal Compensation", "Characterization Metric"},
        FrameStyle → Directive[Black, 14], PlotStyle → {Red, Blue}, PlotRange → All],
       Plot[{pC1550, pP1550}, {x, -2, 4}, PlotLegends → { "Concurrence", "Purity"},
        PlotStyle → {Red, Blue}, PlotRange → All]]
```
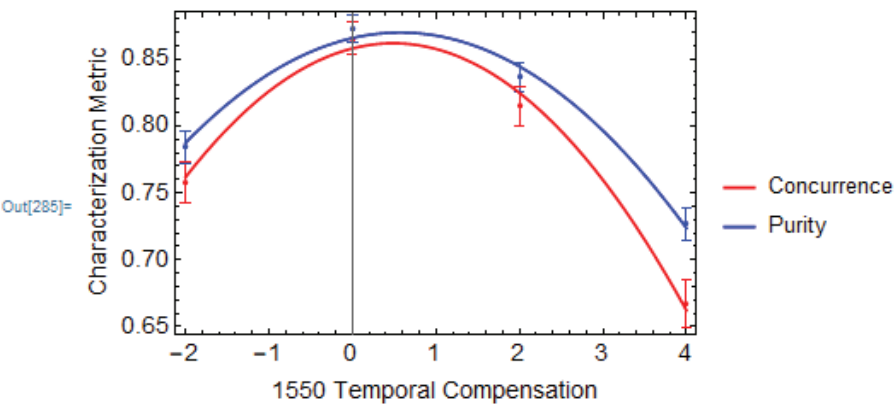

Figure D.2: Mathematica Code for Fitting and Optimizing Using Error Analysis: Part 2

106

```
In[286]:= wc1550 = 1 / 0.12185197701135543`^2;
         wp1550 = 1 / 0.12593649006657823`^2;
         c1550 = 0.4871775847733313`;
         p1550 = 0.5731320283290554`;
         calcitemean1550 = (wc1550 * c1550 + wp1550 * p1550) / (wc1550 + wp1550)

         calcitesigma1550 = 1 / Sqrt[wc1550 + wp1550]

Out[290]= 0.528738

Out[291]= 0.0875708

In[292]:= wc810 = 1 / 0.05262886339344455`^2;
         wp810 = 1 / 0.0359512048952395`^2;
         c810 = 3.563934732683664`;
         p810 = 3.5784992233141715`;
         calcitemean810 = (wc810 * c810 + wp810 * p810) / (wc810 + wp810)

         calcitesigma810 = 1 / Sqrt[wc810 + wp810]

Out[296]= 3.57387

Out[297]= 0.029686
```

Figure D.3: Mathematica Code for Fitting and Optimizing Using Error Analysis: Part 3

References

[1] C. H. Bennett, G. Brassard, C. Crépeau, R. Jozsa, A. Peres, and W. K. Wootters, Phys. Rev. Lett. **70**, 1895 (1993).

[2] M. Żukowski, A. Zeilinger, M. A. Horne, and A. K. Ekert, Phys. Rev. Lett. **71**, 4287 (1993).

[3] J.-W. Pan, D. Bouwmeester, H. Weinfurter, and A. Zeilinger, Phys. Rev. Lett. **80**, 3891 (1998).

[4] M. Halder, A. Beveratos, N. Gisin, V. Scarani, C. Simon, and H. Zbinden, Nature Physics **3**, 692 (2007).

[5] J. Yin, Y. Cao, Y.-H. Li, S.-K. Liao, L. Zhang, J.-G. Ren, W.-Q. Cai, W.-Y. Liu, B. Li, H. Dai, G.-B. Li, Q.-M. Lu, Y.-H. Gong, Y. Xu, S.-L. Li, F.-Z. Li, Y.-Y. Yin, Z.-Q. Jiang, M. Li, J.-J. Jia, G. Ren, D. He, Y.-L. Zhou, X.-X. Zhang, N. Wang, X. Chang, Z.-C. Zhu, N.-L. Liu, Y.-A. Chen, C.-Y. Lu, R. Shu, C.-Z. Peng, J.-Y. Wang, and J.-W. Pan, Science **356**, 1140 (2017).

[6] F. Kaneda, K. Garay-Palmett, A. B. U'Ren, and P. G. Kwiat, Opt. Express **24**, 10733 (2016).

[7] J. Yin, Y.-H. Li, S.-K. Liao, M. Yang, Y. Cao, L. Zhang, J.-G. Ren, W.-Q. Cai, W.-Y. Liu, S.-L. Li, R. Shu, Y.-M. Huang, L. Deng, L. Li, Q. Zhang, N.-L. Liu, Y.-A. Chen, C.-Y. Lu, X.-B. Wang, F. Xu, J.-Y. Wang, C.-Z. Peng, A. K. Ekert, and J.-W. Pan, Nature **582**, 501 (2020).

[8] J. C. Chapman, T. M. Graham, C. K. Zeitler, H. J. Bernstein, and P. G. Kwiat, Phys. Rev. Applied **14**, 014044 (2020).

[9] N. K. Langford, R. B. Dalton, M. D. Harvey, J. L. O'Brien, G. J. Pryde, A. Gilchrist, S. D. Bartlett, and A. G. White, Phys. Rev. Lett. **93**, 053601 (2004).

[10] A. Mair, A. Vaziri, G. Weihs, and A. Zeilinger, Nature **412**, 313 (2001).

[11] P. Imany, J. A. Jaramillo-Villegas, M. S. Alshaykh, J. M. Lukens, O. D. Odele, A. J. Moore, D. E. Leaird, M. Qi, and A. M. Weiner, npj Quantum Information **5**, 59 (2019).

[12] C. K. Hong, Z. Y. Ou, and L. Mandel, Phys. Rev. Lett. **59**, 2044 (1987).

[13] P. G. Kwiat, K. Mattle, H. Weinfurter, A. Zeilinger, A. V. Sergienko, and Y. Shih, Phys. Rev. Lett. **75**, 4337 (1995).

[14] P. G. Kwiat, E. Waks, A. G. White, I. Appelbaum, and P. H. Eberhard, Phys. Rev. A **60**, R773 (1999).

[15] D. C. Burnham and D. L. Weinberg, Phys. Rev. Lett. **25**, 84 (1970).

[16] A. Christ, A. Fedrizzi, H. Hübel, T. Jennewein, and C. Silberhorn, Experimental Methods in the Physical Sciences **45**, 351 (2013).

[17] M. Hentschel, H. Hübel, A. Poppe, and A. Zeilinger, Opt. Express **17**, 23153 (2009).

[18] F. Kaneda and P. G. Kwiat, Science Advances **5** (2019).

[19] R. W. Boyd, *Nonlinear Optics, 4th Edition* (Elsevier, Inc., London, 2020).

[20] J. Schneeloch, S. H. Knarr, D. F. Bogorin, M. L. Levangie, C. C. Tison, R. Frank, G. A. Howland, M. L. Fanto, and P. M. Alsing, Journal of Optics **21**, 043501 (2019).

[21] A. Anwar, C. Perumangatt, F. Steinlechner, T. Jennewein, and A. Ling, Review of Scientific Instruments **92**, 041101 (2021).

[22] C. K. Hong and L. Mandel, Phys. Rev. A **31**, 2409 (1985).

[23] R. S. Bennink, Phys. Rev. A **81**, 053805 (2010).

[24] T. B. Pittman, D. V. Strekalov, D. N. Klyshko, M. H. Rubin, A. V. Sergienko, and Y. H. Shih, Phys. Rev. A **53**, 2804 (1996).

[25] Advr-Inc, private communication (2017-present).

[26] M. J. Lighthill, IMA Journal of Applied Mathematics **1**, 1 (1965).

[27] I. H. Malitson, J. Opt. Soc. Am. **55**, 1205 (1965).

[28] M. H. Rubin, D. N. Klyshko, Y. H. Shih, and A. V. Sergienko, Phys. Rev. A **50**, 5122 (1994).

[29] T. E. Keller and M. H. Rubin, Phys. Rev. A **56**, 1534 (1997).

[30] T. Suhara, G. Nakaya, J. Kawashima, and M. Fujimura, IEEE Photonics Technology Letters **21**, 1096 (2009).

[31] A. Christ, A. Fedrizzi, H. Hübel, T. Jennewein, and C. Silberhorn, Experimental Methods in the Physical Sciences **45**, 351 (2013).

[32] P. J. Mosley, A. Christ, A. Eckstein, and C. Silberhorn, Phys. Rev. Lett. **103**, 233901 (2009).

[33] P. S. Kuo, V. B. Verma, and S. W. Nam, OSA Continuum **3**, 295 (2020).

[34] H. Herrmann, X. Yang, A. Thomas, A. Poppe, W. Sohler, and C. Silberhorn, Opt. Express **21**, 27981 (2013).

[35] D. Kang, N. Zareian, and A. S. Helmy, in *Advances in Photonics of Quantum Computing, Memory, and Communication XI*, Vol. 10547, edited by Z. U. Hasan, P. R. Hemmer, A. E. Craig, and A. L. Migdall, International Society for Optics and Photonics (SPIE, 2018) pp. 67 – 73.

[36] K. Thyagarajan, J. Lugani, S. Ghosh, K. Sinha, A. Martin, D. B. Ostrowsky, O. Alibart, and S. Tanzilli, Phys. Rev. A **80**, 052321 (2009).

[37] D. F. V. James, P. G. Kwiat, W. J. Munro, and A. G. White, Phys. Rev. A **64**, 052312 (2001).

[38] S. Turro, "Guide to quantum state tomography," (2021).

[39] W. Wootters, Quantum Information & Computation **1**, 27 (2001).

[40] R. Jozsa, Journal of Modern Optics **41**, 2315 (1994).

[41] Z. Y. Ou, L. J. Wang, and L. Mandel, J. Opt. Soc. Am. B **7**, 211 (1990).

[42] H. J. Hoffmann, W. W. Jochs, and G. Westenberger, in *Properties and Characteristics of Optical Glass II*, Vol. 1327, edited by A. J. M. III, International Society for Optics and Photonics (SPIE, 1990) pp. 219 – 230.

[43] Y. Chen, M. Fink, F. Steinlechner, J. P. Torres, and R. Ursin, npj Quantum Information **5**, 43 (2019).

[44] A. M. Steinberg, P. G. Kwiat, and R. Y. Chiao, Phys. Rev. A **45**, 6659 (1992).

[45] A. F. Abouraddy, M. B. Nasr, B. E. A. Saleh, A. V. Sergienko, and M. C. Teich, Phys. Rev. A **65**, 053817 (2002).

[46] M. B. Nasr, B. E. A. Saleh, A. V. Sergienko, and M. C. Teich, Phys. Rev. Lett. **91**, 083601 (2003).

[47] M. B. Nasr, O. Minaeva, G. N. Goltsman, A. V. Sergienko, B. E. A. Saleh, and M. C. Teich, Opt. Express **16**, 15104 (2008).

[48] M. B. Nasr, S. Carrasco, B. E. A. Saleh, A. V. Sergienko, M. C. Teich, J. P. Torres, L. Torner, D. S. Hum, and M. M. Fejer, Phys. Rev. Lett. **100**, 183601 (2008).

[49] M. B. Nasr, D. P. Goode, N. Nguyen, G. Rong, L. Yang, B. M. Reinhard, B. E. Saleh, and M. C. Teich, Optics Communications **282**, 1154 (2009).

[50] J. Brion, A. Chakir, J. Charbonnier, D. Daumont, C. Parisse, and J. Malicet, Journal of Atmospheric Chemistry **30**, 291 (1998).

[51] L. K. Shalm, E. Meyer-Scott, B. G. Christensen, P. Bierhorst, M. A. Wayne, M. J. Stevens, T. Gerrits, S. Glancy, D. R. Hamel, M. S. Allman, K. J. Coakley, S. D. Dyer, C. Hodge, A. E. Lita, V. B. Verma, C. Lambrocco, E. Tortorici, A. L. Migdall, Y. Zhang,

D. R. Kumor, W. H. Farr, F. Marsili, M. D. Shaw, J. A. Stern, C. Abellán, W. Amaya, V. Pruneri, T. Jennewein, M. W. Mitchell, P. G. Kwiat, J. C. Bienfang, R. P. Mirin, E. Knill, and S. W. Nam, Phys. Rev. Lett. **115**, 250402 (2015).

[52] ORNL, private communication (2021).

[53] LightMachinery, "Grating spectrometers - user's guide," (2021).